Crustal deformation from geodetic techniques: Earthquakes and plate movements in the South Iceland Seismic Zone

---

Judicael Decriem

Faculty of Earth Sciences
University of Iceland

Crustal deformation from geodetic techniques: Earthquakes and plate movements in the South Iceland Seismic Zone

Judicael Decriem

A dissertation submitted to the Faculty of Earth Sciences for the degree of
Doctor of Philosophy in Geophysics

Thesis advisors

Dr. Thóra Árnadóttir
Nordic Volcanological Centre, University of Iceland

Doctoral Committee

Dr. Thóra Árnadóttir
Nordic Volcanological Centre, University of Iceland

Prof. Páll Einarsson
Institute of Earth Science, University of Iceland

Dr. Freysteinn Sigmundsson
Institute of Earth Science, University of Iceland

Dr. Sigurjón Jónsson
King Abdullah University of Science and Technology (KAUST), Saudi Arabia

Opponents

Dr. Tim Wright
Institute of Geophysics and Tectonics, School of Earth and Environment, The
University of Leeds

Dr. Kristín Vogfjörd
Icelandic Meteorological Office. Reykjavík

Faculty of Earth Sciences
School of Engineering and Natural Sciences
University of Iceland

Crustal deformation from geodetic techniques: Earthquakes and plate movements in the South Iceland Seismic Zone
A dissertation submitted to the Faculty of Earth Sciences for the degree of Doctor of Philosophy in Geophysics

Contents

Abstract

The South Iceland Seismic Zone (SISZ) is one of the most seismically active area in Iceland. The last two major events occured in the central and western parts of the SISZ in June 2000 and May 2008, respectively. In this thesis, I use geodetic methods to estimate the deformation due to earthquakes and plate spreading and derive models of the crustal processes.

In the first paper we derive a uniform-slip and a variable-slip fault models for the two 29 May 2008 earthquakes based on GPS and InSAR observations. We account for the variation in the elastic parameters of the crust with depth. Our models indicate that the slip for the first event (Ingólfsfjall) was concentrated at 2–4 km depth, with a maximum of 1.9 m, whereas the slip on the second fault (Kross) was located deeper, at 3–6 km depth with up to 1.4 m of motion. Static Coulomb failure stress calculations indicate that the first event caused a stress increase in the area of the main asperity on the second fault. We estimated a composite moment that equals a $M_w6.1$ for the doublet. We also find that the June 2000 – May 2008 sequence only released about half of the moment accumulated by plate motion since the previous earthquake sequence in the SISZ during 1896–1912.

In the second paper we document the transient following the June 2000 earthquakes, extending a previous study with GPS data from 2004 to 2008. We explore whether viscoelastic models based on Maxwell and/or standard linear solid (SLS) rheologies can reproduce the surface velocities observed during 2000–2008 and calculate the corresponding stress changes. Our preferred model consists of a ~15 km thick elastic crust overlying a SLS upper mantle with a viscosity of 1-$2 \cdot 10^{18}$ Pa s and relaxation strength between 0.1–0.25. The viscoelastic transient promotes failure in the area of the May 2008 earthquake. However, the Coulomb failure stress changes due to the viscoelastic relaxation are very small (0.05 MPa) compared to the static stress changes from the June 2000 main shocks. Viscoelastic loading may therefore not be the main trigger for the May 2008 events.

In the third paper we study the deformation following the May 2008 earthquakes using GPS and InSAR observations. We test poroelastic, viscoelastic and afterslip models in order to determine the dominent mechanism driving the transient observed. Our best model involves viscoelastic relaxation and shallow afterslip to explain both the far field and near field displacements. We also propose that an impermeable structure disrupts fluid flow and causes pore pressure changes that could be an explanation for a sharp EW lineament highlighted in some interferograms in an area where a large number of aftershocks occured, west of the two mainshocks.

Ágrip

Ritgerðin er samsett úr þremur vísindagreinum ásamt inngangi, sem eiga það sammerkt að fjalla um landmælingar og líkangerð á jarðskorpuhreyfingum í skjálftabelti Suðurlands. Skjálftavirknin er á svæði sem liggur þvert yfir Suðurland frá vestri til austurs og er kallað Suðurlandsskjálftabeltið. Töluverð jarðskjálftavirkni hefur verið á svæðinu, nú síðast svonefndir Suðurlandsskjálftar í júní 2000, og Ölfusskjálftar í maí 2008.

Í fyrstu greininni er greint frá landmælingum með Global Positioning System (GPS) og radarmælingingum með gervitunglum (InSAR), sem sýna jarðskorpu-hreyfingar vegna jarskjálftanna í Ölfusi þann 29. maí 2008. Landmælingagögnin voru notuð við líkanreikninga til að ákvarða legu misgengja sem hreyfðust í skjálftunum, og færslur á þeim. Líkanreikningarnir tóku tillit til lagskiptingar í jarðskorpunni og með samtúlkun á GPS gögnum og InSAR bylgjuvíxlmyndum fékkst nákvæm mynd af þrívíðum hreyfingum. Stærð skjálftanna tveggja var metin út frá líkanreikningum af upptökunum (þ.e. færslu og stærð brotflatar), og bentu til að skjálftarnir hefðu verið álíka stórir, og samanlögð vægisstærð (M_w)þeirra um 6.1. Upptakalíkönin voru síðan notuð til að reikna Coulomb spennubreytingar á upptakasvæðinu. Þeir útreikningar benda til að færslur á misgenginu sem liggur undir vestanverðu Ingólfsfjalli, sem hreyfðist í fyrri skjálftanum, hafi valdið umtalsverðum spennubreytingum á misgengi sem liggur um 5 km vestar, og kennt hefur verið við bæinn Kross. Því er líklegt að skjálftinn í Ingólfsfjalli hafi hleypt af stað skjálfta á Kross-misgenginu. Slík atburðarrás er mjög óvenjuleg, þar sem skjálftar verða á tveimur samsíða misgengjum, en skýrist af tektóník á Suðurlandi. Spennubreytingar gætu einnig skýrt töluverða skjálftavirkni á svæðinu vestur að þrengslum, þó landmælingar bendi ekki til að mikil misgengishreyfing hafi orðið á því svæði. Reikningar á upphleðslu spennu vegna landreks og spennufall í jarðskorpunni á Suðurlandi vegna jarðskjálfta frá 1600–2010 benda til að enn sé veruleg spenna til staðar í jarðskorpunni, og því hægt að búast við áframhaldandi skjálftavirkni á Suðurlandi á næstu árum eða áratugum.

Verkefnið, sem lýst er í öðrum kafla ritgerðarinnar, byggir á landmælingum og líkanreikningum á jarðskorpuhreyfingum á Suðurlandi á árunum 2000 til 2008. Fyrri rannsóknir studdust við GPS gögn frá 2000 til 2004 (Þóra Árnadóttir o.fl., 2005) og bylgjuvíxlmyndir frá 2000 til 2005 (Sigurjón Jónsson, 2008). Mikilvægt var að lengja tímaröð landmælingagagna til að fá betri upplýsingar um hve lengi má greina hægar hreyfingar í kjölfar Suðurlandsskjálftanna. Landmælingarnar sýna að mjög hefur hægt á jarðskopuhreyfingum í kjölfar Suðurlandsskjálfta eftir 2005. Í þessari rannsókn voru kannaðar mun fleiri gerðir af seig-fjaðrandi (e. viscoelastic) jarðlíkönum en í fyrri rannsóknum. Auk Maxwell efniseiginleika voru notuð líkön með Standard-linear-solid (SLS) eiginleika, sem herma betur eftir ólínulegri hegðun efnis. Jarðarlíkanið sem best fellur að GPS og InSAR gögnum er með um 15 km þykkri fjaðrandi plötu og hálfrúmi með SLS hegðun og frekar lágri seigju, um $1\text{–}2{\cdot}10^{18}$ Pa s. Þessar hægu hreyfingar ollu spennubreytingum (e. Coulomb Failure stress) á upptakasvæði Ölfusskjálftanna, sem eru þó um stærðargráðu minni en spennubreytingarnar sem Suðurlandsskjálftarnir ollu.

Þriðji hluti ritgerðarinnar fjallar um mælingar á jarðskorpuhreyfingum í kjölfar Ölfusskjálftanna 2008. Gögnum var safnað, nánast samfellt, með GPS mælingum á 17 stöðvum í rúma tvo mánuði eftir skjálftana, og síðan voru GPS landmælingar framkvæmdar vorið 2009. Líkanreikingar sem best falla að þessum landmælingagögnum benda til að hreyfingar í kjölfar Ölfusskjálftanna séu bæði vegna seig-fjaðrandi eiginleika jarðar og að smávægileg færsla hafi orðið á grynnsta hluta brotflatanna, fyrstu mánuðina eftir skjálftana. Hreyfingar, sem gætu tengst þrýstingsbreytingum í grunnvatni eða jarðhitakerfum á svæðinu (e. poroelastic rebound), virðast ekki vera jafnmiklar og í kjölfar Suðurlandsskjálftana 2000. Leiðrétta þarf landmælingarnar fyrir hreyfingum vegna landreks og færslum á Hengilssvæðinu, sem eru töluverðar á tímabilinu 2008–2009, og má líklega rekja til vinnslu á jarðhita.

Acknowledgments

I am grateful to all the people that supported me during this PhD project. First of all I would like to thank Thóra Árnadóttir for her scientific guidance, great ideas, and for her constructive comments and time with me during the writing. Thanks also go to Páll Einarsson and Freysteinn Sigmundsson for sharing their invaluable knowledge of Iceland and attention to my work. I would like to thank Andy Hooper for his strong involvement with us in both the InSAR processing and modelling, and Halldor Geirsson for his great expertise in the CGPS of Iceland. I am grateful to all the scientists that have contributed to this work to various extents: Bryndís Brandsdóttir, Sigrún Hreinsdóttir, Sigurjón Jónsson, Kaj M. Johnson, Kurt Feigl, Peter C. LaFemina, and Rick Bennett.

I want to thank my family for continuous and immutable support. Thanks to my wife, Julie, for supporting me and keeping me on track during the difficult time, I could not have made this without you. I am deeply grateful to my parents for their support during all my studies.

Thanks go also to many friends and students from Iceland, Uppsala and other places, some of them are Thorbjörg, Marj and David, Benni, Marie, JR, Cedric, πR, Sigurlaug, Oskar, Thomas, Emmanuel, Magda, Taichi, Ingi, Guillaume, Thorgils, and Pierre. Special thanks go to the Icelandic Rescue Team for the bad time in Eldgjá and the nice time in Eyjafjallajökull.

This PhD was funded by grants from the Icelandic Research Council for the projects "High-rate continuous GPS observations in Iceland" (Grant of Excel-

Introduction

My research during this PhD project focuses on the seismic cycle and transient deformation in South Iceland Seismic Zone (SISZ). The SISZ is one of the most seismically active areas in Iceland. Our goal is to improve our understanding of the ongoing crustal processes. Such understanding is crucial to assess the seismic cycle and the resulting earthquakes. The area is populated, and several agricultural, touristic, industrial, and housing projects are under way or have been started. Earthquakes tend to occur in sequences in SISZ. The questions we want to adress here are whether the earthquake trigerring in the SISZ can be related to postseismic deformation from earlier events, what does the postseismic deformation tell us about the crustal structure, and also if we should expect more events in the SISZ in the near future.

We studied coseismic and postseismic surface deformation of past events in the SISZ (June 2000 and May 2008) using geodetic techniques (GPS and InSAR) through three papers. The thread connecting the three papers is how we can relate the surface deformation to deeper mechanism: elastic slip, poroelastic and viscoelastic relaxation.

The coseismic deformation is a result of stress drop due to elastic slip during an earthquake. This stress drop gives indication on the current stress available in the area as well as the size of the event. We calculate elastic slip models for the two May 2008 earthquakes, and also present a model of the stress build-up and release by earthquakes from 1600 to 2010. Our study indicates that further events may occur in the SISZ in the coming years.

We also studied the postseismic deformation after the June 2000 and May 2008 events. Several processes occur at different time scales following an earthquake which result in different deformation and stress load of the surrounding crust. We found a long term transient consistent with viscoelastic relaxation for both events.

In the first part of this thesis, we will give an overview of the tectonic setting

1

and past seismic activity of SISZ. Then we briefly introduce the geodetic methods applied (GPS and InSAR) and modelling. The second part is composed of three papers.

Decriem J., Árnadóttir Th., Hooper A., Geirsson H., Sigmundsson F., Keiding M., Ófeigsson B.G., Hreinsdóttir S., Einarsson P., LaFemina P.C., and Bennett R.A., The 2008 May 29 earthquake doublet in SW Iceland, *Geophysical Journal International*, doi:10.1111/j.1365-246X.2010.04565.x **(GJI 2010 best student paper award)**

Decriem J. and Árnadóttir Th., Transient crustal deformation in the South Iceland Seismic Zone observed by GPS and InSAR during 2000-2008, *submitted to Tectonophysics, 2010*.

Decriem J., Árnadóttir Th., Hreinsdóttir S., Hooper A., Geirsson H., LaFemina P.C., and Bennett R.A., Postseismic relaxation following the May 2008 earthquakes South Iceland, *submitted to Geophysical Journal International, 2011*.

Other publications worked on during the PhD project are:

Hreinsdóttir S., Árnadóttir Th., **Decriem J.**, Geirsson H., Tryggvason A., Bennett R.A., and LaFemina P.C., A complex earthquake sequence captured by the continuous GPS network in SW Iceland, *Geophysical Research Letter*,36, doi:0.1029/2009GL038391,2009.

Sigmundsson F., Hreinsdóttir S., Hooper A., Árnadóttir Th., Pedersen R., Roberts M.J., Óskarsson N., Auriac A., **Decriem J.**, Einarsson P., Geirsson H., Hensch M., Ófeigsson B.G., Sturkell E., Sveinbjörnsson H., and Feigl. K.L., Intrusion triggering of the 2010 Eyjafjallajökull explosive eruption. *Nature*, 468(7322):426-430, November 2010.

Geirsson, H., Árnadóttir Th., S. Hreinsdóttir, **Decriem J.**, LaFemina P.C., Jónsson S., Bennett R.A., Metzger S., Holland A., Sturkell E., Villemin T., Völksen C., Sigmundsson F., Einarsson P., Roberts M.J., Sveinbjörnsson H., Overview of results from continuous GPS observations in Iceland from 1995 to 2010, *Jökull*, 2011.

1.1 The South Iceland Seismic Zone

1.1.1 Tectonic setting

Located on the Mid-Atlantic Ridge (MAR), Iceland widens by 19mm/year due to the continuous spreading between the North American and Eurasian plates. The South Iceland Seismic Zone (SISZ) is a transform zone accomodating the opening of the Reykjanes Peninsula (RP) and the Western Volcanic Zone (WVZ) to the west and the Eastern Volcanic Zone (EVZ) to the east (Fig. 1.1).

The accommodation of E–W shear at depth in the SISZ by motion on a series of parallel N–S faults, causing counter clockwise rotation of blocks, has been termed "bookshelf faulting" (Einarsson, 1991, 2010; Sigmundsson et al., 1995).
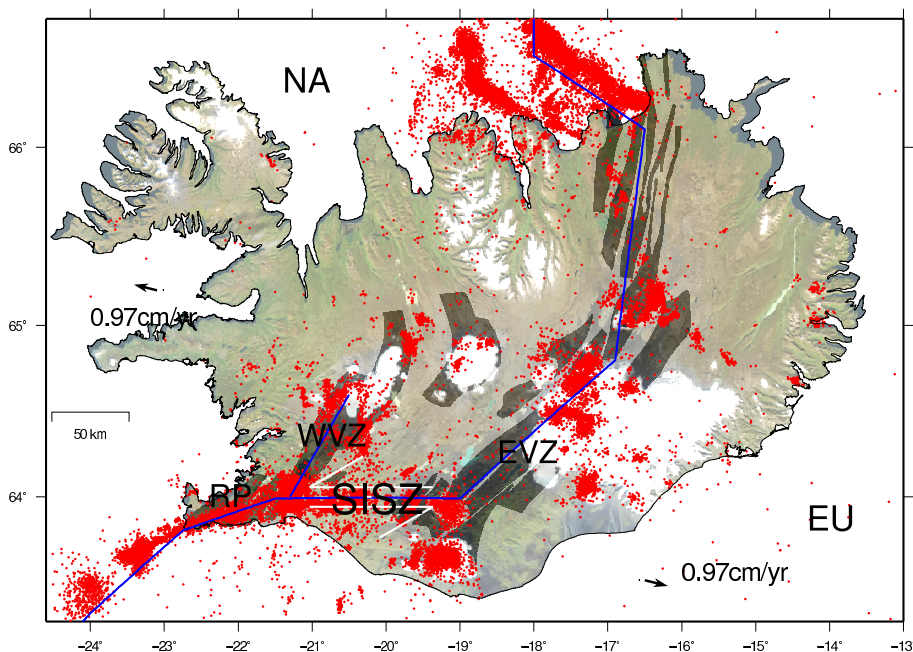

Figure 1.1: Tectonic setting of South Iceland Seismic Zone (SISZ), the blue line indicates the location of the active plate boundary through Iceland, red dots show the earthquakes recorded by the SIL network since 1989. Black arrows indicate the spreading direction between the Eurasian (EU) and North America (NA) plates. Dark areas show volcanic systems (Einarsson and Sæmundsson, 1987)

The SISZ is characterized by arrays of N–S right lateral strike slip faults, spaced 2–5 km apart (Einarsson, 1991; Clifton and Einarsson, 2005). Each of the N–S faults is composed of an array of left stepping *en echelon* surface fractures, separated by push-up structures (e.g., Einarsson and Eiríksson, 1982; Bjarnason et al., 1993b; Clifton and Einarsson, 2005). Sequences of earthquakes in the
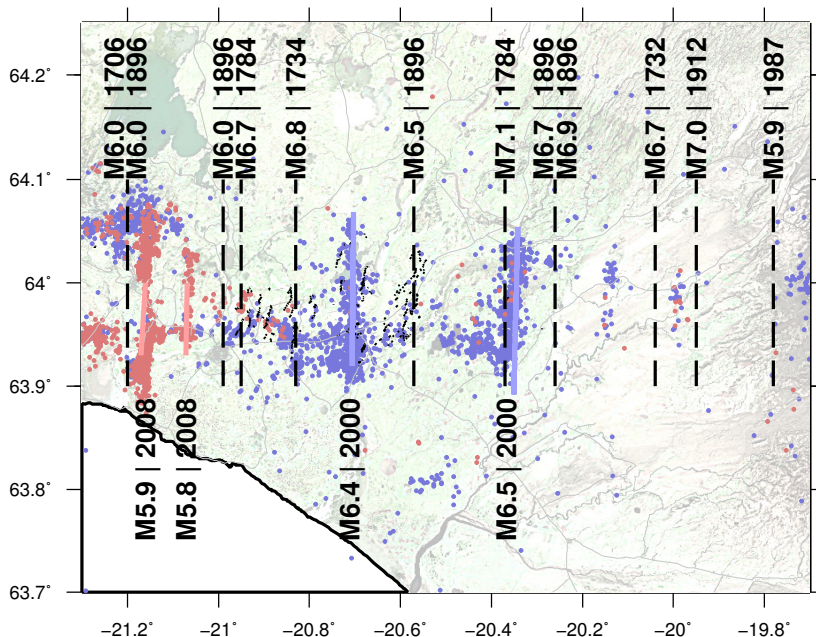
Figure 1.2: Moderate size (M>6) earthquakes in SISZ since 1600. The magnitudes of historical events are M_S and magnitudes for events in 2000 and 2008 are M_w, estimated from geodetic studies. Blue and red thick lines show the location of the June 2000 and the May 2008 faults, respectively.

SISZ have been documented in historical records, for example in 1732–34, 1784, and 1896 (Stefánsson and Halldórsson, 1988; Einarsson et al., 1981). During the 1896 sequence at least five events larger than magnitude 6 were reported over a distance of 50 km within two weeks (Fig 1.2). The largest instrumentally recorded earthquake was a M_S=7.0 event which struck the eastern part of the SISZ in 1912 (Bjarnason et al., 1993a; Bellou et al., 2005). Fig 1.2 shows the approximate location of the historical earthquakes in SISZ since 1600.

1.1.2 The June 2000 earthquakes

Mainshock of magnitude $M_w = 6.5$ on 17 June 2000 in the east-central part (Fig 1.3) of SISZ intiated a new earthquake sequence. It was followed 81 hours later by another $M_w = 6.5$ event, located 17 km west of the first mainshock. The surface deformation caused by the 17 and 21 June mainshocks was measured using both GPS and Interferometric Synthetic Aperture Radar (InSAR). Geodetic data suggests up to 2.5 m of slip on two parallel 20 km long N–S faults (Árnadóttir et al., 2001; Pedersen et al., 2001, 2003). Observations of rapid post-seismic deformation have been explained by models of poro-elastic rebound (Jónsson et al., 2003).

Three $M_w > 5$ events were triggered along the plate boundary on the Reykjanes Peninsula, up to 80 km from the 17 June mainshock (Pagli et al., 2003; Vogfjörd, 2003). One of these events caused a water level drop of several meters of Lake Kleifarvatn (Clifton et al., 2003).

Static stress changes (Árnadóttir et al., 2003, 2004) following the 17 June mainshock promote failure on the 21 June fault. However, the 81 hr delay between the two main events may be better explained by stress changes due to fluid flow following the first mainshock (Lindman, 2009).

1.1.3 The May 2008 earthquakes

The 29 May earthquake doublet is the continuation of the sequence that started in June 2000. An initial mainshock beneath the Ingólfsfjall mountain (63.972°N, 21.072°W and ∼5 km depth, Fig 1.3) at 15:45:58.9 UTC according to the SIL seismic catalog (IMO), was followed almost immediately by earthquakes on a second fault (the Kross fault), located approximately 5 km west of the initial mainshock. Increased earthquake activity was also observed along an E–W zone, with several $M_L 3$ events (Brandsdóttir et al., 2010).

The teleseismic centroid-moment-tensor solutions indicate a nearly vertical, N–S right-lateral source fault, and a moment magnitude of $M_w 6.3$ (NEIC). Co-seismic offsets were observed by the CGPS network in the area (Hreinsdóttir et al., 2009), and campaign style GPS measurements (Decriem et al., 2010).
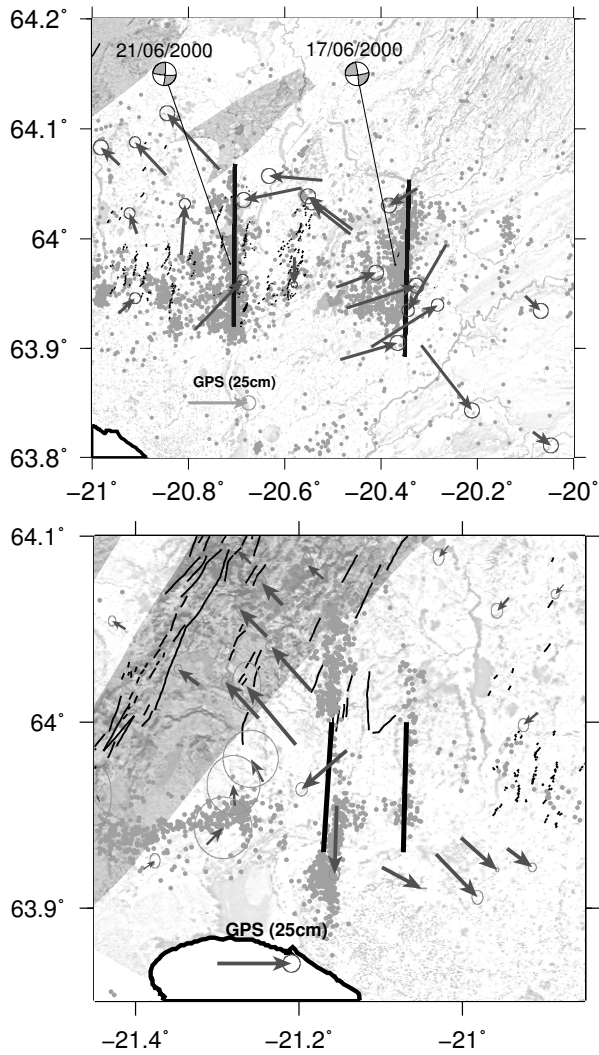
Figure 1.3: Coseismic diplacements recorded with GPS during the June 2000 earthquakes (Upper) and the May 2008 earthquakes (Lower). Black thick lines indicate the location of the modelled faults, gray dots show the location of the recorded aftershocks, determined by the Icelandic Meteorological Office.

1.2　GPS

1.2.1　GPS theory

The American NAVSTAR Global Positioning System (GPS) is part of the Global Navigation Satellite System (GNSS). It is a spaced-based positioning system, allowing the user to get time and position information anywhere on Earth. At present a constellation of 30 GPS satellites orbiting around Earth in 12 hours, on 6 different orbital planes at an altitude of 20,200km. On the ground a world wide network is used to control and monitor the constellation.

Each GPS satellite broadcasts digital signals at two carrier frequencies: the L1 signal (1.57542 GHz) and L2 (1.2276 GHz). Both carriers are modulated with a high rate pseudo-random sequence (PRN), different for each satellite. PRN codes have to be known by the receiver to reconstruct the actual message. Knowing the distance from a receiver and at least 3 satellite positions allows to resolve the location of the receiver in real time with approximately 5-20 m precision.

Earth Science can benefits from GPS to monitor the crustal displacements by getting an absolute position for a given location on the ground. GPS has been used to determine the plate motion rate all over the world at a very precise level (mm/yr).

To achieve this precision, multiple signals from multiple satellites and receivers can be combined together as well as the differentiation of the code (PRN) or of the carrier phase. The observation equation for carriers L1 and L2 for ith satellite and kth receiver are given by:

$$\text{Code}\quad \begin{cases} P_{1k}^i = \varrho_k^i + c\delta_k - c\delta^i + \Delta\varrho_k^i + I_k^i \\ P_{2k}^i = \varrho_k^i + c\delta_k - c\delta^i + \Delta\varrho_k^i + \frac{f_1^2}{f_2^2}I_k^i \end{cases} \tag{1.1}$$

$$\text{Phase}\quad \begin{cases} L_{1k}^i = \varrho_k^i + c\delta_k - c\delta^i + \Delta\varrho_k^i + I_k^i \quad\quad + \lambda_1 n_{1k}^i \\ L_{2k}^i = \varrho_k^i + c\delta_k - c\delta^i + \Delta\varrho_k^i + \frac{f_1^2}{f_2^2}I_k^i \quad + \lambda_1 n_{1k}^i \end{cases}$$

where ϱ is the geometrical distance, c the speed of light, δ_k the receiver clock error, δ^i the satellite clock error, $\Delta\varrho$ the delay due to troposphere refraction, f the carrier frequency, I the delay due to ionosphere refraction, λ the carrier wavelength and n the integer number of cycles (initial phase ambiguity).

We used GPS receivers that can record several days of signal from multiple

satellites, the mm scale accuracy we need is achieved by the post-processing of the observations, during the post-processing we try to estimate all the ambiguities in eq 1.1. For even better results we used mutliple receivers to form the so called differential observations (Dach et al., 2007):

- Single Difference: $L_{Fkl}^i = L_{Fk}^i - L_{Fl}^i$ (2 receivers and 1 satellite)

- Double Differences: $L_{Fkl}^{ij} = L_{Fkl}^i - L_{Fkl}^j$ (2 receivers and 2 satellites)

- Triple Differences: $L_{Fkl}^{ij}(t1) - L_{Fkl}^j(t2)$ (Double difference at 2 epochs)

Those combined observations allow us to estimate some of the error terms: satellite clock error (δ^i) from the single difference, receiver clock error (δ_k) and delay due to ionosphere refraction(δ_l) from the double differences, and initial phase ambiguity (n_{1k}^i) from the triple differences. Estimate of the ambiguities can also be obtained from linear combination of observations:

- $L_3 = \frac{1}{f_1^2 - f_2^2}(f_1^2 L_1 - f_2^2 L_2)$ (Ionosphere-Free)

- $L_4 = L_1 - L_2$ (Geometry-Free)

- $L_5 = \frac{1}{f_1 - f_2}(f_1 L_1 - f_2 L_2)$ (Wide Lane)

- $L_6 = \frac{1}{f_1 - f_2}(f_1 L_1 - f_2 L_2) - \frac{1}{f_1 + f_2}(f_1 P_1 - f_2 P_2)$ (Melbourne-Wubenna)

During this PhD project we process both continuous GPS stations (permanent station streaming the data on a daily basis) and campaign stations (temporary station recording data for days). We use the Bernese V5.0 software (Dach et al., 2007) to calculate daily station position solution. We then combine the obtained daily solutions with global network solutions provided by International GNSS Service (IGS) to obtain the station motions in the International Terrestrial Reference Frame (ITRF) 2005 (Altamimi et al., 2007). We also analyze 1Hz kinematic GPS data, where we compute a solution for each observation (i.e., the receiver recording rate), we were able to produce 1s sampling station timeseries at the time of the May 2008 faults ruptures.

1.2.2 Continuous GPS observations in Iceland

Continuous GPS (CGPS) measurements started in Iceland in 1995 (Geirsson et al., 2006). The network has grown since with 64 CGPS sites by the beginning of 2010, mostly operated by the Icelandic Meteorological office (Geirsson et al., 2010). CGPS provide dense observations in time, close to real time, and set-up errors frequently encountered in campaign measurements are avoided. In a joint effort of several research groups in Iceland, the United States and Switzerland the continuous network in Iceland was expanded with 40 new sites during 2006-2009.
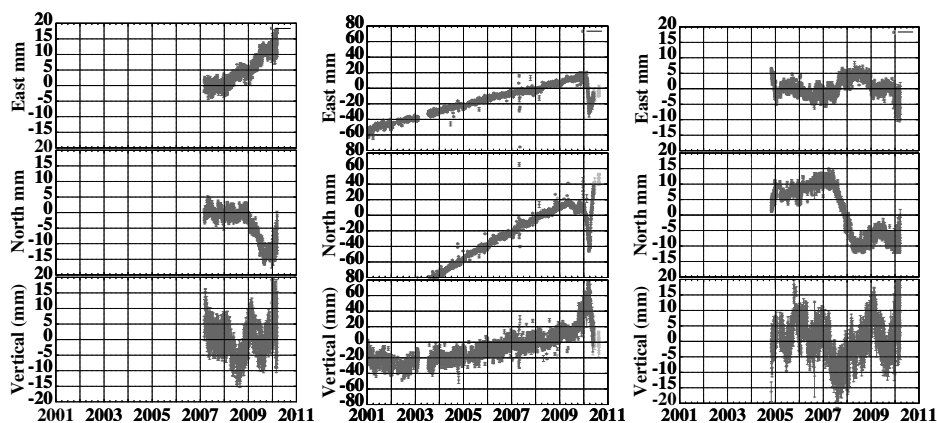
Figure 1.4: Example of CGPS timeseries. Left: KRIV showing uplift in the Krisuvik area. Middle: Deformation South of Eyjafjallajökull recorded by THEY. Right: SAUD showing signs of intrusion north of Vatnajökull ice-cap during 2007 to 2008

Several episodes of volcanic and earthquake deformation have been recorded by the CGPS network in Iceland. The continuous GPS network provides crucial information on the on-going deformation and aids monitoring with the seismic network. An overview of all the deformation signals recorded during 1999-2010 is given in Geirsson et al. (2010).

During this project we have developed an automatic processing procedure, recomputing the solution for the whole CGPS network in Iceland with the Bernese V5.0 software as the data, or the ancilliary files (orbits, atmopshere models and additional stream of data) becomes available. The software provides us with a
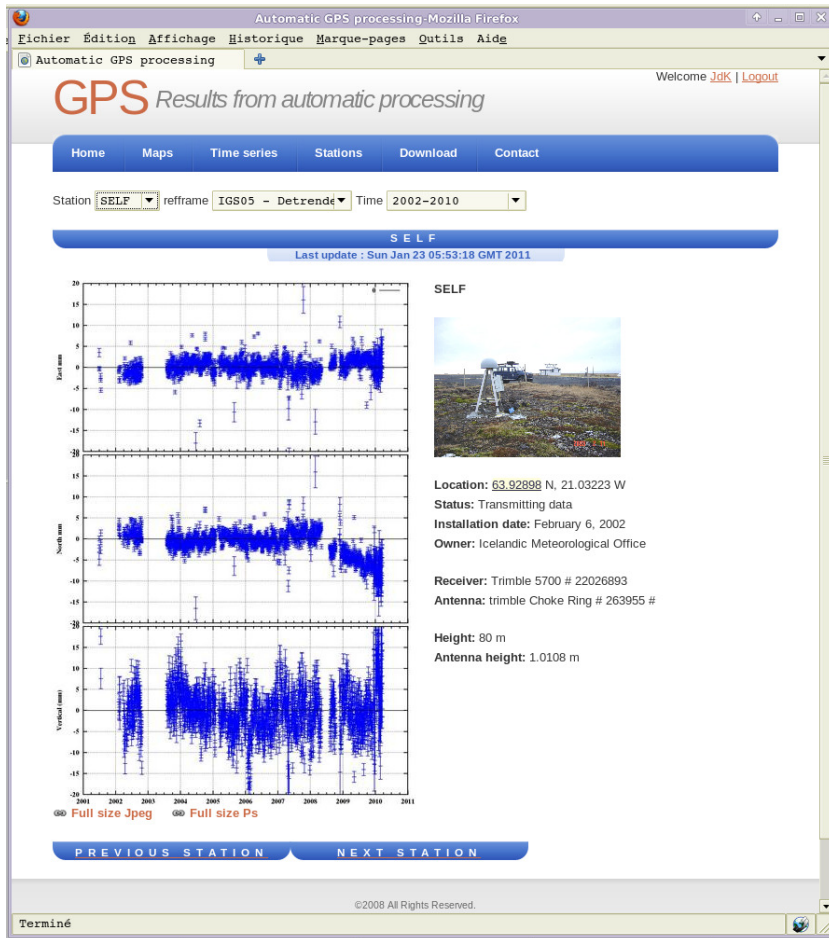
Figure 1.5: Internet web interface (http://www.askja.norvol.hi.is) showing the timeseries from CGPS station SELF in Selfoss, detrended to mimimize seasonal effects and removing the coseismics offset due to the May 2008 earthquakes.

solution for the whole network, with a 24hr delay, and station timeseries since 2001 (Fig. 1.4) can be displayed through a web interface (Fig. 1.5).

1.2.3 GPS campaign observations in South Iceland

Annual campaign style GPS measurements have been conducted in the SISZ and on the Reykjanes Peninsula since June 2000 (Árnadóttir et al., 2006; Keiding et al., 2008). During the campaign measurements each site is normally occupied for at least one 24 hr session. During this PhD project I participate to measurements in this area every year from 2007 to 2009, as well as a dense survey following the May 2008 events (Fig 1.3).

Reference Frame

The absoslute positions obtained directly from GPS pseudorange measurements are based on the 3D Earth centered WGS84 ellipsoid. When studying plate tectonic the reference frame should not be tied to a specific tectonic plate. The International Terrestrial Reference Frame (ITRF) currently gives the best representation of the solid Earth surface. The coordinates of the reference frame are based on combinations of several geodetic space techniques including VLBI, SLR, DORIS and GPS (Altamimi et al., 2007). Therefore, coordinates defined in ITRF will change over time due to the displacement of the plates and possibly to some intra-plate motions. We use the GLOBK software (Herring et al., 2006) to generate a solution using a regional stabilization approach (McClusky et al., 2000). Using a combination of our solutions with three IGS global network solutions (IGS1, IGS3 and EURA) to realize a reference frame approximately aligned with the ITRF2005 (Altamimi et al., 2007), solutions are shown in Fig. 1.6.

1.2.4 High rate GPS observations

Kinematic processing is used to obtain timeseries of station motion, at the same time rate as the receiver acquisition. In the two previous section the GPS measurements have been used to calculate daily solutions, as sufficient when looking at the plate spreading, or slow deformation signals. When studying faster processes such as shaking due to earthquakes, high rate GPS observations are required (Larson et al., 2003; Miyazaki et al., 2004). GPS has the advantage of measuring absolute displacements, whereas seismometers record velocity or ac-
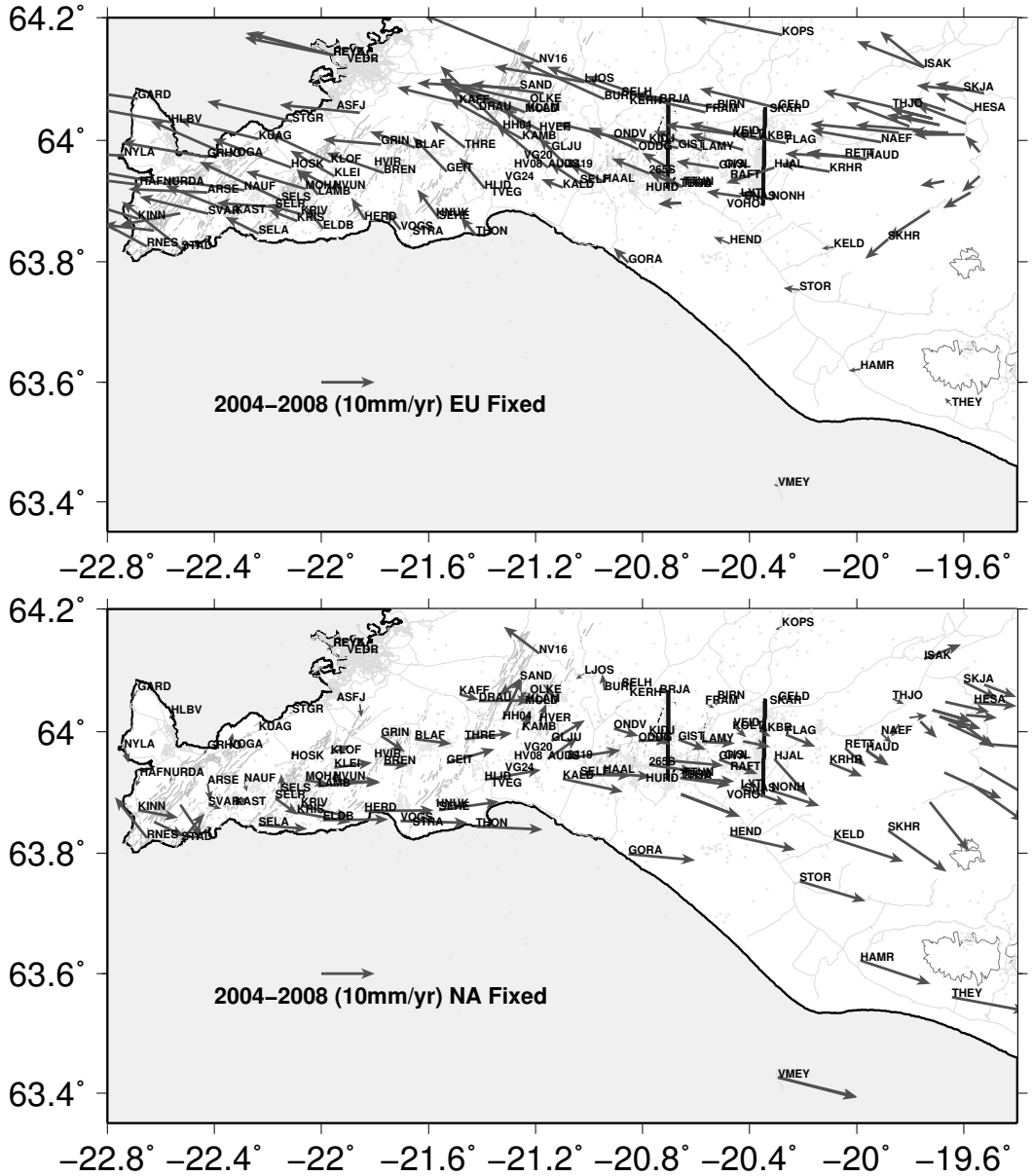
Figure 1.6: GPS velocities in South Iceland relative to Eurasian plate (EU) and North American plate (NA).

celeration. However, uncertainties are much larger in GPS kinematic processing (∼cm) compared to GPS static solutions (∼mm), mostly because atmosphere, multipath (signal reflections from the ground) and orbital effects (Choi et al., 2004) affect the individual observations and are difficult to estimate at this time scale.
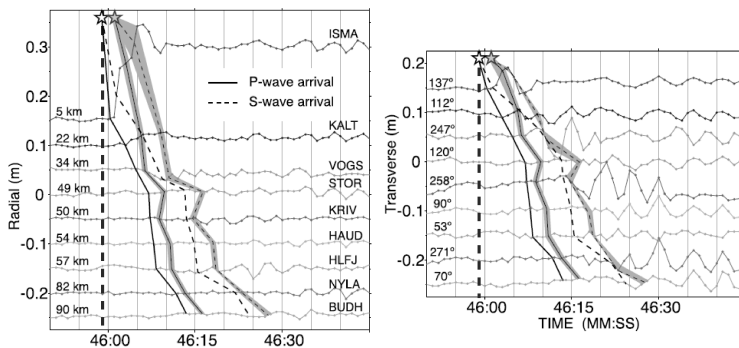
Figure 1.7: Kinematic 1s GPS timeseries from the time of the May 2008 mainshocks. Thick dashed lines indicate the time of the initial rupture (white star 15:45:58.91 UTC) and the estimated arrival times of the first P- and S- waves to each stations are shown with solid and dashed lines respectively. Arrival times from the second event (gray star) are shown assuming a delay of 1.7 to 2.7 s, (Fig from Hreinsdóttir et al. (2009)).

Fortunately several continuous GPS stationin South Iceland were recording 1 Hz data when the May 2008 earthquakes occured. We processed the first high rate GPS kinematic timeseries in Iceland as part of this PhD project (Fig. 1.7). We used the TRACK software (King and Bock, 2006) to analyze the high rate data for 10 CGPS stations. We can get an approximation of the ground displacements, indicating when the seismic waves reach each station. The 1Hz data analysis was used by Hreinsdóttir et al. (2009) to conclude that the two mainshocks on 29 May 2008 occured within ∼3 sec of each other.

1.3 InSAR

1.3.1 InSAR theory

Interferometric Synthetic Aperture Radar (InSAR) is a widely used technique to measure the Earth's surface deformation from space. The concept is to derive the surface displacements from the phase difference between two Synthetic Aperture Radar (SAR) images, acquired from approximately the same position in space. The field is very active and techniques and new sensors are being developed by most of the space agencies. Compared to GPS, radar interferometry provides precise measurements over wide areas, but only in one dimension since the deformation is measured along the Line of Sight (LOS) between the satellite and the ground. However, the orbit of the spacecraft can be divided in two parts: the ascending and the descending arc of the orbit, providing two differents observation geometries for InSAR. The actual spacecrafts operating SAR instruments are Envisat and Radarsat working in the C-Band, Alos in L-Band, and TerraSAR-X in the X-Band.

The phase differences ϕ between two acquisitions is given by:

$$\phi = -\frac{4\pi}{\lambda}\Delta r \tag{1.2}$$

where λ is the wavelength of the radar wave, Δr is the range difference between the sensor and the ground. If there is no deformation Δr only depends on the geometry, i.e., of the height of the satellite above the Earth's surface. This height is given by the topography and the curvature of the Earth. Using a reference ellipsoid for the Earth and a digital elevation model (DEM) for the topography, we can estimate the contribution of both the Earth curvature and the topography. Substracting this from the interferogram leaves only phase difference due to surface deformation. However, the absolute phase is not known and we only get a measurement modulo 2π, but it is possible to estimate the relative height between all points, this process is called the "phase unwrapping" and consist in integrating all the differencial phases between all neighboring pixels over the interferogram. However, the unwrappring solution is non unique because of data gaps and/or relative phase jumps greater than π.

The quality of the interferogram is affected by many factors, such as Doppler Centroid difference, baseline, atmospheric effect. The error magnitude can be

estimated statistically, we present such estimate in an earlier paper (Decriem et al., 2010) following (Hooper et al., 2007).

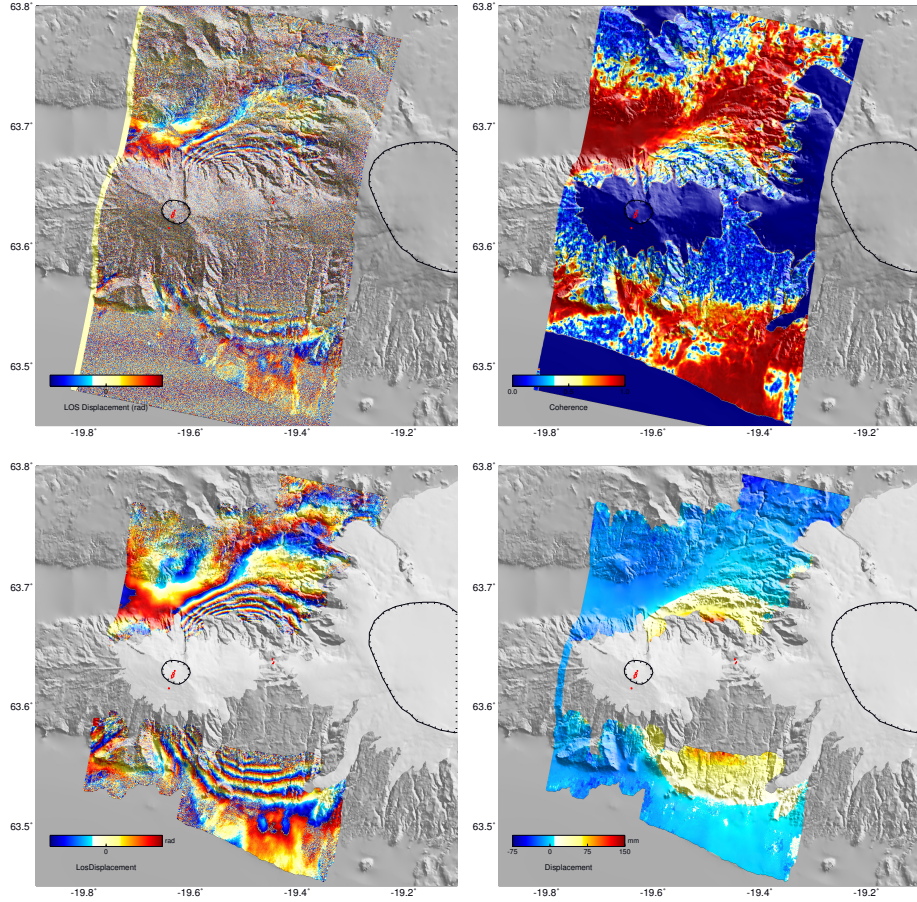## 1.3.2 Single interferogram unwrapping

Figure 1.8: Single interfergogram unwrapping. From left to right: original wrapped phase, coherence, filtered wrapped phase, unwrapped displacements. The interferogram shows an intrusive episode prior to the 2010 Eyjafjallajökull eruption.

Here we present the steps we use to unwrap a single interferogram. The unwrapping is done with statistical-cost, network-flow algorithm from the snaphu software (Chen and Zebker, 2002). For accurate phase unwrapping the interferogram has to be cleaned by masking out incoherent area and should not include isolated groups of pixels. The unwrapping is done using the following:

- Phase Filtering: We use Goldstein filtering to partly attenuate the initial noise from the original phase, the spatial resolution of the filter adapts to the local phase variation: areas of smooth phase are strongly filtered, whereas regions with high phase variance are weakly filtered.

- Coherence Filtering: We calculate the coherence of the interferogram and remove all the pixels with coherence lower than a given threshold.

- Isolated pixels: During the first two steps we remove all the incoherent area, but some of the coherent regions can be isolated, i.e., meaningless for the unwrapping. To remove those areas we use a mathematical morphological filtering (opening filter).

The resulting cleaned phase is shown in Fig 1.8. We use this method to unwrap all the interferograms in Sigmundsson et al. (2010).

1.3.3 InSAR timeseries analysis

Timeseries analysis is uses to minimize the effect of the spatial and temporal decorrelation in InSAR. With multiple acquisition it is possible to improve the interferogram timeseries. There are two main methods for timeseries analysis:

Persistent Scatterer (PS) : Only the best resolution elements dominated by a bright scatterer are selected. This is done by determining the change in signal phase, over time, of a particular, stable radar reflector.

Small Baselines (SB) : Selecting the image pair within the dataset that minimize the temporal baseline (time between the two images used to form the interferogram) and the spatial baseline (distance of the satellite between the two acquisitions). Such analysis has be done using StaMPS/MTI Software (Hooper et al., 2007, 2009). We applied the timeseries analysis in Decriem et al. (2010) (Fig 1.9).
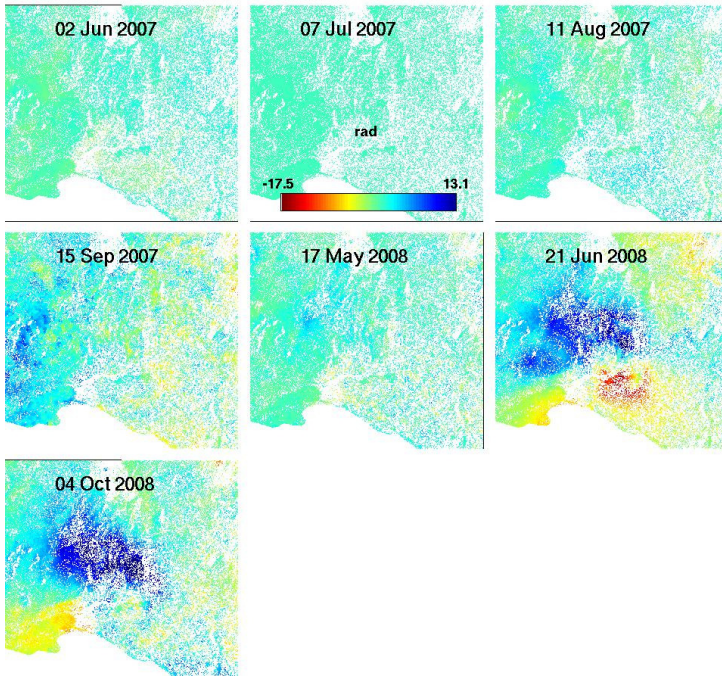
Figure 1.9: Small baseline timeseries analysis. The area shown is the epicentral area of the May 29 earthquakes in 2008.

With both techniques the interferograms are then subjected to various numerical and statistical analyses to identify and remove effects such as atmospheric distortions of signal phase and other noise generators such as vegetation, erosion and adverse acquisition geometry.

1.3.4 Data partitioning

An InSAR image may contain several hundred thousand data points. For more efficient modelling, we explore different schemes in order to reduce the number of points without loosing critical information. We test two different methods: an adaptive quadtree subsampling similar to Jónsson et al. (2002) and a method dividing the area into polygons rather than squares. We apply our methods in the geographic space rather than the pixel space, where the squares/polygons are defined as the spatial envelope around a group of pixels.
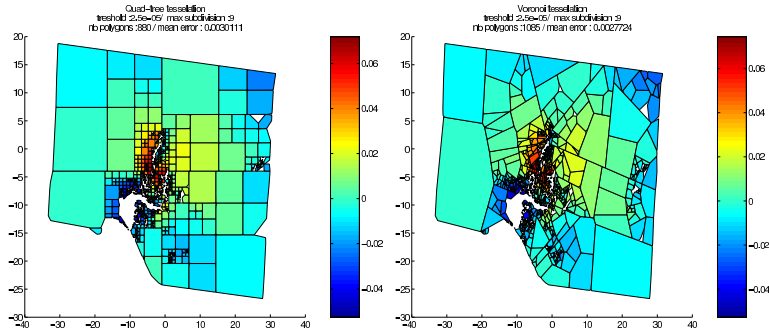
Figure 1.10: Data partitioning using quad-tree (left) and polygon-tree (right).

The polygon-tree is not more efficient than the simple quad-tree (Fig. 1.10). However, compared to Jónsson et al. (2002) our approach within the geographic space is more efficient. Using the spatial envelope implies that our polygons can be irregularly aligned, also the shape of a group of pixels close to data gaps do not result in subdvision to adapt to the shape of the gap. The number of subdivisions is then reduced compared to Jónsson et al. (2002) without any loss of information. This implementation of the quad-tree algorithm in the geographic space was used in the studies by Decriem et al. (2010), Keiding et al. (2010), and Sigmundsson et al. (2010).

1.4 Modelling

1.4.1 Elasticity

The elastic regime is characterized by a linear relationship between stress and strain. This relationship is called Hooke's law and was first stated in 1675. The classic example of elastic material is a metal spring. The isotropic linear elastic stress-strain relation is given by:

$$\sigma_{ij} = \lambda\epsilon_{kk}\delta_{ij} + 2\mu\epsilon_{ij} \tag{1.3}$$

where σ and ϵ are the stress and strain tensor respectively, δ_{ij} the Kronecker delta, λ is the Lamé constant and μ is the shear modulus. An equivalent notation in terms of E the Young's modulus and ν the Poisson's ratio is:

$$\epsilon_{ij} = -\frac{\nu}{E}\sigma_{kk}\delta_{ij} + \frac{1+\nu}{E}\sigma_{ij} \tag{1.4}$$

On short time scale, during earthquake faulting for example, the Earth behaves elastically, except at fault plane itself and its immediate surrounding. Okada (1992) derives the expressions for coseismic displacement u at the Earth's surface caused by a fault at depth in an elastic halfspace in analytic form. The surface displacements are a non-linear function of the location and geometry of the source, and a linear function of the amount of slip. More detailed study on the methods to solve for the fault geometry (non-linear) and the slip distribution over the previously defined fault plane (linear) are given in Decriem et al. (2010).

1.4.2 Viscoelasticity

Viscoelastic materials have properties of both of viscous materials, which resist shear flow and strain linearly with time when a stress is applied, and elastic materials, which strain instantaneously and return quickly to their original state. As such, viscoelastic materials exhibit time dependent strain. Typical viscoelastic material are glasses, rubbers and synthetic polymers. Rocks behave viscoelastically over long time scale or at elevated temperatures. Different rheological models are used to describe the viscoelastic response under different loading conditions. Materials behaving according to these models are calledthe Maxwell

material, the Kelvin-Voigt, the Standard Linear Solid (SLS), and the Burgers Body, depending on the type of the rheology. The rheology in the models is often described by mechanical analogs, i.e., linear combinations of springs (elastic response) and dashpots (viscous response) and are shown in Fig 1.11.

The Maxwell material can be represented by a dashpot and a spring connected in series. When the material is put under a constant strain, the stresses decay exponentially with time, following the equation:

$$\frac{d\epsilon_{Total}}{dt} = \frac{\sigma}{\eta} + \frac{1}{E}\frac{d\sigma}{dt} \qquad (1.5)$$

Where η is the viscosity of the dashpot, and the Young Modulus (E). One limitation of this model is that for constant-stress conditions the strain increases linearly with time. However, under this condition most materials show strain rate decreasing with time.

The Kelvin-Voigt material can be represented by a dashpot and a spring connected in parallel. Under constant stress, the material deforms at a decreasing rate, when the stress is released, the material gradually relaxes to its undeformed state folowing:

$$\sigma(t) = E\epsilon(t) + \eta\frac{d\epsilon(t)}{dt} \qquad (1.6)$$

The Standard Linear Solid (SLS) material combines the Maxwell model with an additionnal spring in parallel with the dashpot. Under a constant stress, the modeled material will instantaneously deform to some strain, and after that it will continue at a decreasing rate. Under a constant strain it behaves similar to the Maxwell model. The governing equation for SLS is:

$$\frac{d\epsilon}{dt} = \frac{\frac{E_2}{\eta}\left(\frac{\eta}{E_2}\frac{d\sigma}{dt} + \sigma - E_1\epsilon\right)}{E_1 + E_2} \qquad (1.7)$$

The Burgers Body material is a Maxwell and a Kelvin-Voigt elements in series. Under constant stress it is similar to SLS with an additionnal unre-

coverable deformation. The governing equation is:

$$\epsilon = \sigma \left(\frac{1}{3G} \left(1 - e^{-G\frac{t}{\nu_1}}\right) + \frac{t}{3\nu_2} \right) \qquad (1.8)$$

with the Shear Modulus (G). We compared three semi-analytical codes that caculate transient deformation after faulting: visco1d (Pollitz and Sack, 1996), psgrn/pscmp (Wang et al., 2006) and v2foait (Fukahata and Matsu'ura, 2005, 2006). We use the software psgrn/pscmp, assuming viscoelastic relaxation following the 2000 and 2008 earthquakes in the SISZ to obatin estimates of the crustal thickness and mantle viscosity in Decriem and Árnadóttir (2011).
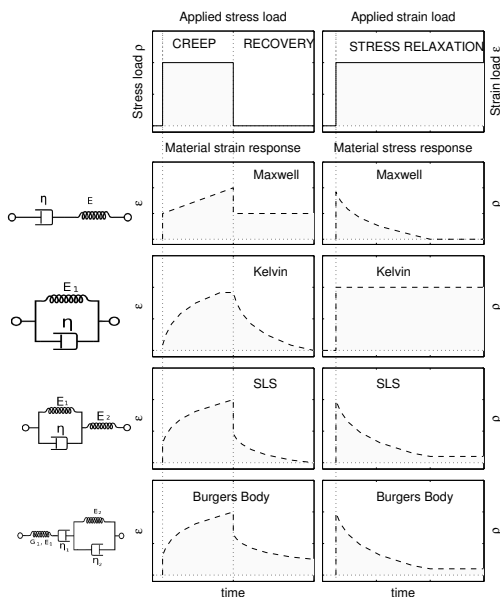
Figure 1.11: Viscoelastic material behaviour under stress and strain load. The applied constraints are shown in the first row, the material response for the Maxwell model, the Kelvin-Voigt model, the Standard Linear Solid model, and the Burgers Body model are shown in the following rows. Schematic representations of the models using springs and dashpots are shown in the first column.

21

1.4.3 Poroelasticity

A porous medium or a porous material is a solid permeated by an interconnected network of pores filled with a fluid. The general description of the mechanical behaviour of a poroelastic medium was describe by Biot (1941). The total stress formulation is given by:

$$\sigma_{ij} = 2G\epsilon_{ij} + (K - \frac{2}{3}G)\epsilon_{kk}\delta_{ij} - \alpha\delta_{ij}pV = \alpha\epsilon_{kk} + \frac{\phi^2}{R}p \qquad (1.9)$$

where $\alpha = \phi(1 + \frac{Q}{R})$ Biot's stress coefficient, p the pore pressure, V the variation of fluid volume per reference volume, ϕ the porosity, R and Q material constants for solid/fluid interaction,

A simple way to calculate the elastic deformation due poroelastic relaxation after an earthquake is to calculate the difference of the coseismic deformation under drained and undrained condition. The undrained condition corresponds to the time interval where the rate of elastic loading is greater than the rate at which pore water pressure may dissipate. The drained state corresponds to the deformation once the pore water has been dissipated. The elastic deformation resulting from the pore pressure dissipation is then given by the difference between the undrained and drained solution. Jónsson et al. (2003) represent the drained and undrained solution by a difference in the Poisson's ratio (0.31 for the undrained and 0.25 for the drained conditions). We calculate poroelastic deformation as well as pore pressure relaxation in Decriem et al. (2011).

Abbreviations and Symbols

CGPS   Continuous GPS

DEM   digital elevation model

E   the Young Modulus

EVZ   Eastern Volcanic Zone

EU   Eurasian plate

G   the Shear Modulus

IGS   International GNSS Service

GNSS   Global Navigation Satellite System

GPS   Global Positioning System

InSAR   Interferometric Synthetic Aperture Radar

ITRF   International Terrestrial Reference Frame

LOS   Line of Sight

MAR   Mid-Atlantic Ridge

NA   North American plate

PRN   pseudo-random sequence

PS   Persistent Scatterer

RP   Reykjanes Peninsula

SAR   Synthetic Aperture Radar

SISZ   South Iceland Seismic Zone

SB   Small Baselines

SLS   Standard Linear Solid

WVZ   Western Volcanic Zone

Bibliography

Altamimi, Z., Collilieux, X., Legrand, J., Garayt, B., and Boucher, C. (2007). ITRF2005: A new release of the International Terrestrial Reference Frame based on time series of station positions and Earth Orientation Parameters. *J. Geophys. Res.*, 112:B09401, doi:10.1029/2007JB004949.

Árnadóttir, T., Geirsson, H., and Einarsson, P. (2004). Coseismic stress changes and crustal deformation on the Reykjanes Peninsula due to triggered earthquakes on 17 June 2000. *J. Geophys. Res.*, 109:B09307, doi: 10.1029/2004JB003130.

Árnadóttir, T., Hreinsdóttir, S., Gudmundsson, G., Einarsson, P., Heinert, M., and Völksen, C. (2001). Crustal deformation measured by GPS in the South Iceland Seismic Zone due to two large earthquakes in June 2000. *Geophys. Res. Lett.*, 28:4031–4033.

Árnadóttir, T., Jiang, W., Feigl, K. L., Geirsson, H., and Sturkell, E. (2006). Kinematic models of plate boundary deformation in southwest Iceland derived from GPS observations. *J. Geophys. Res.*, 111:B07402, doi: 10.1029/2005JB003907.

Árnadóttir, T., Jónsson, S., Pedersen, R., and Gudmundsson, G. B. (2003). Coulomb stress changes in the South Iceland Seismic Zone due to two large earthquakes in June 2000. *Geophys. Res. Lett.*, 30(5):1205, doi: 10.1029/2002GL016495.

Bellou, M., Bergerat, F., Angelier, J., and Homberg, C. (2005). Geometry and segmentation mechanisms of the surfaces traces associated with the 1912 Selsund earthquake, southern Iceland. *Tectonophysics*, 404:133–149.

Biot, M. (1941). General theory of three dimensional consolidation. *J. Appl. Phys.*, 12:155–169.

Bjarnason, I., Cowie, P., Anders, M. H., Seeber, L., and Scholz, C. H. (1993a). The 1912 Iceland earthquake rupture: Growth and development of a nascent transform system. *Bull. Seismol. Soc. Am.*, 83:416–435.

Bjarnason, I., Menke, W., Flóvenz, Ó. G., and Caress, D. (1993b). Tomographic image of the mid-Atlantic plate boundary in southwestern Iceland. *J. Geophys. Res.*, 98:6607–6622.

Brandsdóttir, B., Parsons, M., White, R. S., Gudmundsson, O., Drew, J., and Thorbjarnadóttir, B. (2010). The may 29 2008 earthquake aftershock sequence within the South Iceland Seismic Zone: Fault locations and source parameters of aftershocks. *Jökull: journal of the glaciological and geological societies of Iceland*, 60:23–46.

Chen, C. W. and Zebker, H. A. (2002). Phase unwrapping for large SAR interferograms: Statistical segmentation and generalized network models. *IEEE Transactions on Geoscience and Remote Sensing*, 40:1709–1719.

Choi, K., Bilich, A., Larson, K., and Axelrad, P. (2004). Modified Sidereal Filtering: Implications for High-Rate GPS Positioning. *Geophys. Res. Lett.*, 31.

Clifton, A. E. and Einarsson, P. (2005). Styles of surface rupture analysis accompanying the June 17 and 21, 2000 earthquakes in the South Iceland Seismic Zone. *Tectonophysics*, 396:141–159.

Clifton, A. E., Pagli, C., Jónsdóttir, J. F., Eythórsdóttir, K., and Vogfjörd, K. (2003). Surface effects of triggered fault slip on Reykjanes Peninsula, SW Iceland. *Tectonophysics*, 369:145–154.

Dach, R., Hugentobler, U., Fridez, P., and Meindl, M. (2007). Bernese GPS software version 5.0. Technical report, Astronomical Institute, University of Bern, Bern, Switzerland.

Decriem, J. and Árnadóttir, T. (2011). Transient crustal deformation in the South Iceland Seismic Zone observed by GPS and InSAR during 2000-2008. *submitted to Tectonophysics*.

26

Decriem, J., Árnadóttir, T., Hooper, A., Geirsson, H., Sigmundsson, F., Keiding, M., Ófeigsson, B. G., Hreinsdóttir, S., Einarsson, P., LaFemina, P. C., and Bennett, R. (2010). The 2008 May 29 earthquake doublet in SW Iceland. *Geophys. J. Int.*, 181:1128–1146.

Decriem, J., Árnadóttir, T., Hreinsdóttir, S., Hooper, A., Geirsson, H., LaFemina, P. C., and Bennett, R. (2011). Postseismic relaxation following the May 2008 earthquakes South Iceland. *submitted to Geophys. J. Int.*

Einarsson, P. (1991). Earthquakes and present-day tectonism in Iceland. *Tectonophysics*, 189:261–279.

Einarsson, P. (2010). Mapping of Holocene surface ruptures in the South Iceland Seismic Zone. *Jökull*, 60:117–134.

Einarsson, P., Björnsson, S., Foulger, G., Stefánsson, R., and Skaftadóttir, T. (1981). Seismicity pattern in the South Iceland Seismic Zone. In Simpson, D. W. and Richards, P. G., editors, *Earthquake Prediction – An international review*, volume 4, pages 141–151. AGU, Washington D.C.

Einarsson, P. and Eiríksson, J. (1982). Earthquake fractures in the districts Land and Rangárvellir in the South Iceland Seismic Zone. *Jökull*, 32:113–120.

Einarsson, P. and Sæmundsson, K. (1987). Earthquake epicenters 1982–1985 and volcanic systems in Iceland. A map accompanying festschrift for Th. Sigurgeirsson. In Sigfusson, T., editor, *Í hlutarins edli*. Menningarsjódur, Reykjavík, Iceland.

Fukahata, Y. and Matsu'ura, M. (2005). General expressions for internal deformation fields due to a dislocation source in a multiayered elastic half-space. *gji*, 161:507–521.

Fukahata, Y. and Matsu'ura, M. (2006). Quasi-static internal deformation due to a dislocation source in a multilayered elastic/viscoelastic half-space and an equivalence theorem. *Geophys. J. Int.*, 166:418–434.

Geirsson, H., Árnadóttir, T., Völksen, C., Jiang, W., Sturkell, E., Villemin, T., Einarsson, P., and Sigmundsson, F. (2006). Current plate movements across the

Mid-Atlantic ridge determined from 5 years of continuous GPS measurements in Iceland. *J. Geophys. Res.*, 111:B09407, doi: 10.1029/2005JB003717.

Geirsson, H., Árnadóttir, T., Hreinsdóttir, S., Decriem, J., LaFemina, P., Jónsson, S., Bennett, R. A., Metzger, S., Holland, A., Sturkell, E., Villemin, T., Völksen, C., Sigmundsson, F., Einarsson, P., Roberts, M. J., and Sveinbjörnsson, H. (2010). Overview of results from continuous GPS observations in Iceland from 1995 to 2010. *Jökull*, 60:3–22.

Herring, T. A., King, R. W., and McClusky, S. C. (2006). GLOBK reference manual, Global Kalman filter VLBI and GPS analysis program, release 10.3. Technical report, Mass. Inst. Technol., Cambridge, MA, USA.

Hooper, A., Pedersen, R., and Sigmundsson, F. (2009). Constrains on magma intrusion at Eyjafjallajokull and Katla volcanoes in Iceland from time series SAR interferometry. In et al., C., editor, *The VOLUME Project, VOLcanoes : understanding subsurface mass moveMEnt.*, pages 13–24.

Hooper, A., Segall, P., Johnson, K., and Zebker, H. A. (2007). Persistent Scatterer InSAR for Crustal Deformation Analysis, with Application to Volcan Alcedo, Galapagos. *J. Geophys. Res.*, page 2062.

Hreinsdóttir, S., Árnadóttir, T., Decriem, J., Geirsson, H., Tryggvason, A., Bennett, R. A., and LaFemina, P. (2009). A complex earthquake sequence captured by the continuous GPS network in SW Iceland. *Geophys. Res. Lett.*, 36:L12309.

Jónsson, S., Segall, P., Pedersen, R., and Björnsson, G. (2003). Post-earthquake ground movements correlated to pore-pressure transients. *Nature*, 424:179–183.

Jónsson, S., Zebker, H. A., Segall, P., and Amelung, F. (2002). Fault slip distribution of the 1999 M_w7.2 Hector Mine earthquake, California, estimated from satellite radar and GPS measurements. *Bull. Seismol. Soc. Am.*, 92:1377–1389.

Keiding, M., Árnadóttir, T., Jónsson, S., Decriem, J., and Hooper, A. (2010). Plate boundary deformation and man-made subsidence around geothermal fields on the Reykjanes Peninsula, Iceland. *Journal of Volcanology and Geothermal Research*, 194:139–149.

Keiding, M., Árnadóttir, T., Sturkell, E., Geirsson, H., and Lund, B. (2008). Strain accumulation along an oblique plate boundary: The Reykjanes Peninsula, southwest Iceland. *Geophys. J. Int.*, 172(1):861–872, doi:10.1111/j.1365–246X.2007.03655.x.

King, R. W. and Bock, Y. (2006). GAMIT reference manual, GPS Analysis at MIT, release 10.3. Technical report, Mass. Inst. Technol., Cambridge, MA, USA.

Larson, K., Bodin, P., and Gomberg, J. (2003). Using 1 hz GPS Data to measure Deformations caused by the Denali Fault Earthquake. *Science*, 300:1421–1424.

Lindman, M. (2009). *Physics of aftershocks in the South Iceland Seismic Zone*. PhD thesis, Faculty of Science and Technology, Uppsala University, Uppsala, Sweden.

McClusky, S. et al. (2000). Global Positioning System constraints on plate kinematics and dynamics in the eastern Mediterranean and Caucasus. *J. Geophys. Res.*, 105(B3):5695–5720.

Miyazaki, S., Larson, K., Choi, K., Hikima, K., Koketsu, K., Bodin, P., Haase, J., Emore, G., and Yamagiwa, A. (2004). Modeling the rupture process of the 2003 Tokachi-Oki (Hokkaido) earthquake using 1-hz GPS data. *Geophys. Res. Lett.*, 31.

Okada, Y. (1992). Internal deformation due to shear and tensile faults in a half-space. *Bull. Seismol. Soc. Am.*, 82:1018–1040.

Pagli, C., Pedersen, R., Sigmundsson, F., and Feigl, K. L. (2003). Triggered seismicity on June 17, 2000 on Reykjanes Peninsula, SW-Iceland captured by radar interferometry. *Geophys. Res. Lett.*, 30(6):1273, doi:10.1029/2002GL015310.

Pedersen, R., Jónsson, S., Árnadóttir, T., Sigmundsson, F., and Feigl, K. L. (2003). Fault slip distribution of two M_w=6.5 earthquakes in South Iceland estimated from joint inversion of InSAR and GPS measurements. *Earth Planet. Sci. Lett.*, 213:487–502.

Pedersen, R., Sigmundsson, F., Feigl, K. L., and Árnadóttir, T. (2001). Coseismic interferograms of two M_s=6.6 earthquakes in the South Iceland Seismic Zone, June 2000. *Geophys. Res. Lett.*, 28:3341–3344.

Pollitz, F. F. and Sack, S. (1996). Viscosity structure beneath northeast iceland. *J. Geophys. Res.*, 101:771–793.

Sigmundsson, F., Einarsson, P., Bilham, R., and Sturkell, E. (1995). Rift-transform kinematics in south Iceland: Deformation from Global Positioning System measurements, 1986 and 1992. *J. Geophys. Res.*, 100:6235–6248.

Sigmundsson, F., Hreinsdóttir, S., Hooper, A., Árnadóttir, T., Pedersen, R., Roberts, M. J., Óskarsson, N., Auriac, A., Decriem, J., Einarsson, P., Geirsson, H., Hensch, M., Ófeigsson, B. G., Sturkell, E., Sveinbjörnsson, H., and Feigl, K. L. (2010). Intrusion triggering of the 2010 Eyjafjallajökull explosive eruption. *Nature*, 468(7322):426–430.

Stefánsson, R. and Halldórsson, P. (1988). Strain release and strain build-up in the south Iceland seismic zone. *Tectonophysics*, 152:267–276.

Vogfjörd, K. S. (2003). Triggered seismicity in SW Iceland after the June 17, M_w=6.5 earthquake in the South Iceland Seismic Zone: The first five mintues. In *Geophys. Res. Abs.* EAE03-A-11251, vol. 5, European Geosciences Union.

Wang, R., Lorenzo-Martin, F., and Roth, F. (2006). Psgrn/pscmp- a new code for calculating co- and post-seismic deformation, geoid and gravity changes based on the viscolelastic-gravitational dislocation theory. *"Computers and Geosciences"*, 32:527–541.

Peer-reviewed articles

Decriem J., Árnadóttir Th., Hooper A., Geirsson H., Sigmundsson F., Keiding M., Ófeigsson B.G., Hreinsdóttir S., Einarsson P., LaFemina P.C., and Bennett R.A., The 2008 May 29 earthquake doublet in SW Iceland, *Geophysical Journal International*, doi:10.1111/j.1365-246X.2010.04565.x

The 2008 May 29 earthquake doublet in SW Iceland

J. Decriem,[1] T. Árnadóttir,[1] A. Hooper,[2] H. Geirsson,[3] F. Sigmundsson,[1] M. Keiding,[1] B. G. Ófeigsson,[1] S. Hreinsdóttir,[4] P. Einarsson,[1] P. LaFemina[5] and R. A. Bennett[4]

[1]*Nordic Volcanological Center, Institute of Earth Sciences, University of Iceland, IS-101 Reykjavík, Iceland. E-mail: judicael@hi.is*
[2]*Delft Institute of Earth Observation and Space Systems (DEOS), Delft University of Technology, Delft, Netherlands*
[3]*Physics Department, Icelandic Meteorological Office, Reykjavík, Iceland*
[4]*Department of Geosciences, University of Arizona, Tucson, AZ, USA*
[5]*Department of Geosciences, Pennsylvania State University, University Park, PA, USA*

SUMMARY

On 2008 May 29 an earthquake doublet shook the southwestern part of Iceland. The first main shock originated beneath Mt Ingólfsfjall, located near the western margin of the South Iceland Seismic Zone (SISZ) approximately 40 km east of the capital Reykjavík. Immediate aftershock activity was recorded by the SIL seismic network, operated by the Icelandic Meteorological Office (IMO), with both N–S and E–W structures illuminated over a broad area. A continuous GPS (CGPS) network, also operated by the IMO, recorded coseismic offsets with up to 200 mm of horizontal motion at the closest stations. We estimate the coseismic surface deformation observed by campaign and continuous GPS and satellite radar data (InSAR). We invert the geodetic data to find the optimal geometry, location and slip on the main faults, accounting for variation in the elastic parameters of the crust with depth. Our models indicate that most of the slip occurred on two N–S structures spaced ∼5 km apart. From a joint inversion of GPS and InSAR data for variable slip models we find that most of the slip for the first (Ingólfsfjall) event was concentrated at 2–4 km depth with a maximum of 1.9 m, whereas the slip on the second (Kross) fault was located deeper, at 3–6 km depth with up to 1.4 m of motion. The models give similar geodetic moments for the two main events, equivalent to a moment magnitude of $M_w5.8$ and $M_w5.9$ for the first and second event, respectively. Our estimated composite moment therefore equals a $M_w6.1$ for the doublet, smaller than the $M_w6.3$ estimated from teleseismic data (e.g. NEIC and Harvard).

The geodetic data support rupture on two main faults and analysis of high-rate (1 Hz) CGPS data suggests that slip on the second fault initiated within 3 s of the first main shock. Static Coulomb failure stress calculations indicate that the first event caused a stress increase in the area of the main asperity (i.e. at the location of the largest slip patch) on the second fault. However, we cannot rule out dynamic stress triggering due to the short time between the two main events. The 2008 May 29 earthquake doublet appears to be a continuation of the earthquake sequence that started in 2000 June, when two $M_w6.5$ events struck the eastern and central part of the South Iceland Seismic Zone, in the span of 81 hr. The 2000 June–2008 May sequence has released about half of the moment accumulated by plate motion since the previous earthquake sequence in 1896–1912. Therefore, continued earthquake activity with moderate size events rupturing N–S faults in the SISZ in the coming decades is likely.

Key words: Satellite geodesy; Space geodetic surveys; Earthquake source observations; Seismicity and tectonics.

1 INTRODUCTION

Iceland is the largest subaerial part of the Mid-Atlantic Ridge, the boundary between the North American and Eurasian plates. The rate of plate divergence across Iceland is ∼19 mm yr^{-1} causing major seismic and volcanic activity in the island. The Reykjanes Peninsula is the onshore extension of the Reykjanes Ridge in southwest Iceland, characterized by oblique spreading as the direction of relative plate motion deviates by ∼30° from the trend of the plate boundary axis. The Hengill triple junction marks the intersection of the Reykjanes Peninsula (RP), the Western Volcanic Zone (WVZ) extending to the north, and the South Iceland Seismic Zone (SISZ)
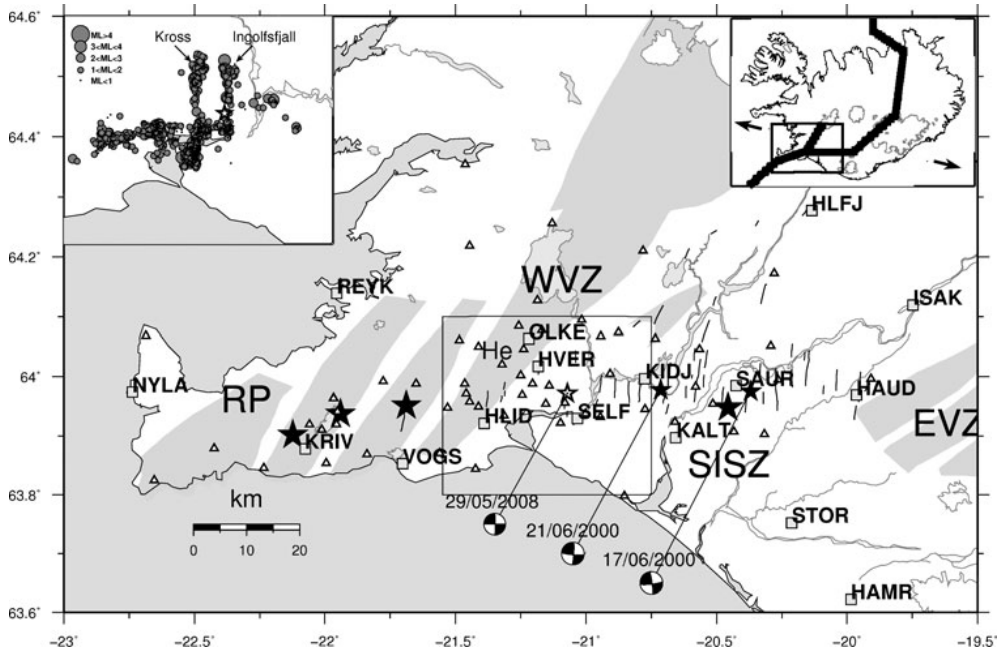
GJI Seismology

Figure 1. The main tectonic features in the study area: the Reykjanes Peninsula (RP), the Hengill triple junction (He), the Western and Eastern Volcanic Zones (WVZ and EVZ, respectively) and the South Iceland Seismic Zone (SISZ). Individual fissure swarm are shown in light grey. The stars indicate the epicentres of $M_w > 5$ events in 2000 June (black) and the initial 2008 May 29 main shock (white). The focal mechanisms are from the USGS. The white triangles denote GPS campaign sites and grey squares the continuous GPS stations. The right-hand inset shows the plate boundary across Iceland and the location of the study area is indicated with a rectangle. The black arrows show the plate spreading according to the NUVEL-1A plate motion model (DeMets *et al.* 1994). The inset to the left-hand side shows the epicentre of 2008 May 29 main shock (white star) and aftershocks (grey circles) recorded by the SIL seismic network from 2008 June 2 to 2008 July 10. The circles are scaled to represent the local magnitude (M_L).

(Fig. 1). The SISZ is an approximately 80-km-long E–W transform zone accommodating left-lateral shear, due to the plate spreading in South Iceland. The eastern end of the SISZ joins the Eastern Volcanic Zone (EVZ), where most of the extension across south Iceland is currently taking place.

The SISZ is characterized by arrays of N–S right lateral strike-slip faults, spaced 2–5 km apart (Einarsson 1991; Clifton & Einarsson 2005). Each of the N–S faults is composed of an array of left step-ping *en echelon* surface fractures, separated by push-up structures (e.g. Bjarnason *et al.* 1993b; Clifton & Einarsson 2005). Earthquake activity in south Iceland has been recorded by the SIL seismic net-work (Stefánsson *et al.* 1993) operated by the IMO, since 1989. Micro-earthquakes (down to magnitude less than zero) have been used to map active fault surfaces at depth (Hjaltadóttir 2009). Stud-ies following the 2000 June earthquake sequence indicate that the larger faults are nearly vertical, planar features extending to approx-imately 10 km depth, although complicated fracture patterns have in some cases been mapped at the surface (e.g. Clifton & Einarsson 2005; Hjaltadóttir 2009).

Global Positioning System (GPS) observations have been used to document crustal deformation in Iceland since 1986 (Foulger *et al.* 1987). A network of continuous GPS (CGPS) stations, operated by the Icelandic Meteorological Office (IMO), has been expanding since 1999 (Geirsson *et al.* 2006). Many previous geodetic studies in SW Iceland address plate spreading (e.g. Hreinsdóttir *et al.* 2001; LaFemina *et al.* 2005; Árnadóttir *et al.* 2006; Keiding *et al.* 2008),

while others focus on earthquake deformation (e.g. Árnadóttir *et al.* 2001; Pedersen *et al.* 2001, 2003; Jónsson *et al.* 2003; Pagli *et al.* 2003; Árnadóttir *et al.* 2004; Jónsson 2008; Sudhaus & Jónsson 2008). LaFemina *et al.* (2005) used GPS campaign measurements between 1992 and 2003 to infer latitudinal variation in the spreading rates across the WVZ and the EVZ, the two main axes of spreading in south Iceland. From 2-D modelling of these GPS measurements LaFemina *et al.* (2005) suggested a rate decrease along the WVZ, from 7.0 mm yr^{-1} in the south to 2.6 mm yr^{-1} in the northern part of the zone, and an increase in rates along the EVZ from 11 mm yr^{-1} in the south to 19 mm yr^{-1} in the north. LaFemina *et al.* (2005) also concluded that the sum of the extension rates across the WVZ and the EVZ is 18–20 mm yr^{-1}, in the direction of plate motion (N102°E), which is consistent with plate motion model predictions (Sella *et al.* 2002). The crustal deformation due to relative plate motion in southwest Iceland has been estimated from GPS mea-surements between 1992 and 2004 by Árnadóttir *et al.* (2006). In this study, the 2000 pre-June GPS station velocities in SW Iceland were modelled assuming that the plate boundary can be approx-imated with several vertical dislocations. The study estimated a locking depth of ∼15 km and a deep slip rate of around 19 mm yr^{-1} for the SISZ.

The accommodation of E–W shear at depth in the SISZ by motion on a series of parallel N–S faults, causing counter-clockwise rotation of blocks, has been termed 'bookshelf faulting' (Einarsson *et al.* 1981; Sigmundsson *et al.* 1995). Sequences of earthquakes in the

SISZ have been documented in historical records, for example in 1732–1734, 1784 and 1896 (Einarsson *et al.* 1981; Stefánsson & Halldórsson 1988). During the 1896 sequence at least five events larger than magnitude 6 were reported over a distance of 50 km within two weeks. The largest instrumentally recorded earthquake was a $M_S = 7.0$ event which struck the eastern part of the SISZ in 1912 (Bjarnason *et al.* 1993a; Bellou *et al.* 2005). A new earthquake sequence in the SISZ was initiated on 2000 June 17 with a main shock of magnitude $M_w = 6.5$ in the east-central part, followed 81 hr later by another $M_w = 6.5$ event, located 17 km west of the June 17 main shock. The surface deformation caused by the June 17 and 21 main shocks was measured using both GPS and Interferometric Synthetic Aperture Radar (InSAR). Modelling of the geodetic data suggests up to 2.5 m of slip on two parallel 10 km long N–S faults (Árnadóttir *et al.* 2001; Pedersen *et al.* 2001, 2003). Three $M_w > 5$ events were triggered along the plate boundary on the Reykjanes Peninsula, up to 80 km from the June 17 main shock (Pagli *et al.* 2003; Vogfjörd 2003). One of these events caused a water level drop of several metres of Lake Kleifarvatn (Clifton *et al.* 2003). Triggering of the secondary events has been studied using the slip models derived from geodetic data to estimate the dynamic and static coseismic Coulomb stress changes (Árnadóttir *et al.* 2003, 2004; Antonioli *et al.* 2006). Observations of rapid post-seismic deformation have been explained by models of poro-elastic rebound (Jónsson *et al.* 2003). Although the static stress changes following the June 17 main shock promote failure on the June 21 fault these models do not explain the 81 hr delay between the two main events. Stress changes due to fluid flow following the first main shock may explain the time delay (Lindman 2009).

Here we study the surface deformation caused by the May 29 earthquake doublet. We consider these events a continuation of the sequence that started in the SISZ in 2000 June. The 2008 May 29 sequence initiated with a main shock beneath the Ingólfsfjall mountain (63.972°N, 21.072°W and ~5 km depth) at 15:45:58.9 UTC according to the SIL seismic catalogue (IMO). Almost immediately, aftershock activity started on a second fault (the Kross fault), located approximately 5 km west of the initial main shock. Increased earthquake activity was also observed along an E–W zone, with several $M_L 3$ events (Fig. 1). The teleseismic centroid-moment-tensor solutions indicate rupture on a near vertical fault, with right lateral motion on a N–S striking fault or left-lateral motion on an E–W oriented structure, with a seismic moment of $M_w 6.3$ (NEIC). Coseismic offsets were observed by the CGPS network in the area (Hreinsdóttir *et al.* 2009), and campaign style GPS measurements were started a few hours after the initial main shock (Decriem *et al.* 2008). The earthquake sequence was also observed by the ICEARRAY strong motion network (Halldórsson & Sigbjörnsson 2009).

Independent estimates of the coseismic offsets causing the 2008 May 29 earthquakes at CGPS stations in SW Iceland have been used to model the fault geometry and slip by Hreinsdóttir *et al.* (2009). Here we extend the work by Hreinsdóttir *et al.* (2009) by analysing campaign and continuous GPS data as well as radar interferograms (InSAR). The dense spatial sampling of InSAR data combined with the 3-D GPS displacements improve the constraints on the model parameters from the previous study. We invert the geodetic data to estimate dislocation source geometries and locations, and distribution of slip on the rupture surfaces using a layered half-space rheology to account for heterogeneities of the elastic parameters in the Icelandic crust. From our extensive geodetic data set we are able to resolve variations in the slip models on a 500 m gridded plane. The variation of the elastic parameters with depth does not greatly affect the fault geometry, but is important when estimating coseismic stress changes. Our Coulomb failure stress calculations indicate an agreement between areas of stress increase and locations of aftershocks.

2 DATA

2.1 GPS data and analysis

Annual campaign style GPS measurements have been conducted in the SISZ and on the Reykjanes Peninsula since 2000 June (Árnadóttir *et al.* 2006; Keiding *et al.* 2008). During the campaign measurements each site is normally occupied for at least one 24 hr session. We resurveyed 52 benchmarks in a GPS campaign between 2008 April 29 and May 19. Following the May 29 earthquakes, all benchmarks within a radius of ~100 km that we had previously occupied with GPS, were remeasured (Fig. 1). In addition, we deployed a semi-continuous GPS network where 21 benchmarks were occupied almost continuously until July 21 and 12 stations until mid-August.

In order to estimate the inter and coseismic deformation in SW Iceland we include in our analysis all available campaign and continuous GPS data from 2001 to 2008.

The GPS data analysis is performed in two steps. First, we calculate daily solutions using the Bernese v5.0 software (Dach *et al.* 2007) with orbit information and Earth rotation parameters from the International GPS Service (IGS) in the International Terrestrial Reference Frame (ITRF) 2005. For each 24 hr session we include the GPS campaign data, CGPS data from stations in Iceland, and data from nine long-running CGPS stations outside of Iceland (ALBH, ALGO, ALRT, BRUS, CAGL, DREJ, MADR, ONSA and WES2). The processing includes (1) cycle slip correction from phase single difference, (2) double-difference phase residuals screening and outlier rejection, (3) coordinates and troposphere estimates using the Quasi Ionosphere Free (QIF) strategy and (4) final coordinate estimation, zenith path delays and horizontal tropospheric gradient based on the L3 linear combination. In this last procedure the coordinates of the nine fiducial sites outside of Iceland are tightly constrained by means of a three parameter Helmert transformation (the three translation components should be zero and the residuals below 1 cm).

In the second step, we import SINEX files containing the Bernese daily solutions into the GLOBK software (Herring *et al.* 2006) to generate a solution using a regional stabilization approach (McClusky *et al.* 2000). We first combine our solutions with three IGS global network solutions (IGS1, IGS3, and EURA) using the global stations in the origin definition. We then identify the most stable fiducial sites as ALBH, ALGO, ALRT, MADR, ONSA, BRUS, CAGL and DREJ (misfit less than 1.23 mm in position and less than 0.5 mm yr^{-1} in velocity) and realize a reference frame approximately aligned with the ITRF2005. Finally, we estimate annual positions and velocities with respect to the reference frame (Fig. 2).

We calculate the coseismic station displacements in east, north, and vertical by combining the time-series from 2001 January 1 to 2008 May 28 with the solution from 2008 May 30 to June 10. Fig. 3 shows the time-series from CGPS stations in the epicentral area. The benchmarks HV08, VG13, VG15, VG20, VG22 and VG24 had only been measured once with GPS, in 2007 November by the Iceland GeoSurvey (ISOR). In order to calculate the coseismic displacements at these sites, we need to estimate the interseismic velocities in order to correct for the 6 months of plate motion between 2007
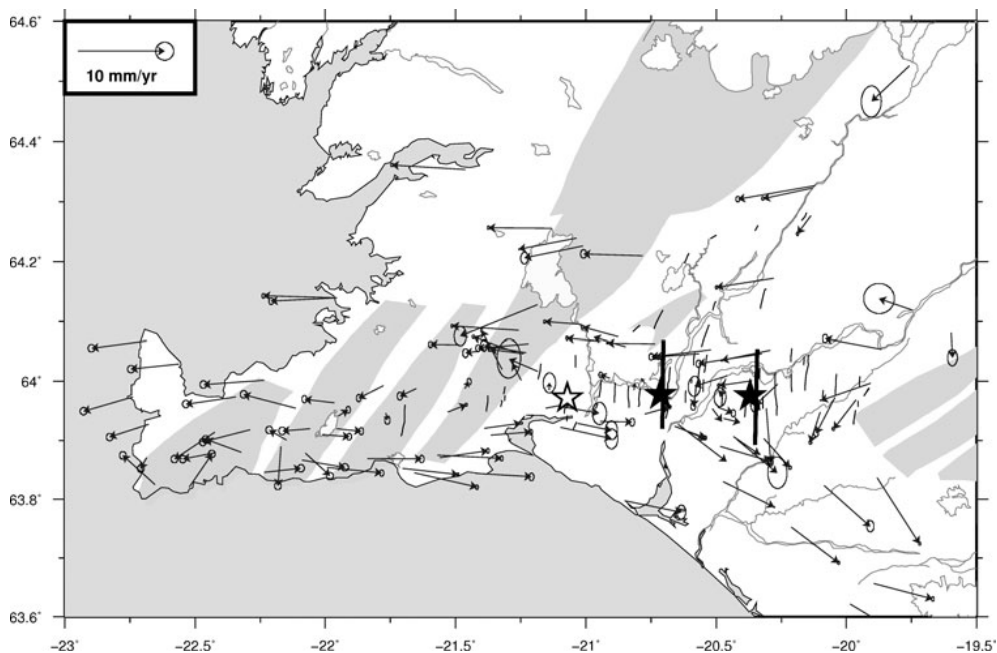
Figure 2. GPS station velocities (with 95 per cent confidence ellipses) in the SISZ and Reykjanes Peninsula calculated from campaign and continuous observations form 2001 January 1 to 2008 May 28. The velocities are the average between the solutions for stable North America and stable Eurasia, to depict motion relative to the plate boundary. The stars show the 2000 June main shocks (black) and the initial 2008 May 29 main shock (white). The black bold lines are the surface projections of the variable slip models for the 2000 June events (Pedersen *et al.* 2003).

Figure 3. Continuous GPS time-series at the closest stations to the Ingólfsfjall area corrected for plate motion and seasonal effects. The coseismic displacements are seen as offsets on the time-series on 2008 May 29 (indicated with a vertical dashed line).

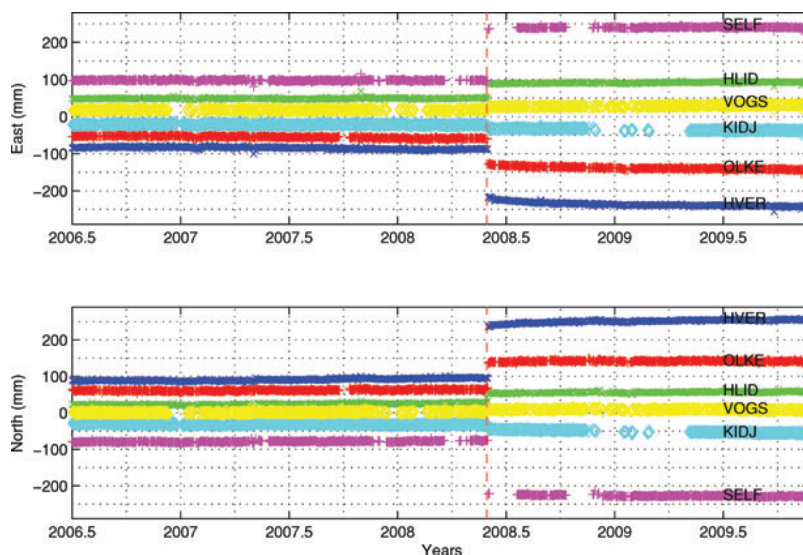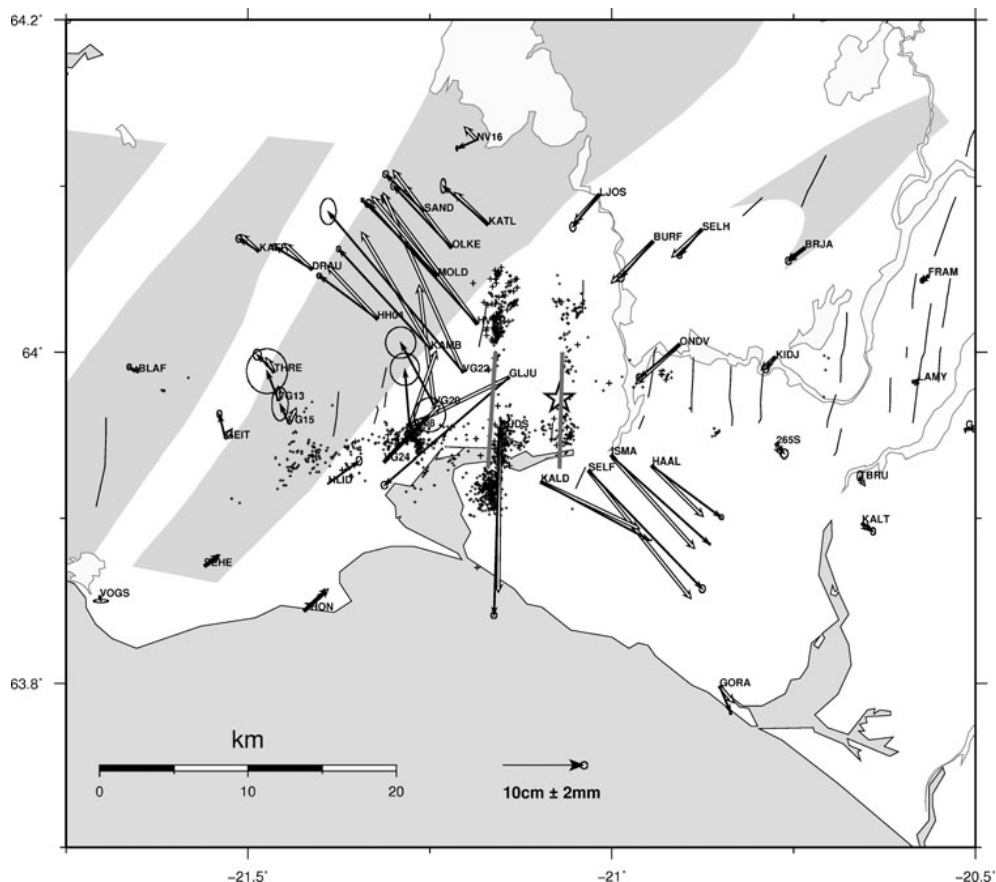**Figure 4.** Coseismic deformation in the Ölfus area following the 2008 May 29 earthquake sequence. The observed horizontal GPS displacements are shown with black arrows and 95 per cent confidence ellipses, whereas the white arrows are the predicted displacements for the preferred uniform slip model (thick grey lines). The white star indicates the epicentre of the first main shock and black crosses show locations of aftershocks recorded by the SIL seismic network from 2008 June 2 to July 10.

November and 2008 May. The interseismic deformation is evaluated by interpolating the velocities at the closest station (THRE, GEIT, HLID and HVER) using a Delaunay triangulation scheme. The coseismic deformation observed by GPS is shown in Fig. 4 and the numerical values are given in Table S1. The large uncertainties in the coseismic estimates for the ISOR stations are due to short observation sessions in 2007 (each station was only observed for 2–6 hr) and the uncertainties in estimating the interseismic deformation.

2.2 InSAR data analysis

Interferometric Synthetic Aperture Radar (InSAR) is a satellite based method that can be used to measure surface deformation. When two images have been acquired with approximately the same observation geometry, it is possible to get a measurement of the surface displacement by differencing the phases of two SAR images. The advantage of InSAR is the dense spatial coverage associated with remote sensing, but because of the observation geometry, the surface deformation is only sampled along one direction, that is, the line-of-sight (LOS) of the radar. Several radar images acquired

by ENVISAT and ALOS satellites span the time of the 2008 May earthquakes both along ascending and descending tracks (Table S2). The ASAR instrument onboard the ENVISAT satellite operates in C-band with a wavelength of 56.2 mm, whereas the PALSAR instrument onboard the ALOS satellite operates in L-band with a wavelength of 236.0 mm.

We use the Stanford Method for Persistent Scatterer (StaMPS) (Hooper *et al.* 2007) to generate interferogram time-series from 2007 to 2008 for three ENVISAT tracks, two descending (T138, T367) and one ascending (T402) in addition to an ascending ALOS track (T20). The mean LOS unit vector, $\hat{\mathbf{n}}$ = [East, North, Up], for each interferogram is: $\hat{\mathbf{n}}_{ALOS}$ = $[-0.62 \ -0.12 \ 0.77]$, $\hat{\mathbf{n}}_{T138}$ = $[0.33 \ -0.09 \ 0.93]$, $\hat{\mathbf{n}}_{T367}$ = $[0.36 \ -0.11 \ 0.92]$ and $\hat{\mathbf{n}}_{T402}$ = $[-0.35 \ -0.10 \ 0.92]$. We use the time-series analysis to isolate the best target pixels (those most coherent in time) as well as to estimate the spatially correlated look angle errors (i.e. not randomly distributed errors due to spatially correlated errors in the DEM) and master atmosphere/orbit errors. The unwrapped phase is calculated with a statistical cost flow algorithm as described in Hooper (2009). From this analysis we select four interferograms with
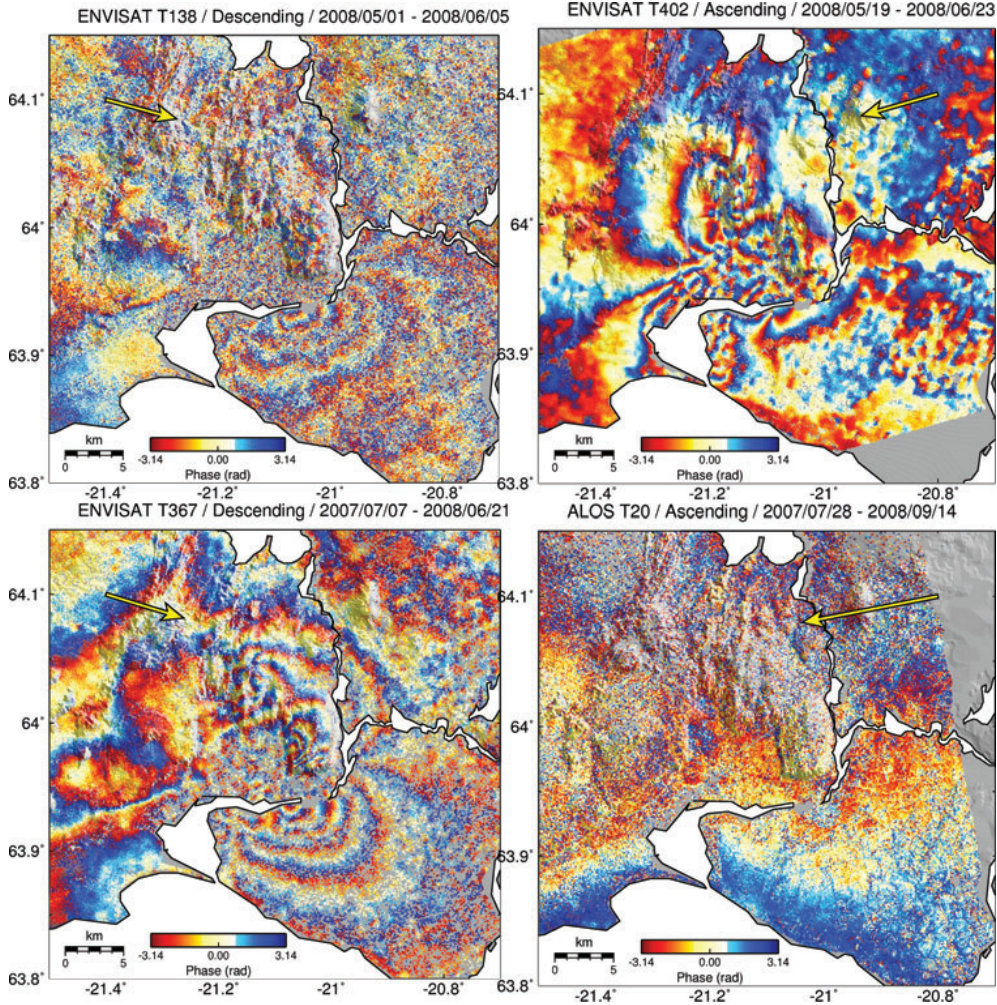
Figure 5. Wrapped phase interferograms spanning the 2008 May 29 earthquakes. Each colour cycle represents 28 mm of motion in the LOS between the ground and the ENVISAT satellite and 120 mm for the ALOS. The yellow arrows show the surface projection of the mean LOS unit vectors.

different sensors and observation geometries shown in Figs 5 and 6. The details of the available interfograms are given in Table S2.

2.2.1 Error estimates for the InSAR data

Several error sources affect the InSAR data, in the observation itself or due to the processing. The main sources of errors are electronic noise from the instrument, atmospheric disturbance along the radar wave paths, distribution of the scatterers for a given pixel, satellite orbit inaccuracies and digital elevation model (DEM) errors. The StaMPS method accounts for several error terms including uncorrelated noise, spatially correlated look angle errors (almost entirely due to DEM errors), and atmospheric and orbit errors due to the master image (Hooper *et al.* 2007). The remaining error terms in our data set mainly depend on the state of the atmosphere and ground surface conditions at acquisition time of the slave image. These

errors are spatially correlated due to the smooth variation of the atmospheric signal delays and are specific for each interferogram. As the data interpretation and modelling depend on the quality of the measurements, we need to quantify the remaining error in the InSAR data. We do this by statistically estimating the empirical covariance function of each interferogram, following (Sudhaus & Jónsson 2008). We assume that the error statistics are the same across the whole image. Therefore, we can estimate the covariance function, cov(h), where h is the pixel separation distance in the non-deforming part of the interferogram and assume the same power and structure for the deforming part.

To estimate the covariance we first form a discrete semi-variogram $\hat{\gamma}$ by sampling our data in the following manner:

$$\hat{\gamma}(h_c) = \frac{1}{2N} \sum_{i=1}^{N} [d(\mathbf{r}_i) - d(\mathbf{s}_i)]^2, \tag{1}$$
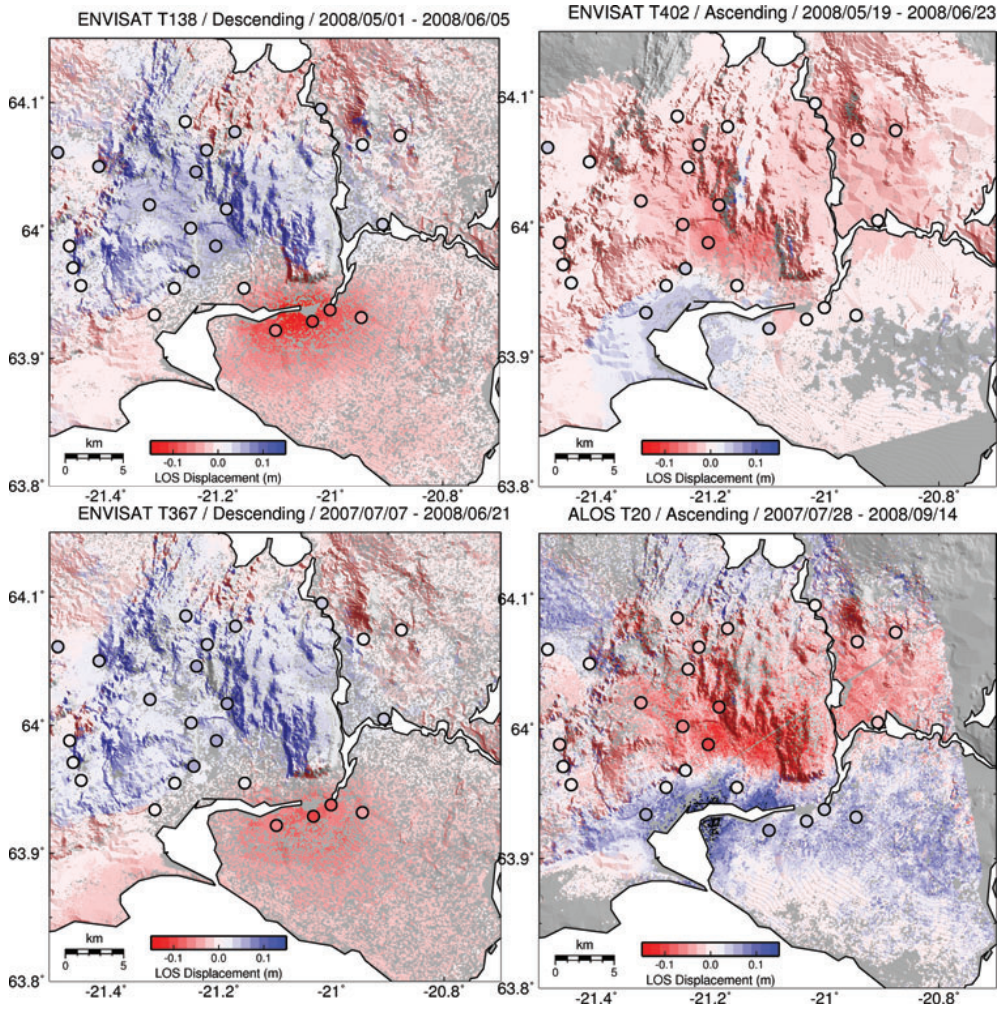
Figure 6. Unwrapped InSAR interferograms. The LOS displacements during the time interval given on each interferogram are shown by colour, where blue indicates an increase in the LOS (motion away from the satellite, primarily subsidence) and red represents a LOS decrease (motion towards the satellite). The coloured dots give the GPS station displacements projected onto the unit vector of the LOS for each interferogram.

where h_c is a bin of distances, $d(\mathbf{r}_i)$ and $d(\mathbf{s}_i)$ are the data values of the pixels located at $\mathbf{r}_i$ and $\mathbf{s}_i$, and N is the number of pixels satisfying the distance $\|\mathbf{r}_i - \mathbf{s}_i\| \simeq h_c$. We use a bin width of $h_c = 150$ m ranging from 0 km to the half of the maximum separation possible and randomly sample 500 000 pixel pairs in the non-deforming part of our images to build $\hat{\gamma}(h_c)$. We then fit the semi-variogram with an appropriate empirical function, $\gamma(h)$, given the shape of the variogram and the expected structure of the errors. Here, we assume that $\gamma(h)$ is an exponential decay function, $\gamma(h) = \sigma^2 \cdot \exp(\frac{-h}{a})$, where a is the correlation length and σ^2 are the data variance.

Finally, we obtain the empirical covariance function from

$$cov(h) = cov(0) - \gamma(h), \tag{2}$$

where $cov(0)$ is the non-correlated error of each measurement, referred to as the semi-variogram zero crossing. Using eq. (2) we

can calculate the full data covariance matrix for the interferograms given the separation distance between each pixel pair.

2.2.2 Sub-sampling of the InSAR datasets

Due to the extensive spatial coverage, the InSAR data sets consist of several hundred thousand points. We therefore need to resample our interferograms to a more manageable data set. We use an adaptive quadtree subsampling scheme similar to Jónsson *et al.* (2002) in order to reduce the number of data points without loosing the benefits of the high spatial resolution of the radar images. The quadtree algorithm recursively divides the image into squares until the variance of the pixels contained in each square does not exceed a given threshold. Therefore, an area with a high variance will be subdivided whereas an area with a low variance will be represented
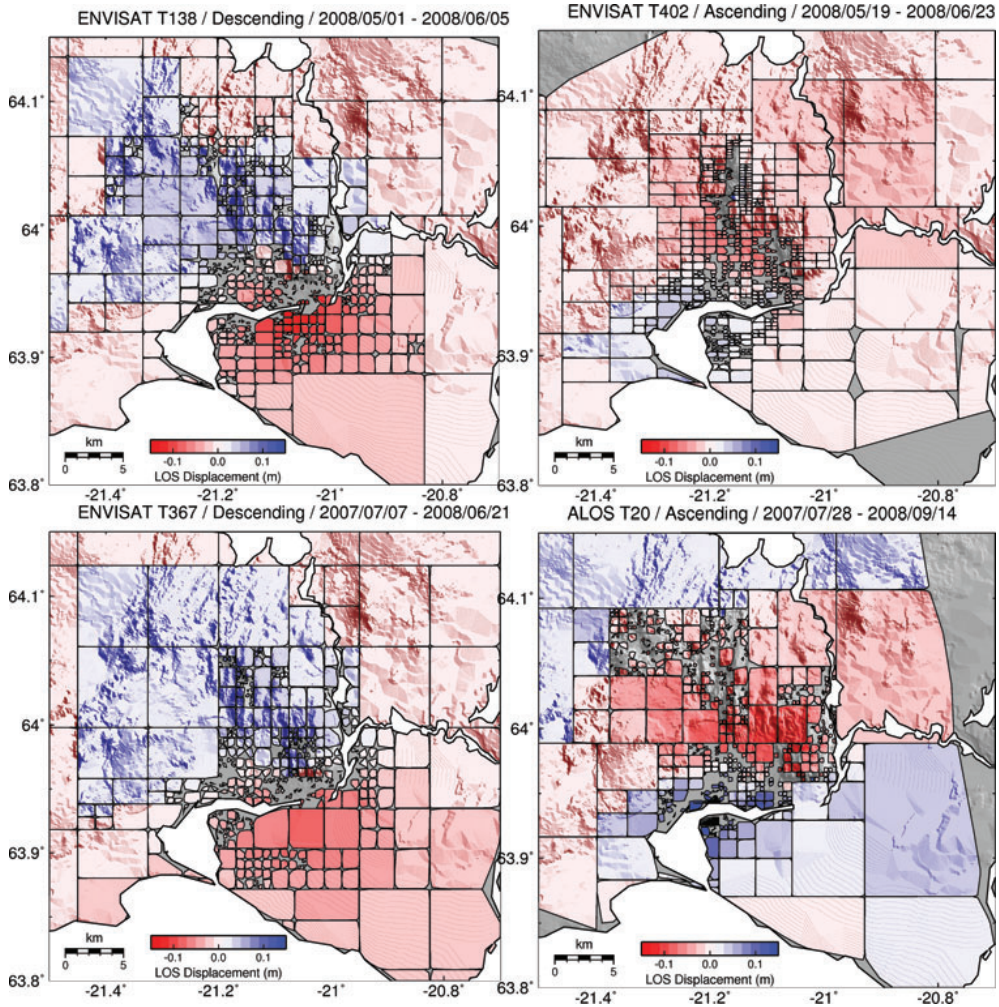
Figure 7. Quadtree subsampling of the LOS InSAR data.

by larger squares. The quadtree algorithm adapts the subsampling to both the variance of the measurements and the spatial coverage in case of data gaps. Since StaMPS works with a list of persistent scatterer (PS) pixels rather than an array of pixels we apply the quadtree algorithm to the geographic coordinates (latitude and longitude) rather than the radar coordinates (range and azimuth). We define our 'squares' (or polygons in this case) as the spatial envelope around a group of PS pixels and the mean of all the geographic coordinates as the focal point. This strategy implies that our polygons can be irregularly aligned, depending on the density of points in a particular area. As a benefit, we note that using this approach reduces slightly the number of subdivisions caused by data gaps, especially along the edges of the image. We set the threshold values for the quadtree algorithm to the variance values derived from the error estimation in Section 2.2.1, and retain only polygons containing more than five pixels. This leads to ∼500 representative data points for each InSAR image (Table S2). The resulting quadtree

images are shown in Fig. 7. Once the interferograms have been re-sampled we use eq. (2) to build the quadtree covariance matrix Σ according to the interpolygons distances.

2.3 Coseismic deformation

The coseismic surface deformation we estimate from the campaign and continuous GPS and InSAR observations is shown in Figs 4–6. Most of the surface deformation is concentrated within 10–15 km of the main area of aftershocks, and the amplitudes decay rapidly suggesting that most of the slip occurred above 10 km depth. The largest horizontal coseismic GPS station displacement was recorded at VG22 (258 ± 11 mm towards NW) while the closest CGPS stations (HVER and SELF) moved by 199 ± 4 mm and 201 ± 3 mm towards NW and SE, respectively. A maximum of 100 mm in the direction of LOS was recorded by the ALOS satellite. Smaller

displacements were recorded by ENVISAT, which can be explained by the different observation geometry as represented by the LOS unit vectors, where the ALOS satellite is more sensitive to horizontal motion than the ENVISAT.

In the descending interferograms (Fig. 6) we observe a range increase towards north and range decrease southward, which correspond to motion away from the satellite and motion towards the satellite, respectively. Due to the difference in the horizontal component of the LOS unit vectors, the pattern of deformation is reversed in the ascending interferograms. The magnitude of the LOS displacements obtained from the InSAR are consistent with the GPS measurements (Fig. 6).

There are two geodetic benchmarks on top of Kögunarhóll hill that have been observed previously with GPS. The hill is located less than 100 m south of the epicentral location of the Ingólfsfjall earthquake, along the trace of the fault. Two parallel branches of tectonic faulting have been identified here, one on each side of the benchmarks. We observed both sites on Kögunarhóll hill and found that the two points moved apart by 500 mm. The hill sustained significant local deformation and surface cracks were formed, most likely due to amplification of seismic waves radiating from the initial rupture. We therefore do not use GPS data from the Kögunarhóll stations in our modelling.

3 MODELLING

In this section, we explain how we model the coseismic surface deformation observed by campaign and continuous GPS and InSAR. A tomographic study of the epicentral area indicates a strong gradient in the seismic velocities, with the *P*-wave velocity varying from ∼4 to ∼6 km s^{-1} and the *S*-wave velocity increasing from ∼2.3 to ∼3.8 km s^{-1}, suggesting an increase in the shear modulus from 12 to 30 GPa in the uppermost 2 km (Tryggvason *et al.* 2002). Tryggvason *et al.* (2002) estimate that the thickness of the brittle part of the crust (i.e. the depth above which 90 per cent of the earthquakes occur) increases from about 5 km on the Reykjanes Peninsula to about 12 km in the eastern part of the SISZ.

In our modelling we account for the depth dependence of the elastic parameters in the crust by using a layered Earth rheology derived by Dubois *et al.* (2008), given in Table 1. We use the software PSCMP/PSGRN (Wang *et al.* 2006) to calculate the surface displacements and the stresses due to slip on rectangular dislocations in a layered half-space. The surface displacements are a non-linear function of the location and geometry of the source, whereas the slip has a linear dependence. We follow a conventional approach of first estimating the dislocation geometry and location assuming

Table 1. Elastic parameters.

Depth (km)	Density ρ (kg m^{-3})	Shear modulus μ (GPa)	Poisson's ratio ν
0.0	2306	12.2	0.28
0.6	2512	19	0.28
1.2	2630	25.6	0.28
1.8	2706	30	0.28
2.4	2753	34.3	0.28
3.0	2830	41.3	0.25
8.0	2959	45	0.25
13.0	3322	60	0.30

Notes: Layered earth model for South Iceland initially derived by Dubois *et al.* (2008) based on seismic tomography from Tryggvason *et al.* (2002). The depth is to the top of the layer.

constant slip using non-linear optimization. We then use a regularized linear inversion algorithm to solve for variable slip given the optimal dislocation location and geometry estimated in the first step.

3.1 Uniform slip models from non-linear optimization

Here we estimate the optimal fault locations and geometries, assuming that the faults can be represented as rectangular dislocations with constant slip. The surface displacements have a non-linear relation to the dislocation geometry and location. We use a probabilistic Bayesian approach based on the Metropolis-Hastings algorithm (Metropolis *et al.* 1953), to solve this non-linear problem. Given that each of our model parameter can be expressed by a proposal (or *a priori*) probability density function (PDF), we can use Bayes' theorem to update the proposal density based on the observed data and the resulting (posterior) PDF is the solution of the inverse problem.

Bayes' theorem states the posterior PDF, $p(\mathbf{m}|\mathbf{d})$, of the model parameters $\mathbf{m}$ given the data $\mathbf{d}$ as

$$p(\mathbf{m}|\mathbf{d}) = \frac{p(\mathbf{d}|\mathbf{m})p(\mathbf{m})}{p(\mathbf{d})} \tag{3}$$

with $p(\mathbf{m})$ the probability of the model parameters and $p(\mathbf{d})$ the probability of the data. The major advantages of the Bayesian approach is that the posterior PDF contains uncertainties as well as interparameter correlations, where other methods only allow us to resolve for one single set of optimal model parameters. In the case of non-linear inversion problems the posterior PDF is difficult to derive analytically, but it can be numerically estimated using a Markov chain Monte Carlo (MCMC) algorithm. We use the Metropolis–Hastings algorithm since it can draw samples from any probability distribution $p(\mathbf{x})$, requiring only that the density can be calculated at $\mathbf{x}$. A popular adaptation of the Metropolis–Hastings algorithm is the Simulated Annealing algorithm which is designed to move faster to the minimum energy state without drawing the complete posterior PDF.

We first need to express the posterior PDF. We assume *a priori* that the PDF's for the model parameters, $p(\mathbf{m})$, are boxcar functions (i.e. one for a given interval and zero elsewhere), and that the observation errors have a Gaussian distribution with a mean of zero. We use the Bayesian inversion formulation derived by Fukuda & Johnson (2008) for the case of multiple data sets with unknown relative weights. The relative weight terms are used to adjust the relative weights of the GPS and InSAR data sets. In our case these estimated terms were close to one indicating appropriate error estimates for the different data sets. Assuming independent errors, the likelihood function we minimize is the product of the likelihoods for each independent data set

$$p\left(\mathbf{d}_1, \mathbf{d}_2, \ldots, \mathbf{d}_K | \mathbf{m}, \sigma_1^2, \sigma_2^2, \ldots, \sigma_K^2\right)$$
$$= \prod_{k=1}^{K} \left\{ \left(2\pi\sigma_k^2\right)^{-N_k/2} |\Sigma_k|^{-1/2} \right.$$
$$\left. \times \exp\left[-\frac{1}{2\sigma_k^2}(\mathbf{d}_k - \hat{\mathbf{d}}_k)^T \Sigma_k^{-1}(\mathbf{d}_k - \hat{\mathbf{d}}_k)\right]\right\}, \tag{4}$$

where $\mathbf{d}_k$ are the N_k data of the kth data set, $\mathbf{m}$ the model parameters and $\hat{\mathbf{d}}_k$ the corresponding predicted data, σ_k^2 is an unknown scale factor for the data errors Σ_k of the kth data set. Reintroducing the likelihood function into Bayes' theorem we get the posterior

Table 2. Uniform slip models.

	Length (km)	Width (km)	Depth (km)	Strike (deg)	Longitude (deg W)	Latitude (deg N)	Strike-slip (m)	χ_ν^2
Kross								
GPS	$6.3^{+1.0}_{-1.5}$	$4.9^{+0.8}_{-3.0}$	$0.3^{+0.2}_{-0.3}$	$3.5^{+0.7}_{-1.9}$	$21.169^{+0.006}_{-0.008}$	$63.951^{+0.008}_{-0.006}$	$1.22^{+0.8}_{-0.4}$	4.6
InSAR	$7.4^{+1.9}_{-2.5}$	$3.3^{+1.2}_{-1.9}$	$0.9^{+0.3}_{-0.6}$	$2.5^{+0.3}_{-1.1}$	$21.175^{+0.002}_{-0.002}$	$63.951^{+0.005}_{-0.003}$	$0.94^{+0.2}_{-0.1}$	6.9
Joint	$8.0^{+1.4}_{-1.2}$	$5.0^{+5.3}_{-2.9}$	$0.3^{+0.1}_{-0.1}$	$2.8^{+1.2}_{-1.5}$	$21.172^{+0.008}_{-0.004}$	$63.961^{+0.003}_{-0.002}$	$0.75^{+0.03}_{-0.01}$	3.5
CGPS	$8.5^{+1.5}_{-3.1}$	$6.5^{+3.4}_{-1.4}$	$0.6^{+2.0}_{-0.6}$	$0.5^{+2.5}_{-0.5}$	$21.155^{+0.009}_{-0.003}$	$63.982^{+0.023}_{-0.015}$	$0.55^{+0.41}_{-0.20}$	3.0
Ingólfsfjall								
GPS	$10.1^{+1.0}_{-1.0}$	$3.9^{+0.5}_{-3.0}$	$2.2^{+0.5}_{-0.5}$	$0.6^{+0.2}_{-0.5}$	$21.075^{+0.009}_{-0.021}$	$63.987^{+0.004}_{-0.012}$	$1.25^{+2.8}_{-0.27}$	4.6
InSAR	$7.8^{+1.4}_{-1.5}$	$5.5^{+1.0}_{-2.1}$	$1.3^{+0.5}_{-0.8}$	$1.1^{+1.3}_{-0.4}$	$21.071^{+0.007}_{-0.018}$	$63.958^{+0.003}_{-0.009}$	$1.8^{+2.1}_{-0.6}$	6.9
Joint	$7.4^{+1.8}_{-1.3}$	$2.0^{+2.2}_{-1.4}$	$1.4^{+0.6}_{-0.6}$	$2.0^{+1.0}_{-1.5}$	$21.070^{+0.002}_{-0.001}$	$63.967^{+0.005}_{-0.004}$	$1.25^{+1.6}_{-0.34}$	3.5
CGPS	$10.1^{+2.1}_{-5.1}$	$5.4^{+4.3}_{-0.4}$	$0.5^{+3.1}_{-0.5}$	$0.0^{+1.7}_{-0.5}$	$21.073^{+0.002}_{-0.011}$	$63.980^{+0.017}_{-0.026}$	$0.79^{+0.2}_{-0.34}$	3.0

Notes: Optimal dislocation model parameters and 1σ confidence intervals assuming two dislocations. The length is measured along strike, and width is the downdip dimension. The depth is measured vertically from the surface down to upper edge of the dislocation. The dip is fixed to $90°$ (vertical dislocation). The longitude and latitude are the coordinates of the vertical surface projection of the dislocation centre point. The slip is right-lateral strike-slip in metres. The model parameters are given for the three cases considered in this study, that is, using only GPS data, only InSAR data, and from a joint inversion of InSAR and GPS data, as well as those estimated from continuous GPS data by Hreinsdóttir *et al.* (2009) (rows labelled 'CGPS'). The uncertainties estimated on the CGPS models obtained in a different manner than in this study, they are 95 per cent bounds from bootstrap calculations.

PDF

$$p\left(m, \sigma_1^2, \sigma_2^2, \ldots, \sigma_K^2 | \mathbf{d}_1, \mathbf{d}_2, \ldots, \mathbf{d}_K\right)$$

$$= \prod_{k=1}^{K} \left(\sigma_k^2\right)^{-N_k/2} \exp\left[-\frac{1}{2}\sum_{k=1}^{K}\frac{1}{\sigma_k^2}(\mathbf{d}_k - \hat{\mathbf{d}}_k)^T \Sigma_k^{-1}(\mathbf{d}_k - \hat{\mathbf{d}}_k)\right].$$

(5)

Since we can calculate the posterior PDF from eq. (5) for a given set of model parameters **m**, we can estimate the full PDF with the Metropolis algorithm. The Metropolis algorithm samples the model space using random walk as follows: A candidate model, **m**′, is generated from the previous step, $\mathbf{m}^{(t)}$, as $\mathbf{m}^{(t)} + \delta(\mathbf{m}_i)$ with $\delta(\mathbf{m}_i)$, a random step according to $p(\mathbf{m})$. **m**′ is accepted as the new state of the Markov chain only if it satisfies the Metropolis criterion

$$min\left(1, \frac{p(\mathbf{m}')}{p(\mathbf{m}^{(t)})}\right) > u \sim U(0, 1)$$

(6)

with u a random number from a uniform distribution over the interval [0, 1]. If the candidate model does not satisfy the Metropolis criterion then the Markov chain remains at the current state, $\mathbf{m}^{(t)}$. After a sufficiently large number of steps, during which the Markov chain converges (also called a 'burn-in' stage) the samples of the

Markov chain can be considered as a set of samples drawn from the posterior PDF.

The aftershock locations suggest that more than one fault ruptured in the May 29 sequence. We therefore investigated several different models, increasing the number of dislocations to mimic the aftershock zones. Our analyses indicate that the geodetic data do not require significant slip on more than two main segments, as concluded by Hreinsdóttir *et al.* (2009).

As the data sets span different time intervals, we estimate the optimal model parameters assuming two dislocation surfaces, first using only the GPS data, then the InSAR data, and finally in a joint inversion using all the data. We select the best model as the maximum likelihood solution (i.e. the solution with the highest probability density). The model parameters are summarized in Table 2 and the posterior PDF's for the parameters are shown in Fig. 8. We found some differences in the estimated model parameters for the three cases. In general, the solutions that include the InSAR data have a narrower range of possible model parameters for the Kross fault, which indicates that the InSAR data provide important constraints on the deformation in the area around the Kross fault. The GPS based inversion suggest that the Ingólfsfjall fault plane extend close to the surface whereas the InSAR data suggest that slip occurred
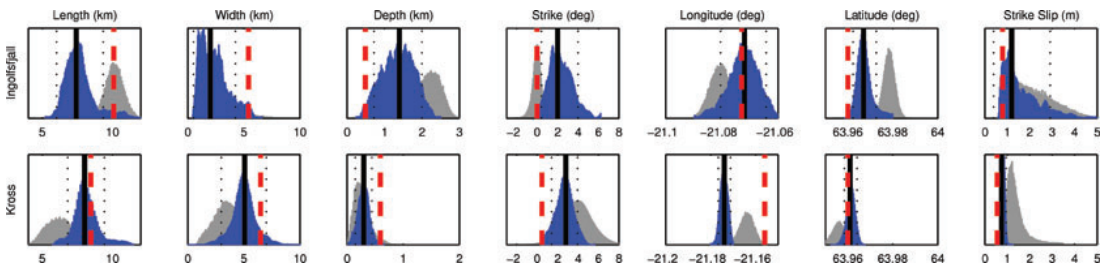

Figure 8. Posterior probability distributions of the uniform slip model parameters using GPS data only (grey) or the joint inversion of GPS and InSAR data (blue). The black lines show the best-fitting model values for the joint inversion, and the dotted lines indicate the 1σ confidence interval. The red dashed lines show the optimal model values estimated by Hreinsdóttir *et al.* (2009) using only the CGPS data.

below 2 km depth. Our interpretation is that there is not sufficient near field data to resolve the shallow part of the Ingólfsfjall fault.

To assess how well the models fit the data we calculate the weighted residual sum of squares, $WRSS = \mathbf{r}^T \Sigma^{-1} \mathbf{r}$, where $\mathbf{r}$ is the difference between the observed data and model prediction (i.e. the data residual vector) and Σ^{-1} is the inverse of the data covariance matrix. We report the goodness of fit to the data using $\chi^2_\nu = WRSS/(N - m)$, where N is the number of data and m is the number of model parameters that we estimate. For the uniform slip models $N = 2176$ and $m = 18$. Our preferred model is based on the joint inversion of GPS and InSAR data. This model has a lower misfit ($\chi^2_\nu = 3.5$) than we find for the optimal models from inversion of only the GPS data ($\chi^2_\nu = 4.6$) or the InSAR data ($\chi^2_\nu = 6.9$). We suspect that some of the differences in the optimal models are due to inadequate corrections for interseismic signals or rapid post-seismic deformation. However, we argue that these signals are small compared to the coseismic displacements and hence we prefer the model from the joint inversion, as this takes full advantage of the dense spatial coverage of InSAR as well as the 3-D displacement field from the GPS observations. Our best-fitting uniform slip model (from the maximum likelihood estimate) for the Ingólfsfjall fault has 1.2 m of right-lateral strike-slip on an 7.5 km long fault extending from 2 to 4 km. This suggests that most of the slip is concentrated below 2 km. For the Kross fault we estimate a 8 km long fault surface extending from 0.5 to about 5 km depth with 0.75 m of right-lateral strike-slip.

We examine the linear relationship between the model parameters in our study by plotting the correlation matrix (Fig. 9). The absolute value of the correlation coefficient gives a measure of the linear relationship between the model parameters, where a large value (i.e. an absolute value close to one) indicates a strong trade-off between the parameters and a coefficient of 0 indicates that the variables are independent. A negative correlation coefficient suggests an anti-correlation, whereas a positive coefficient represent a positive correlation. As the model parameters have a non-linear relationship to the surface deformation any significant correlation between the resulting model parameters indicates a trade-off that we are not able to resolve with our data set. With a perfect data set (i.e. with adequate spatial sampling and small data errors) one should find all the PDF's to be independent (i.e. all the correlation coefficients are zero). We found a strong correlation (0.87) between the north coordinate and length of the Ingólfsfjall fault, showing that the northern end of the fault is not well constraint. This can be explained by a general decrease of the coherence of the InSAR data on the Ingólfsfjall mountain and the closest GPS benchmark (BURF) is located about 5 km north of the mountain. We also note possible significant anticorrelation between the depth, downdip width, and amount of strike-slip motion, indicating that it is difficult to distinguish between a shallow source with high slip or a wide source with low slip, given our data set. The Kross fault is better resolved, with no correlation coefficient over 0.6. The rather small absolute values of the correlation between the parameters of the two dislocations
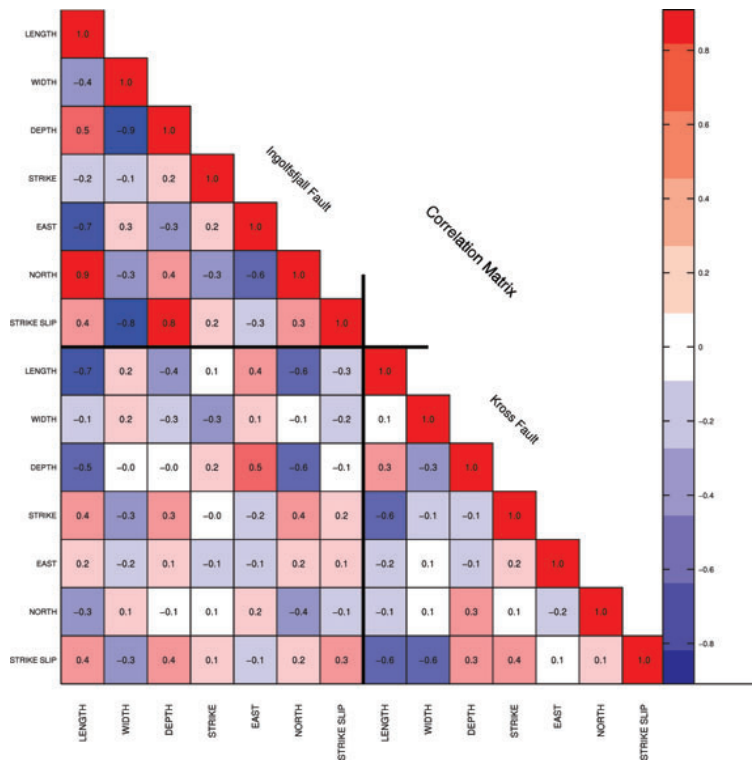

Figure 9. Correlation matrix of the marginal probability distribution of the uniform slip model parameters for the joint inversion. A value of 1 indicates perfect correlation and −1 is perfect anticorrelation.

(maximum value is 0.5) do not indicate substantial trade-off. In particular, the small value for the longitude (E–W location) of the two faults is rather remarkable given the proximity of the ruptures.

3.2 Non-uniform slip models

We estimate the slip distribution on each dislocation using the geometry and locations of our preferred uniform slip models obtained in the previous section. We increase the area of the uniform slip dislocations, so that they extend from the surface to 22 km depth and the length along strike is 25 km. Each rectangular dislocation source is then divided into square patches (0.5×0.5 km). In general, the surface displacements are a linear function of the slip. We minimize the weighted misfit (WRSS) between the observed and predicted surface deformation in a least-square sense and assume right-lateral strike-slip only. To regularize the problem, we impose a Laplacian smoothing operator (finite difference L) weighted by a smoothing parameter, κ. Our inversion problem can thus be described as

$$
\begin{bmatrix}
\mathbf{d}_{gps} \\
\mathbf{d}_{T138} \\
\mathbf{d}_{T367} \\
\mathbf{d}_{T402} \\
\mathbf{d}_{T20} \\
0
\end{bmatrix}
=
\begin{bmatrix}
G^K_{gps} & G^I_{gps} & 0 & 0 & 0 & 0 \\
G^K_{T138} & G^I_{T138} & 1 & 0 & 0 & 0 \\
G^K_{T367} & G^I_{T367} & 0 & 1 & 0 & 0 \\
G^K_{T402} & G^I_{T402} & 0 & 0 & 1 & 0 \\
G^K_{T20} & G^I_{T20} & 0 & 0 & 0 & 1 \\
\kappa L^K & \kappa L^I & 0 & 0 & 0 & 0
\end{bmatrix}
\times
\begin{bmatrix}
S^K \\
S^I \\
a_{T138} \\
a_{T367} \\
a_{T402} \\
a_{T20}
\end{bmatrix},
\quad (7)
$$

where $\mathbf{d}_{gps}$, $\mathbf{d}_{T138}$, $\mathbf{d}_{T367}$, $\mathbf{d}_{T402}$ and $\mathbf{d}_{T20}$ are the data vectors, G is a matrix that contains Green's functions for the patches on the two dislocation surfaces representing the Kross and the Ingólfsfjall fault, labelled by the superscripts K and I, respectively, S is a vector with the amount of strike-slip on each patch, and a is an arbitrary plane that is estimated to account for possible orbital errors in each interferogram, as noted by the subscripts. The equation system is solved using a fast non-negative least square solver (Lawson & Hanson 1974).

The parameter κ controls how well the model fits the data versus the roughness of the solution. A model with smoothly varying slip will not fit the data as well as a model that has many localized slip patches but a model with large differences in slip between adjacent patches (i.e. rough slip distribution) is considered physically unrealistic. The usual approach to determine an appropriate smoothing parameter (κ) is from a trade-off curve, where one tries to select a value that minimizes both the data misfit and the roughness of the slip model. A more robust approach (Matthews & Segall 1993) is to select κ using cross-validation sum of squares (CVSS). The CVSS is calculated as the sum of the weighted residuals for a given value of κ, in the following manner. An inversion is first performed on a data set omitting one data and the resulting model is then used to calculate the predicted data, for the data that was not included in the inversion. The difference between the data and the model prediction weighted by the data error is the weighted residual. This procedure is repeated for each datapoint and a range of κ and the minimum CVSS indicates the optimal smoothing value, given the data. We select a smoothing value of $\kappa = 0.8$ which is optimal from both the trade-off curve and the CVSS calculation (Fig. 10).

We calculate the resolution kernel of the inverse problem for the different data sets define by Tarantola (2005) as

$$
R = G^T (GG^T)^{-1} G. \quad (8)
$$

The resolution (dimensionless) is 1 in the well-resolved areas and 0 in unresolved areas. A plot of the resolution kernel (Fig. S1) shows that we can resolve the slip distribution down to ~8 km on the two fault planes for a joint inversion of GPS and InSAR data. The resolution is smoothly decreasing with depth indicating that we should no get any artefacts in the slip distribution due to the geometry of our observation network.

The estimated slip distributions are shown in Fig. 11 and the data residuals in Fig. 12. Most of the slip on the Kross fault is focused in an area that is approximately 5 km long and extends from 3 to 6 km depth with a maximum motion of 1.4 m. A second, smaller slip maximum is located further north, above a cluster of aftershocks. The slip model we obtain for the Ingólfsfjall event suggests smaller area of slip but a larger slip amplitude than on the Kross fault. The slip is concentrated in a 4×2 km area centred at approximately 3 km depth, and decreases smoothly from a maximum of 1.9 m to less than 0.5 m over a distance of 8 km towards north.

The geodetic moment release of our model for the Kross fault is $M_0 = \mu As = 8.65 \times 10^{17}$ Nm, where A is the fault area, s is the
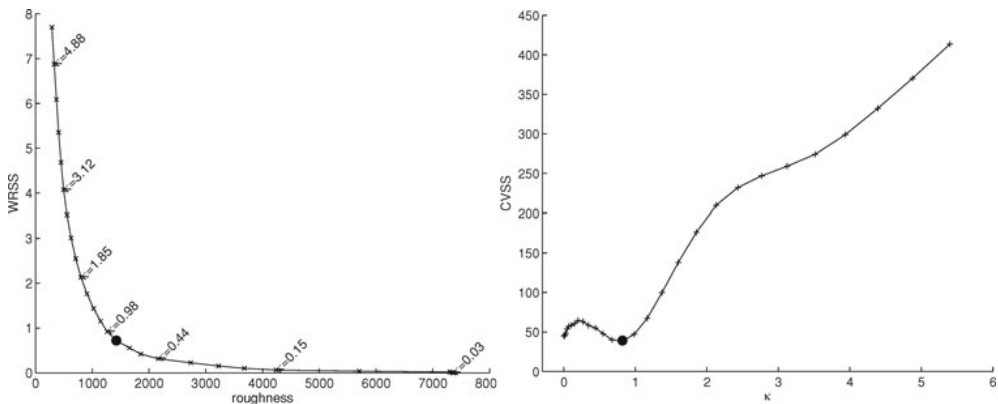

Figure 10. Evaluation of the optimal smoothing parameter (κ). Left-hand plot shows the trade-off curve between the weighted residual sum of squares (WRSS) and the model roughness, given the values of κ (text overlay). Right-hand plot shows the cross validation sum of squares (CVSS) versus κ. The dot indicates the preferred value of $\kappa = 0.8$ on both graphs.
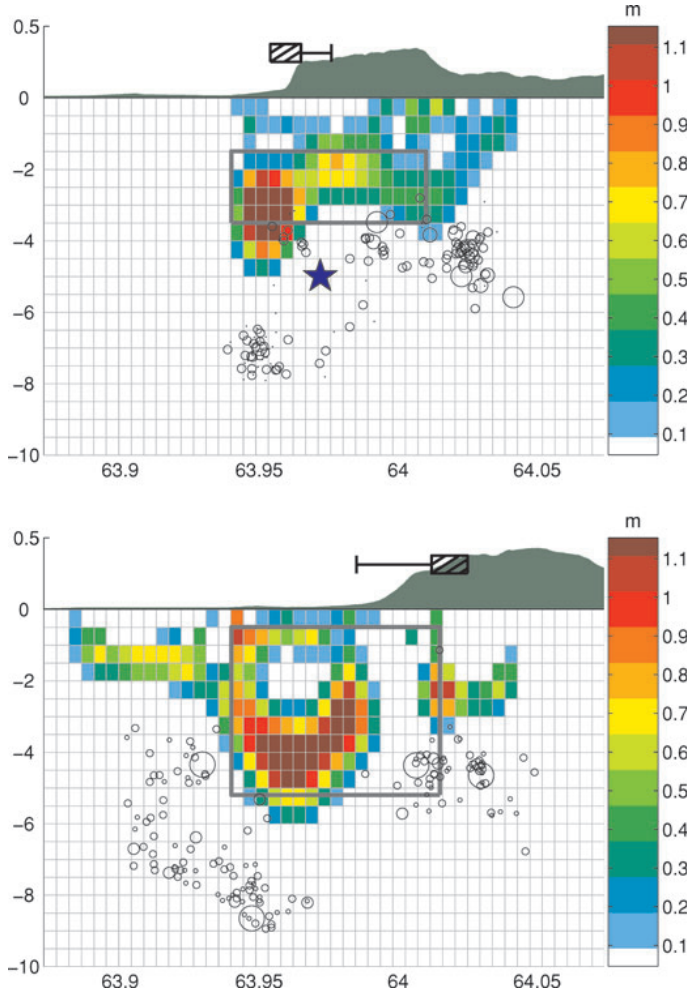
Figure 11. Variable slip model for the Ingólfsfjall fault (top panel) and the Kross fault (bottom panel). The amount of right-lateral strike-slip is shown with the colour scale (same for both figures). The black circles denote aftershocks recorded by the SIL network between 2008 June 2 and July 10. The locations of the constant slip models are shown with a grey outline. The black boxes indicate locations of mapped surface fractures, and the black lines show areas where the mapped fractures may be secondary features, rather than surface expressions of the 2008 May events.

slip, and μ is given Table 1. This geodetic moment corresponds to a seismic moment magnitude of $M_w5.9$, using $M_w = 2/3 \log_{10} M_0 - 6.03$. For the Ingólfsfjall fault we estimate a geodetic moment of 5.97×10^{17} Nm, corresponding to a moment magnitude of $M_w5.8$. Our models therefore give a cumulative geodetic moment for the doublet of $M_0 = 1.46 \times 10^{18}$ Nm, equivalent to a single event with a moment magnitude of $M_w6.1$.

3.3 Coseismic static Coulomb failure stress change

We calculate the static Coulomb stress changes predicted by our variable slip models using the layered Earth rheology, to examine possible stress triggering of the second event and how stress changes predicted from our model agree with aftershock locations.

The change in the static Coulomb failure stress change (ΔCFS) is estimated from (e.g. Harris 1998)

$$\Delta CFS = \Delta \tau_s + \mu_f \left(\Delta \sigma_n - \frac{B}{3} \Delta \sigma_{kk} \right), \tag{9}$$

where $\Delta \tau_s$ is the change in shear stress resolved in the slip direction of a fault that may fail in a subsequent event, $\Delta \sigma_n$ is the change in normal stress on the receiver faults, and $\Delta \sigma_{kk}$ is the change in volumetric stress. Here, μ_f is the coefficient of friction (we assume $\mu_f = 0.75$) and B is Skempton's coefficient ($B = 0.5$). The stress change depends on the location and orientation of the receiver faults. Here, the ΔCFS is calculated on N–S right-lateral strike-slip faults at 5 km depth. A positive ΔCFS implies an increase in the Coulomb failure stress, that may promote failure on secondary faults. Our
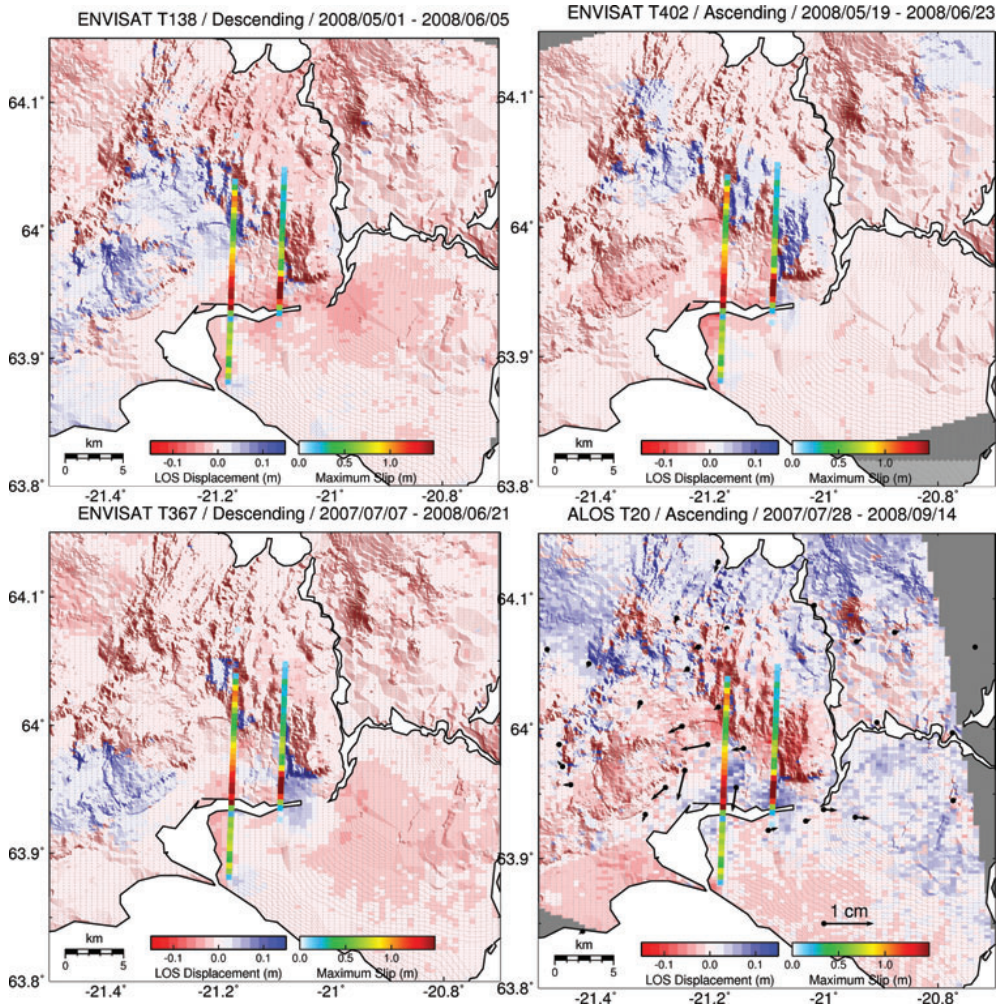
Figure 12. InSAR residuals from the non-uniform slip model are shown with the colour scale and the GPS residuals with arrows. The slip models are indicated by a bold line showing the maximum slip value at depth.

models predict positive static Coulomb stress changes following the Ingólfsfjall event at the location of the maximum slip on the Kross fault model (Fig. 13a). This suggests that the coseismic stress changes caused by the Ingólfsfjall event promoted failure on the Kross fault. Analysis of high-rate (1 Hz) CGPS data indicate that slip on the second fault initiated within 3 s of the initial main shock (Hreinsdóttir *et al.* 2009). Therefore, we cannot preclude dynamic stress triggering of the second event from the geodetic data. The positive Coulomb stress changes associated with the two main events correlate spatially with aftershock locations recorded by the SIL seismic network after the main shocks (Fig. 13b). Furthermore, our models indicate an increase in the Coulomb failure stress in the area west of the Kross fault and east of the Ingólfsfjall fault. Very few aftershocks were located on the Ingólfsfjall fault, while intense activity has continued on the southern part of the Kross fault.

4 DISCUSSION

4.1 Fault models

Our modelling shows that the coseismic deformation observed by GPS and InSAR can be explained by right-lateral motion on two parallel N–S striking faults, spaced about 5 km apart, in agreement with a previous study using only CGPS data (Hreinsdóttir *et al.* 2009). We find that the Kross fault is located slightly further west than in the models by Hreinsdóttir *et al.* (2009), based on data from two GPS stations located near the trace of the Kross fault (AUDS and GLJU), as well as pixels in the descending InSAR image located in the area between the two faults. We also note that the Ingólfsfjall rupture determined from the geodetic data lies to the west of where most of the aftershocks are located (e.g. Fig. 4), in agreement with
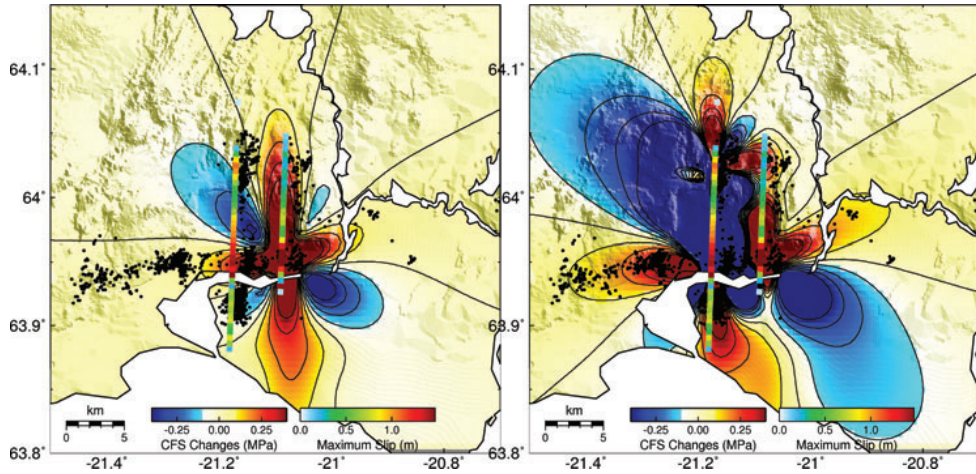
Figure 13. Static Coulomb failure stress changes for N–S right-lateral strike-slip faults at 5 km depth. The contours are 0.1 MPa. The left-hand panel shows the ΔCFS calculated from the variable slip model for the Ingólfsfjall event and the right-hand panel is the total ΔCFS predicted from the Ingólfsfjall and Kross models. The thick lines represent the surface projections of the dislocation models, where the colour indicates the maximum slip at depth. The black dots show the locations of aftershock recorded by the SIL network from 2008 June 2 to July 10.

field observations of surface ruptures in the epicentral area. Preliminary results from a local seismic network deployed after the May 29 earthquakes indicate that the aftershock locations from the SIL network may be ∼500 m too far east, due to variations in the seismic structure in the area that is not included in the SIL seismic model (B. Brandsdóttir 2009, personal communication).

Our best-fitting uniform slip model for the Ingólfsfjall fault suggests that most of the slip there occurred below 2 km which is deeper than the uniform slip model estimated by Hreinsdóttir et al. (2009). In general, we find higher slip over smaller fault surfaces, than Hreinsdóttir et al. (2009). Our variable slip models can explain 95 per cent of the data variance. The geodetic models suggest that the slip on the Kross fault was concentrated in two main patches, similar to the features found in the slip models estimated from CGPS data by Hreinsdóttir et al. (2009). Our study shows that most of the slip occurred north of the Ölfusá river, which is consistent with locations of surface fractures (Fig. 11). The variable slip model we obtain for the Ingólfsfjall event has less slip than on the Kross fault. The main patch in our model is located further south than in the CGPS model by Hreinsdóttir et al. (2009). The reason for this is most likely that there are only two continuous GPS stations located near the southern end of the Ingólfsfjall fault, whereas our data set includes several additional campaign GPS and InSAR data in the near-field area (Fig. 4). In particular, the GPS campaign stations LJOS, BURF, SELH and ONDV located 5–8 km from the northern part of the Ingólfsfjall fault show smaller coseismic displacements than the CGPS station SELF (in Selfoss), indicating that there was less slip on the northern part of the fault than on the southern part. The decrease of coseismic displacement eastward from the southern end of the Ingólfsfjall fault (i.e. at SELF, ISMA, HAAL) also indicates that most of the slip occurred at shallow depth on the southern part. The main slip on the Kross fault is roughly at the same location in both geodetic studies, confirming that the differences between the slip on the Ingólfsfjall fault estimated by Hreinsdóttir et al. (2009) and in this study are primarily due to an increase in the model

resolution when including the GPS campaign data and the InSAR images.

We also performed a joint inversion of the GPS and InSAR data assuming a half-space rheology (with $\nu = 0.28$). From a comparison between this and our optimal model, we conclude that the layered earth model produces lower slip magnitudes (0.25–0.5 m) and shallower slip (1–2 km) than the half-space model. Dubois et al. (2008), however, found more slip at depth when using a layered earth model to estimate the variable slip for the 2000 June events. In general, the slip models depend on the available data (which affects the model resolution), the earth model, the choice of the smoothing imposed on the model and the depth of the slip source.

The geodetic moments estimated from the variable slip models indicate that the initial event on the Ingólfsfjall fault was slightly smaller than the triggered rupture on the Kross fault. The magnitude and geodetic moment estimates using the depth dependent rigidity are, however, very similar to the half-space models (the difference in M_w is less than 0.02). Using a layered earth model rather than an elastic half-space thus affects the slip magnitude and depth in the variable slip model, but is unlikely to cause a shift in the latitude of the slip estimates. We note that aftershocks appear to cluster adjacent to the regions of coseismic slip on both faults (Fig. 11). In general, aftershocks are expected to occur in areas of large stress changes on and off the ends of the fault surface, as reported in many studies (e.g. Massonnet & Feigl 1993; Cohee & Beroza 1994; Pedersen et al. 2003; Johanson et al. 2006). The events in the 2008 May sequence are smaller than the 2000 June, which ruptured 10–15 km long faults with up to 2–3 m of slip, located above 10 km depth (Pedersen et al. 2003). The decrease in earthquake size is consistent with thinning of the brittle part of the crust from about 12 km in the east to ∼5 km in the west (e.g. Tryggvason et al. 2002; Árnadóttir et al. 2006). As for the 2000 June main shocks, we find a high ratio of slip to fault length indicating high stress drop in these earthquakes. This has also been noted for earlier events in the

Table 3. Earthquakes in the SISZ.

Date	Lat.	Lon.	Magnitude	District/location
1630/02/21	64.00	20.21	7	Land, Minnivellir
1633/–/–	–	–	–	Ölfus
1706/04/20	63.90	21.20	6.0	Ölfus, Hveragerði
1732/09/07	64.00	20.04	6.7	Land, Leirubakki?
1734/03/21	63.90	20.83	6.8	Flói, Litlu-Reykir?
1766/09/09	63.90	21.16	6.0	Ölfus, Gljúfur Kross
1784/08/14	63.90	20.47	7.1	Holt - Gíslholtsvatn
1784/08/16	63.90	20.95	6.7	Flói - Laugardælir
1829/02/21	63.90	20.0	6.0	Rangárvellir - Hekla
1896/08/26	64.00	20.13	6.9	Skarðsfjall - Fellsmúli
1896/08/27	64.00	20.26	6.7	Flagbjarnarh. -Lækjarbotnar
1896/09/05	63.90	21.04	6.0	Selfoss - Ingólfsfjall
1896/09/05	64.00	20.57	6.5	Skeið - Arakot -Borgarkot
1896/09/06	63.90	21.20	6.0	Ölfus - Hveragerði
1912/05/06	63.90	19.95	7.0	Selsund - Galtalækur
2000/06/17	63.973	20.367	6.6(6.5)	Holt, Skammbeinsstaðir
2000/06/21	63.972	20.711	6.5(6.4)	Flói, Grímsnes, Hestvatn
2008/05/29	63.972	21.072	6.3(5.8,5.9)	Ölfus doublet (Ingólfsfjall, Kross)

Notes: Moderate size ($M > 6$) earthquakes in SISZ since 1600. The magnitudes of the events we report are MS and the moment magnitudes for events in 2000 and 2008, estimated from geodetic studies are given in parenthesis.

SISZ and interpreted as evidence for the SISZ being a young and immature fault zone (Bjarnason *et al.* 1993a).

4.2 The 2000–2008 earthquake sequence in a tectonic context

The SISZ accommodates 18–20 mm yr^{-1} of relative plate motion across an approximately 20 km wide N–S zone. The strain accumulated during a century could therefore be released as ∼2 m of coseismic slip along the E–W length of the zone. The May 29 events follow the faulting pattern observed in earlier events, which limits the seismic hazard to magnitude 6–7 earthquakes rupturing 10–20 km long N–S faults instead of the ∼80 km E–W transform along the SISZ. To model the earthquake cycle in the SISZ we assume that moment accumulated by deep shear in the SISZ is released by brittle failure in the crust. Sigmundsson *et al.* (1995) showed that the moment release by rupture of many closely spaced, short N–S faults is equivalent to that released by a single E–W transform fault for the SISZ. We therefore calculate the geodetic moment built up by plate motion using an average constant locking depth ranging between the estimates for the eastern and western part of the SISZ (12 ± 2 km) (e.g. Tryggvason *et al.* 2002; Árnadóttir *et al.* 2006), and a constant rate of slip (19 ± 1 mm yr^{-1}) in an 80 km E–W zone. We compare this moment accumulation to the moment released in moderate size ($M > 6$) earthquakes. A list of significant earthquakes in the SISZ since 1600 AD is given in Table 3. The magnitudes of events are after Stefánsson & Halldórsson (1988) and are based on the size of destruction areas of the historical earthquakes as published by Björnsson & Einarsson (1981). The identification of the source faults of these earthquakes is given by Einarsson *et al.* (1981), Einarsson & Eiríksson (1982), Bjarnason *et al.* (1993a) and Khodayar *et al.* (2007) and is based on field mapping of surface ruptures and historical documents compiled by Thoroddsen (1899, 1925).

The geodetic moment accumulation and seismic moment release from this model is shown in Fig. 14. The start of the loading history is arbitrarily adjusted so that the 1912 event produces a complete release of the accumulated moment. Fig. 14 shows that the model is consistent with an almost complete release of the accumulated

moment during 1732–1784, and in 1630. During a seismic cycle in the SISZ the moment is built up by plate motion and completely released by earthquakes in the whole zone, whether they occur in one or more earthquake sequences and single events (Fig. 14). This indicates that the seismic cycle in the SISZ is 130–150 yr, whereas the time between historical earthquake sequences in the SISZ varies between 45 and 112 yr with the individual earthquake sequences lasting up to 2 yr (Einarsson *et al.* 1981). For example, the 1732 and 1734 earthquakes are considered to be an earthquake sequence, as are the two 1784 magnitude 7.1 and 6.7 events that occurred in a span of 2 d, whereas the 1912 event is often given as an example of a single event, not considered part of the 1896 earthquake sequence (Einarsson *et al.* 1981). We see that it took 16 yr (1896–1912) to release the moment accumulated by ∼100 yr of plate motion, whereas the accumulated moment was released over a much longer time interval (1732–1784) in two main earthquake sequences during the preceding earthquake cycle. Whether one considers the 2000 June and 2008 May events as the same sequence or two separate sequences, it is clear from Fig. 14 that the moment release in the 2000–2008 events is less than in the 1896 sequence (after five M_S = 6–6.9 events). This indicates that there is still potential for a moment release equivalent to a M_w = 7 event in South Iceland. We note, however, that the accuracy of the seismic history is critical for this analysis and a change of ±0.05 in the estimated magnitudes can lead to different scenarios. Furthermore, this analysis does not identify what segment of the SISZ will rupture in the next moderate size event(s). The 2000–2008 June sequence has now reached the western part of the SISZ and more detailed studies, including a plate boundary model that accounts for the crustal thickening and stress changes due to post-seismic deformation is needed to address whether the activity is likely continue with similar size or larger events in the eastern part of the SISZ or with moderate size earthquakes in the central and/or western part of the region.

5 CONCLUSIONS

We present models of the faults that ruptured in the 2008 May 29 earthquake doublet in the South Iceland Seismic Zone. We use a
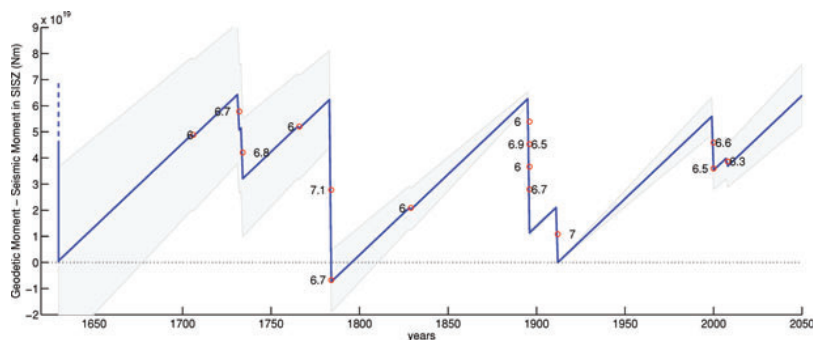
Figure 14. Model of the seismic cycle in the SISZ as a function of time since 1600. The interseismic periods are represented by the accumulation of geodetic moment in the SISZ, as explained in the text. The seismic moment released in moderate size events in the SISZ (red circles) is calculated for the events listed in Table 3. The grey area shows the range of possible values assuming a ± 0.05 uncertainty in the seismic magnitude estimates and ± 2 km in the locking depth.

joint inversion of InSAR and GPS data to estimate the geometry, location and distribution of the slip on the fault planes. In our models we account for the depth dependence of the elastic parameters in the Icelandic crust. We interpret the May 29 events as earthquakes rupturing two vertical N–S right-lateral strike-slip faults. The first rupture occurred along the Ingólfsfjall fault and our models indicate localized and shallow slip. The second event was triggered on the Kross fault. The depth extent of the ruptures are shallower than found in models for the 2000 June events, which is consistent with the brittle part of the crust thickening towards the east along the SISZ. Aftershock locations correlate spatially with both static Coulomb failure stress changes and the areas of high coseismic slip is adjacent to concentrations of aftershocks. Our models have geodetic moments of 8.65×10^{17} and 5.97×10^{17} Nm, corresponding to moment magnitudes of $M_w = 5.9$ and 5.8 for the Kross and the Ingólfsfjall faults, respectively. The June 2000–2008 earthquake sequence has only released about half of the moment accumulated by plate motion since the last major earthquake sequence in the SISZ (1896–1912). It is therefore likely that the sequence will continue with moderate size earthquakes in the SISZ in the coming years.

ACKNOWLEDGMENTS

REFERENCES

Antonioli, A., Belardinelli, M., Bizzarri, A. & Vogfjörd, K.S., 2006. Evidence of instantaneous dynamic triggering during the seismic se-

quence of year 2000 in south Iceland, *J. geophys. Res.,* **111,** B03302, doi:10.1029/2005JB003935.

Árnadóttir, T., Hreinsdóttir, S., Gudmundsson, G., Einarsson, P., Heinert, M. & Völksen, C., 2001. Crustal deformation measured by GPS in the South Iceland Seismic Zone due to two large earthquakes in June 2000, *Geophys. Res. Lett.,* **28,** 4031–4033.

Árnadóttir, T., Jónsson, S., Pedersen, R. & Gudmundsson, G.B., 2003. Coulomb stress changes in the South Iceland Seismic Zone due to two large earthquakes in June 2000, *Geophys. Res. Lett.,* **30**(5), 1205, doi:10.1029/2002GL016495.

Árnadóttir, T., Geirsson, H. & Einarsson, P., 2004. Coseismic stress changes and crustal deformation on the Reykjanes Peninsula due to triggered earthquakes on 17 June 2000, *J. geophys. Res.,* **109,** B09307, doi:10.1029/2004JB003130.

Árnadóttir, T., Jiang, W., Feigl, K.L., Geirsson, H. & Sturkell, E., 2006. Kinematic models of plate boundary deformation in southwest Iceland derived from GPS observations, *J. geophys. Res.,* **111,** B07402, doi:10.1029/2005JB003907.

Bellou, M., Bergerat, F., Angelier, J. & Homberg, C., 2005. Geometry and segmentation mechanisms of the surfaces traces associated with the 1912 Selsund earthquake, southern Iceland, *Tectonophysics,* **404,** 133–149.

Bjarnason, I., Cowie, P., Anders, M.H., Seeber, L. & Scholz, C.H., 1993a. The 1912 Iceland earthquake rupture: growth and development of a nascent transform system, *Bull. seism. Soc. Am.,* **83,** 416–435.

Bjarnason, I., Menke, W., Flóvenz, Ó.G. & Caress, D., 1993b. Tomographic image of the mid-Atlantic plate boundary in southwestern Iceland, *J. geophys. Res.,* **98,** 6607–6622.

Björnsson, S. & Einarsson, P., 1981. Jarðskjálftar (Earthquakes, in Icelandic), in *Náttúra Íslands,* pp. 121–155, eds Þórarinsdóttir, H. & Steinþórsson, S., Almenna Bókafélagið, Reykjavík.

Clifton, A.E. & Einarsson, P., 2005. Styles of surface rupture analysis accompanying the June 17 and 21, 2000 earthquakes in the South Iceland Seismic Zone, *Tectonophysics,* **396,** 141–159.

Clifton, A.E., Pagli, C., Jónsdóttir, J.F., Eythórsdóttir, K. & Vogfjörd, K., 2003. Surface effects of triggered fault slip on Reykjanes Peninsula, SW Iceland, *Tectonophysics,* **369,** 145–154.

Cohee, B.P. & Beroza, G.C., 1994. Slip distribution of the 1992 Landers earthquake and its implications for earthquake source mechanics, *Bull. seism. Soc. Am.,* **84,** 692–712.

Dach, R., Hugentobler, U., Fridez, P. & Meindl, M., 2007. Bernese GPS software version 5.0, Technical report, Astronomical Institure, University of Bern, Bern, Switzerland.

Decriem, J. *et al.*, 2008. Unraveling faulting in a complex earthquake sequence in the South Iceland Seismic Zone, in *EOS, Trans. Am. geophys. Un.,* **89**(53), Fall Meet. Suppl., Abstract T41A-1926, AGU.

DeMets, C.G., Gordon, R., Argus, D.F. & Stein, S., 1994. Effect of recent revisions to the geomagnetic reversal time scale on

estimates of current plate motions, *Geophys. Res. Lett.,* **21,** 2191–2194.

Dubois, L., Feigl, K.L., Komatitsch, D., Árnadóttir, T. & Sigmundsson, F., 2008. Three-dimensional mechanical models for the June 2000 earthquake sequence in the south Iceland seismic zone, *Tectonophysics,* **457,** 12–29.

Einarsson, P., 1991. Earthquakes and present-day tectonism in Iceland, *Tectonophysics,* **189,** 261–279.

Einarsson, P. & Eiríksson, J., 1982. Earthquake fractures in the districts Land and Rangárvellir in the South Iceland Seismic Zone, *Jökull,* **32,** 113–120.

Einarsson, P., Björnsson, S., Foulger, G., Stefánsson, R. & Skaftadóttir, T., 1981. Seismicity pattern in the South Iceland Seismic Zone, in *Earthquake Prediction—An International Review,* Vol. 4, pp. 141–151, eds Simpson, D.W. & Richards, P.G., AGU, Washington DC.

Foulger, G.R., Bilham, R., Morgan, W.J. & Einarsson, P., 1987. The Icelandic GPS geodetic field campaign 1986, *EOS, Trans. Am. geophys. Un.,* **68,** 1809.

Fukuda, J. & Johnson, K.M., 2008. A fully Bayesian inversion for spatial distribution of fault slip with objective smoothing, *Bull. seism. Soc. Am.,* **3,** 1128–1146.

Geirsson, H., Árnadóttir, T., Völksen, C., Jiang, W., Sturkell, E., Villemin, T., Einarsson, P. & Sigmundsson, F., 2006. Current plate movements across the Mid-Atlantic ridge determined from 5 years of continuous GPS measurements in Iceland, *J. geophys. Res.,* **111,** B09407, doi:10.1029/2005JB003717.

Halldórsson, B. & Sigbjörnsson, R., 2009. The M_w6.3 Ölfus earthquake at 15:45 UTC on May 29 2008 in South Iceland: ICEARRAY strong-motion recordings, *Soil Dyn. Earthq. Eng.,* **29,** 1073–1083, doi:10.1016/j.soildyn.2008.12.006.

Harris, R.A., 1998. Introduction to special section: stress triggers, stress shadows, and implications for seismic hazard, *J. geophys. Res.,* **103,** 24 347–24 358.

Herring, T.A., King, R.W. & McClusky, S.C., 2006. GLOBK reference manual, Global Kalman filter VLBI and GPS analysis program, release 10.3, Technical report, *Mass. Inst. Technol.,* Cambridge, MA, USA.

Hjaltadóttir, S., 2009. Use of relatively located microearthquakes to map fault patterns and estimate the thickness of the brittle crust in Soutwest Iceland, *Master's thesis,* Faculty of Earth Sciences, University of Iceland, Reykjavík, Iceland.

Hooper, A., Segall, P., Johnson, K. & Zebker, H.A., 2007. Persistent scatterer InSAR for crustal deformation analysis, with application to Volcan Alcedo, Galapagos, *J. geophys. Res.,* **112,** B07407, doi:10.1029/2006JB004763.

Hooper, A., 2009. A statistical-cost approach to unwrapping the phase of InSAR time series, in *Proceedings of ESA FRINGE Workshop, Frescati, Italy, November 30–December 4, 2009,* in press.

Hreinsdóttir, S., Einarsson, P. & Sigmundsson, F., 2001. Crustal deformation at the oblique spreading Reykjanes Peninsula, SW Iceland: GPS measurements from 1993 to 1998, *J. geophys. Res.,* **106,** 13 803–13 816.

Hreinsdóttir, S., Árnadóttir, T., Decriem, J., Bayesson, H., Geirsson, H., Bennett, R.A. & LaFemina, P., 2009. A complex earthquake sequence captured by the continuous GPS network in SW Iceland, *Geophys. Res. Lett.,* **36,** L12309.

Johanson, I., Fielding, E.J., Rolandone, F. & Bürgmann, R., 2006. Coseismic and postseismic slip of the 2004 Parkfield earthquake from space-geodetic data, *Bull. seism. Soc. Am.,* **96,** 5269–5282.

Jónsson, S., 2008. Importance of post-seismic viscous relaxation in southern Iceland, *Nature,* **1,** 136–139.

Jónsson, S., Zebker, H.A., Segall, P. & Amelung, F., 2002. Fault slip distribution of the 1999 M_w7.2 Hector Mine earthquake, California, estimated from satellite radar and GPS measurements, *Bull. seism. Soc. Am.,* **92,** 1377–1389.

Jónsson, S., Segall, P., Pedersen, R. & Björnsson, G., 2003. Post-earthquake ground movements correlated to pore-pressure transients, *Nature,* **424,** 179–183.

Keiding, M., Árnadóttir, T., Sturkell, E., Geirsson, H. & Lund, B., 2008. Strain accumulation along an oblique plate boundary: the

Reykjanes Peninsula, southwest Iceland, *Geophys. J. Int.,* **172**(1), 861–872, doi:10.1111/j.1365-246X.2007.03655.x.

Khodayar, M., Franzson, H., Einarsson, P. & Björnsson, S., 2007. Hvammsvirkjun. Geological investigation of Skarðsfjall in the South Iceland Seismic Zone., Technical report. ÍSOR-2007/017, LV-2007/065, Íslenskar Orkurannsóknir, Reykjavík, Iceland.

LaFemina, P.C., Dixon, T.H., Malservisi, R., Árnadóttir, T., Sturkell, E., Sigmundsson, F. & Einarsson, P., 2005. Geodetic GPS measurements in south Iceland: strain accumulation and partitioning in a propagating ridge system, *J. geophys. Res.,* **110,** B11405, doi:10.1029/2005JB003675.

Lawson, C. & Hanson, R., 1974. *Solving Least Squares Problems,* Prentice Hall, Englewood Cliffs.

Lindman, M., 2009. Physics of aftershocks in the South Iceland Seismic Zone, *PhD thesis,* Faculty of Science and Technology, Uppsala University, Uppsala, Sweden.

Massonnet, D. & Feigl, K.L., 1993. Radar interferometry and its application to changes in the earth's surface, *Rev. Geophys.,* **36**(4), 441–550.

Matthews, M. & Segall, P., 1993. Statistical inversion of crustal deformation data and estimation of the depth distribution of slip in the 1906 earthquake, *J. geophys. Res.,* **98,** 12 153–12 163.

McClusky, S. *et al.,* 2000. Global Positioning System constraints on plate kinematics and dynamics in the eastern Mediterranean and Caucasus, *J. geophys. Res.,* **105**(B3), 5695–5720.

Metropolis, N., Rosenbluth, A., Rosenbluth, M., Teller, A. & Teller, E., 1953. Equations of State Calculations by Fast Computing Machines, *J. Chem. Phys.,* **21,** 1087–1091.

Pagli, C., Pedersen, R., Sigmundsson, F. & Feigl, K.L., 2003. Triggered seismicity on June 17, 2000 on Reykjanes Peninsula, SW-Iceland captured by radar interferometry, *Geophys. Res. Lett.,* **30**(6), 1273, doi:10.1029/2002GL015310.

Pedersen, R., Sigmundsson, F., Feigl, K.L. & Árnadóttir, T., 2001. Coseismic interferograms of two M_s = 6.6 earthquakes in the South Iceland Seismic Zone, June 2000, *Geophys. Res. Lett.,* **28,** 3341–3344.

Pedersen, R., Jónsson, S., Árnadóttir, T., Sigmundsson, F. & Feigl, K.L., 2003. Fault slip distribution of two M_w = 6.5 earthquakes in South Iceland estimated from joint inversion of InSAR and GPS measurements, *Earth planet Sci. Lett.,* **213,** 487–502.

Sella, G.F., Dixon, T.H. & Mao, A., 2002. REVEL: a model for recent plate velocities from space geodesy, *J. geophys. Res.,* **107,** ETG 11–1–31, doi:10.1029/2000JB000033.

Sigmundsson, F., Einarsson, P., Bilham, R. & Sturkell, E., 1995. Rift-transform kinematics in south Iceland: deformation from Global Positioning System measurements, 1986 and 1992, *J. geophys. Res.,* **100,** 6235–6248.

Stefánsson, R. & Halldórsson, P., 1988. Strain release and strain build-up in the south Iceland seismic zone, *Tectonophysics,* **152,** 267–276.

Stefánsson, R. *et al.,* 1993. Earthquake Prediction Research in the South Iceland Seismic Zone and the SIL Project, *Bull. seism. Soc. Am.,* **83**(3), 696–716.

Sudhaus, H. & Jónsson, S., 2008. Improved source modelling through combined use of InSAR and GPS under consideration of correlated data errors: application to the June 2000 Kleifarvatn earthquake, Iceland, *Geophys. J. Int.,* **176,** 389–404.

Tarantola, A., 2005. *Inverse Problem Theory and Methods for Parameter Estimation,* SIAM, Philadelphia.

Thoroddsen, T., 1899. Jarðskjálftar á Suðurlandi (Earthquakes in South Iceland, in Icelandic), *Hið íslenska bókmenntafélag (The Icelandic Literary Society),* p. 269.

Thoroddsen, T., 1925. Die Geschichte der Isländischen Vulkane (The history of Icelandic volcanoes, in German), *D. Kgl. Danske Vidensk. Selsk. Skrifter,* p. 458 and 5 pl.

Tryggvason, A., Rögnvaldsson, S.T. & Flóvenz, Ó.G., 2002. Three-dimensional imaging of the *P*- and *S*-wave velocity structure and earthquake locations beneath Southwest Iceland, *Geophys. J. Int.,* **151,** 848–866.

Vogfjörd, K.S., 2003. Triggered seismicity in SW Iceland after the June 17, M_w = 6.5 earthquake in the South Iceland Seismic Zone: the first

five mintues, in *Geophys. Res. Abs.,* EAE03-A-11251, Vol. 5, European Geosciences Union.

Wang, R., Lorenzo, F. & Roth, F., 2006. PSGRN/PSCMP—a new code for calculating co- and post-seismic deformation, geoid and gravity changes based on viscoelastic-gravitational dislocation theory, *Comput. Geosci.,* **32,** 527–541.

SUPPORTING INFORMATION

Additional Supporting Information may be found in the online version of this article:

Figure S1. Resolution analysis for the non-uniform model for the Ingólfsfjall (left-hand panel) and the Kross fault (right-hand panel), using GPS data only (first row), InSAR data only (second row), and GPS and InSAR (third row). Contours show the preferred slip distribution. The colour scale indicates the level of resolution, with one well-resolved areas and zero unresolved areas. Both fault are reasonably well resolved (>0.1) down to ∼6 km depth, where most of the coseismic slip is inferred.

Table S1. Coseismic GPS station offsets.

Table S2. Selected InSAR interferograms spanning the 2008 May 29 earthquakes.

Please note: Wiley-Blackwell are not responsible for the content or functionality of any supporting materials supplied by the authors. Any queries (other than missing material) should be directed to the corresponding author for the article.

Decriem J. and Árnadóttir Th., Transient crustal deformation in the South Iceland Seismic Zone observed by GPS and InSAR during 2000-2008, *submitted to Tectonophysics, 2010.*

Transient crustal deformation in the South Iceland Seismic Zone observed by GPS and InSAR during 2000-2008

J. Decriem[a], T. Árnadóttir[a]

[a]*Nordic Volcanological Center,Institute of Earth Sciences,University of Iceland,IS-101 Reykjavík, Iceland (judicael@hi.is)*

Abstract

Repeated geodetic (GPS and InSAR) observations in the South Iceland Seismic Zone (SISZ) show transient surface deformation signals following two M6.5 earthquakes in 2000 June. Previous studies concluded that the postseismic signal observed during the 2000–2005 time period was most likely due to viscoelastic relaxation in the lower crust and upper mantle signal, rather than afterslip (Árnadóttir et al., 2005; Jónsson, 2008). The ~5 years transient signal was modelled assuming Maxwell rheology in the lower crust with a viscosity of $1 \cdot 10^{19}$ Pa s and either Burgers body rheology or two Maxwell layers to represent material behaviour in the upper mantle and viscosity in the range $1\text{-}3 \cdot 10^{18}$ Pa s. Here, we extend the GPS dataset used in the previous studies by adding both continuous and campaign observations from 2004 to 2008. Our analysis indicate that the postseismic signal is very small after 2005. We explore viscoelastic models using Maxwell and standard linear solid (SLS) rheologies to reproduce the surface velocities observed during 2000–2008. Our preferred model consists of a thick (~15 km) elastic crust overlying a SLS upper mantle with a viscosity of $1 \cdot 10^{18}$ Pa s and relaxation strength between 0.1–0.25. This model produces a more rapid decay in the surface velocities, and hence is more compatible with our observations, than models including a lower crust with a viscosity of $1 \cdot 10^{19}$ Pa s, and Maxwell rheology. The 2000 June earthquakes were followed 8 years later with an earthquake doublet of composite magnitude 6.3 in the western part of the SISZ. We find that the Coulomb failure stress change due to viscoelastic relaxation increased the loading of the faults that ruptured in 2008 May by about 0.05 MPa. This stress increase is, however, an order of magnitude smaller than the static stress changes estimated for the 2000 June main shocks. The viscoelastic relaxation may therefore not be the primary loading mechanism necessary to explain the delay between the 2000 June and the 2008 May earthquakes.

Keywords: Viscoelastic relaxation, South Iceland Seismic Zone, crustal deformation, stress changes, GPS, InSAR

1. Introduction

Seismic and volcanic activity in Iceland is the result of plate spreading between the North American and Eurasian plates. The rate of plate divergence across the island is ~19 mm/yr (DeMets et al., 1994). The left-lateral shear across the southern part of Iceland is accommodated by an approximately 80 km long E–W transform zone, the South Iceland Seismic Zone (SISZ) (Fig. 1). The SISZ translates the motion between the main spreading sections of the plate

boundary in south Iceland, i.e., the Western Volcanic Zone (WVZ), and the Reykjanes Peninsula (oblique spreading), in the west, to the Eastern Volcanic Zone (EVZ).

Earthquake activity in south Iceland has been recorded by the SIL seismic network operated by the Icelandic Meteorological Office, since 1989 (Stefánsson et al., 1993). Mapping of surface faults in the SISZ has highlighted arrays of N–S right lateral strike slip faults, spaced 2–5 km, each array made up of numerous left stepping *en echelon* surface fractures (Einarsson, 2008; Clifton and Einarsson, 2005).

Two M6.5 earthquakes occurred on 2000 June 17 and 21, and were the first major events in the SISZ since a M7 earthquake in 1912 (Fig. 1). The surface deformation caused by the 2000 June main shocks was measured using both GPS and Interferometric Synthetic Aperture Radar (InSAR) techniques. Modelling of the geodetic data suggests up to 2.5 m of slip on two parallel 10 km long N–S faults (Árnadóttir et al., 2001; Pedersen et al., 2001, 2003). The SIL seismic system recorded thousands of aftershocks, and relative relocations indicate that the faults that ruptured in the 2000 June main shocks are nearly vertical, linear features, extending down to about 10 km depth (Hjaltadóttir, 2009), despite complexities observed in the surface ruptures (Clifton and Einarsson, 2005).

The 2000 June main shocks increased the static Coulomb stress in the areas east of the June 17 rupture and west of the June 21 fault (Árnadóttir et al., 2003). Considering that the seismic moment accumulated by plate motion since the 1912 earthquake were not fully released by the 2000 June sequence, further earthquake activity in the SISZ was expected (Árnadóttir et al., 2003; Pedersen et al., 2003). In 2008 May two M6 earthquakes struck in the western part of the SISZ. The two main events ruptured N–S oriented faults, located only ~5 km apart within a few seconds of each other (Hreinsdóttir et al., 2009; Decriem et al., 2010).

The 2000 June earthquake sequence provided the first opportunity to study postseismic deformation in Iceland (Jónsson et al., 2003; Árnadóttir et al., 2005). Several mechanisms have been suggested to explain postseismic deformation at different temporal and spatial scales, namely pore fluid flow, viscoelastic relaxation, and afterslip.

Poroelastic rebound is driven by pore pressure equilibration caused by coseismic stress changes. Fluids in the crust move from areas of high pressure to low pressure, according to Darcy's law. This fluid displacement affects the volumetric strain of the rock, and causes deformation that is in the opposite sense to the coseismic deformation. For example, in the case of faulting on a N–S right-lateral strike slip fault, the coseismic motion causes compression and uplift, and hence an increase in pore pressure in the NW and SE quadrants, and dilation as well as lowering of pore pressure in the SW and NE quadrants. Following the earthquake the fluids are therefore driven from the area of high pressure (NW and SE of the fault) toward the areas of pressure decrease. As a result of fluid flow to these areas, we may observe uplift SW and NE of the fault during the weeks to months following the earthquake. Poroelastic relaxation mostly occurs in the shallow crust where the rock matrix behaves elastically. Poroelastic deformation has been suggested to explain short term deformation transients following several earthquakes, for example the 1992 Landers M7.4 earthquake (Peltzer et al., 1998), the 2000 June M6.5 events (Jónsson et al., 2003) and the 2002 Denali M7.9 main shock (Freed et al., 2006).

Coseismic stresses may also relax by viscoelastic flow in the lower crust and upper mantle. The time scale of viscoelastic relaxation depends on the rheology, and most often occurs over years or decades. This mechanism has been used to explain the broad (10-100 km) long term deformation signals following moderate to large earthquakes, such as the 1992 Landers M7.4 (Deng et al., 1998; Pollitz et al., 2000), the 1997 Manyi Mw7.6 (Ryder et al., 2007), the 1999 Hector Mine M7.1 (Pollitz et al., 2001), the 1999 Izmit M7.4 (Wang et al., 2009), and the 2002

Denali M7.9 (Pollitz, 2005), and 2004 Sumatra-Andaman M9.2 (Masterlark and Hughes, 2008; Pollitz et al., 2008) events. Viscoelastic relaxation has also been used to model the deformation following the 2000 June SISZ events (Árnadóttir et al., 2005; Jónsson, 2008). Several types of rheologies have been used to describe the viscoelastic behaviour of the lower crust and upper mantle. Most commonly, studies assume a Maxwell rheology using linear elements to represent the lower crust and the upper mantle (Jónsson, 2008). Other studies invoke more complicated rheologies, albeit a combination of linear elements, such as Burgers body (Pollitz, 2003, 2005; Árnadóttir et al., 2005), and standard linear solid (SLS) element combined with a Maxwell linear element (Wang et al., 2009). A few studies argue for stress and temperature dependent non-linear rheology (power law creep) (e.g. Freed and Bürgman, 2004). It is not clear, however, which of these rheologies best characterises the lower crust and the mantle. In most cases postseismic deformation due to viscoelastic flow requires at least the sum of two exponential functions. The simple linear rheologies can however usually only explain a short period of the observations, whereas a combination of linear rheologies, such as Burgers body and SLS, or non-linear models (power law) are more successful in explaining both the rapid short term transient in the months following an earthquake as well as longer term deformation signals lasting for years to decades. Viscoelastic relaxation is a reasonable physical model to explain long term transient deformation, but may, however, not fully account for the deformation in the first months following an earthquake, during which poroelastic and/or afterslip may also be occurring.

Afterslip, i.e., slip in the area outside the main coseismic rupture, is another mechanism that has been suggested to explain deformation observed during the months/years following an earthquake. There are, however, very large variations in the amount of afterslip from one event to another (Melbourne et al., 2002; Pritchard and Simons, 2006). For example, the cumulative seismic moment released by afterslip for the 1994 Sanriku-Haruka-Oki M7.6 earthquake has been estimated to be as large as the coseismic moment (Heki et al., 1997), and about twice the coseismic moment for the 2004 Parkfield event (Langbein et al., 2006). Jónsson (2008) argues that only a small fraction, if any, of the postseismic signal measured after the 2000 June events in the SISZ is caused by afterslip.

2. GPS data and analysis

The surface deformation in the SISZ following the 2000 June earthquakes has been measured by annual GPS campaigns (Árnadóttir et al., 2005, 2006). Here we extend the dataset used in the previous postseismic GPS study in the SISZ (Árnadóttir et al., 2005) with measurements from 2005 to 2008. The campaign measurements have been done during spring time, usually around May to minimise the effect of seasonal signals. At the time of the 2000 June earthquakes the closest CGPS station (HVER) was about 25 km west of the June 21 epicentre. Since then, many new continuous GPS (CGPS) stations have been installed in Iceland, including two stations in the SISZ (KIDJ in 2001, and SELF in 2002), and three stations in 2007 (KALT, SAUR, HAUD).

We analyse all available GPS campaign and continuous data from 2000 to 2008, in order to estimate the postseismic deformation in the entire GPS network in south Iceland. We calculate daily solutions using the Bernese v5.0 software (Dach et al., 2007) with orbit information and Earth rotation parameters from the International GPS Service (IGS) in the International Terrestrial Reference Frame (ITRF) 2005 (Altamimi et al., 2007). For each 24 hr session we include GPS campaign data, CGPS data from stations in Iceland, and data from 40 long-running CGPS stations outside of Iceland. We use the GLOBK software (Herring et al., 2006) to combine our local solution with three IGS global network solutions (IGS1, IGS3 and EURA) using a regional

3

stabilisation approach (McClusky et al., 2000). We realise the ITRF05 reference frame based on 40 global stations and estimate positions and velocities for three time intervals (2000–2001, 2001–2004, and 2004–2008). For clarity we show the velocities as the average of two solutions, for stable NA and stable Eurasia, such that the motion across the SISZ is symmetric (Fig. 2).

Deformation due to pore pressure readjustments was observed by InSAR, indicating that this process takes place during the first two months following the 2000 June earthquakes (Jónsson et al., 2003). We therefore correct the GPS displacements observed during the first year (2000–2001) for poroelastic deformation using the model suggested by Jónsson et al. (2003).

First, we calculate the coseismic deformation using the fault models derived by Pedersen et al. (2003), assuming a Poisson's ratio of 0.28 (undrained conditions). From this we subtract the coseismic deformation estimated using a different Poisson's ratio ($\nu = 0.25$, fluid in pressure equilibrium), to obtain the deformation induced by the pore pressure changes only. The corrected velocities for the first year are shown in Fig. 2A, indicating that stations are moving at up to twice the expected plate spreading rate. The deformation pattern is similar to the coseismic deformation, although much smaller, i.e., stations move from extensional coseismic quadrants (SW and NE) toward compressional coseismic quadrants (NW and SE). Therefore it is unlikely that the deformation is due to additional fluid re-equilibration, as the pore-pressure induced deformation has the opposite sign to the coseismic deformation. The area in between the two faults shows complex pattern of deformation, especially south of plate boundary.

The 2001–2004 velocities (Fig. 2B) show a similar pattern as observed during the first year, but at a slower rate. The velocities at stations VOHO, SNAS, LYTI and NONH near the southern end of the June 17 fault are three to four times smaller than during 2000–2001. Stations northwest of the June 21 fault (BURF, KERH, BRJA, FRAM and BIRN) move at almost half the rate observed during the first year.

The postseismic deformation signal appears to be very small during 2004–2008 (Fig. 2C, and Fig. 3). Stations close to the plate boundary show small or no significant displacements. The exceptions are stations BURF, SELH and BRJA, which move at a faster rate with a coherent trend toward northwest. It is difficult to relate this pattern to postseismic deformation considering the slower rates at stations south of this area (ONDV, KIDJ). Apart from BURF, SELH and BRJA the stations move at a rate that is consistent with the expected interseismic plate motion (Fig. 4).

3. InSAR data

We use three averaged profiles of InSAR observations from Jónsson (2008), spanning the 2000–2005 period (Fig. 5). In addition, we have processed ENVISAT data from tracks T95, T138, T367 and T402 spanning 2006 to 2008 using the DORIS software. We tested several master images, minimising both the temporal and the perpendicular baseline. Unfortunately, the coherence is not sufficiently good in the SISZ for this time period to obtain coherent images over a sufficiently large area and a long enough time period. We get reasonable coherence when the acquisitions are close in time, but due to the small deformation rates that we are trying to extract, we do not find significant deformation in SISZ. This is consistent with the 2004–2008 GPS velocities, indicating that the postseismic signal after 2005 is most likely very small.

4. Secular plate motion

The deformation we observe in the SISZ after 2000 June is primarily due to secular plate motion, and the postseismic signals. In order to model the postseismic deformation we must

therefore first correct for the steady state plate motion across the SISZ. The plate boundary in southern Iceland is, however, complex, with overlapping rift zones, oblique spreading and several active volcanoes, as well as the SISZ transform (Árnadóttir et al., 2005, 2006; Árnadóttir et al., 2009; LaFemina et al., 2005). Other processes, such as utilisation of geothermal fields may locally affect the surface deformation in the southernmost part of the WVZ (Keiding et al., 2010). To minimise the effect of processes other than plate motion we use GPS data from the central part of the SISZ, between 21.2° and 19.8° West longitude, and 63.4° and 64.3° North latitude. Our study area extends sufficiently far north and south of the SISZ to include stations moving at close to the full plate velocity (LAUG, KOPS, HLFJ to the north and VMEY to the south). Fig. 3 shows the velocities estimated for the 2004–2008 time period relative to the SISZ transform. Stations along the plate boundary (e.g., 265S, GIVA, KRHR) show almost no displacement during this time interval.

To model the secular motion, we assume that the Earth is an elastic half-space and that the SISZ can be approximated with an E–W left lateral shear dislocation. Our dislocation model thus represents the steady state plate motion that is accommodated by E–W shearing below seismogenic depth. We assume that the dislocation length and width is much greater than the E–W extent of the SISZ. We estimate the location, dip, strike, locking depth, and the rate of strike slip, that best fit the 2004–2008 GPS velocities using a nonlinear inversion scheme (e.g. Árnadóttir et al., 2006). Our best fit dislocation model has a strike slip rate of 19 mm/yr below 9.5 km, an E–W strike (N93E°), and a near vertical dip (85°). The locking depth we estimate for our model is consistent with maximum depths of micro-earthquakes, down to magnitude less than zero, indicating that the brittle crust extends down to approximately 10 km depth in the SISZ (e.g. Stefánsson et al., 1993; Hjaltadóttir, 2009). Our model is able to reproduce the observed velocity at the most distant stations (Fig. 3). The stations BURF, SELH, and BRJA have the largest misfit, moving faster towards west and north than the dislocation model predicts. We think that the misfit at these stations is due to a local process that we have not identified yet.

5. Viscoelastic modelling

In this section we explore a range of viscoelastic models to explain the surface deformation following the 2000 June earthquakes. Before trying to model the postseismic signal in our data, it is, however, helpful to explore how the different rheological model parameters affect the surface deformation. Fig. 6 shows the mechanical analogs (springs and dashpots) used to describe Maxwell, Burgers body, and SLS rheologies. The characteristic model predictions that we are most interested in are the total displacements in the fully relaxed state (i.e., after the transient signal has disappeared) and the decay time of the transient phase. We run forward model calculations for Maxwell and SLS rheologies varying one model parameter at a time to examine how the parameters affect the predicted surface deformation. The earthquake source is a vertical N–S right lateral strike slip fault extending from the surface to 10 km depth with 1 m of coseismic slip. For simplicity, we show the surface deformation as a function of time at a point in the NE quadrant, 15 km away from the centre of the fault (Fig. 7).

The first model we examine has a 20 km thick elastic plate and Maxwell rheology below (Fig. 7A). We observe that as we increase the half-space viscosity (η) the relaxation time of the transient also increases. This relationship is apparent from the equation $\rho = \rho_0 \exp(-\frac{\mu t}{\eta})$, stating that the stress relaxes to $\frac{1}{e}$ of its original value (ρ_0) in the Maxwell time $\tau = \frac{\eta}{\mu}$, where μ the elastic modulii and t is time. It is important to note that in the Maxwell representation the viscosity (η) does not affect the total displacement.

5

In the second model we again assume a Maxwell rheology, but now we keep the viscosity fixed and vary the thickness of the elastic plate (Fig. 7B). We find that the displacements increase with decreasing thickness of the elastic plate. The reason is that the coseismic stress field relaxes over a larger volume if the elastic plate is thin. We also note that the relaxation time of the deformation transient is not affected by the thickness of the elastic plate and only depends on the half-space viscosity.

In the third set of models we use a SLS rheology rather than Maxwell, keeping the viscosity and elastic plate thickness fixed, and vary the relaxation strength of the SLS body (α) (Fig. 7C). As explained in Fig. 6, μ_2 is the unrelaxed modulus and the relaxed shear modulus is $\frac{\mu_1 \mu_2}{\mu_1 + \mu_2} = \alpha \mu_2$. If $\alpha = 1$ the SLS rheology corresponds to perfect elasticity and if $\alpha = 0$ the material behaviour is the same as for Maxwell rheology. Thus, if α is very small (0.01) the surface displacements are similar to the deformation predicted by models with a Maxwell rheology (Fig. 7A), whereas increasing α reduces both the displacement magnitude and the time of the transient (for an elastic body the total coseismic displacement occurs instantaneously).

The last model we examine has a thin elastic plate (from the surface to 10 km depth) and two Maxwell viscoelastic layers with different viscosities (Fig. 7D). We find that varying the viscosity of the two layers does not affect the total displacement, and the total relaxation time depends on the higher viscosity.

From this exercise we see that in the case of Maxwell and SLS rheologies, we can adjust the time of the transient by changing the viscosity (η) and/or the relaxation strength (α), and the displacement by varying the elastic plate thickness and/or α. We note that our models predict the largest postseismic displacement for the fully relaxed solution in the case of Maxwell rheology.

We now turn our attention to the postseismic signals we observe in the SISZ. Our rheological models consist of an elastic plate representing the brittle crust, with a viscoelastic lower crust and upper mantle (Fig. 8). We use the PGRN/PSCMP software to calculate the surface displacements (Wang et al., 2009), and test four different Earth models using both linear Maxwell and SLS rheologies, as indicated in Fig. 8. Model A has a Maxwell lower crust and upper mantle, Model B has SLS rheology in the lower crust and a Maxwell mantle, Model C has a thick elastic crust (20 km) and SLS rheology below. Model D has the same rheological structure as Model C, except we vary elastic plate thickness keeping the viscosity constant at $1 \cdot 10^{18}$ Pa s.

We use data from 29, 44, and 36 GPS stations (3D components) for the three GPS time periods, respectively. The GPS velocities are corrected for poroelastic deformation during the first year, and plate motion for all three years as explained in the previous sections. The three InSAR profiles give one datapoint per year from 2000 to 2005 a total of 18 InSAR LOS observations. The InSAR profiles are average solutions over the three areas shown in Fig. 3. To assess the fit to the models to the InSAR profiles, we calculate the mean solution of five points: the centre and the four corners of the square delimiting the area of each profile.

We calculate the data fit as the weighted residual sum of squares (WRSS), for the GPS velocities during 2000–2001, 2001–2004, and 2004–2008 and three InSAR profiles, varying the model parameters as indicated in Fig. 9. The GPS velocities and model predictions, using the optimal parameters for the combined data and each Earth model, are shown in Fig. 2, and the InSAR LOS in Fig. 5.

Model A has a Maxwell rheology in the lower crust in the depth range 10–20 km, viscosity η_{LC}, and upper mantle below 20 km (viscosity indicated by η_{UM}). From Fig. 9 we see that it is difficult to find a consistent range of viscosities for this model that give reasonable fit to the different time periods spanned by our data. For the 2000–2001 time period $\eta_{LC} > 5 \cdot 10^{18}$ Pa s and $\eta_{UM} > 1\text{-}3 \cdot 10^{18}$ Pa s gives the lowest misfit, whereas lower viscosities (faster relaxation

6

time) overpredicts the data. There is no clear minimum for the 2001–2004 or 2004–2008 GPS velocities, assuming a Maxwell rheology. The lowest mean misfit (WRSS=162, representing 60% of the data variance) is found for rather high lower crust viscosities (> $5 \cdot 10^{19}$ Pa s). Such high viscosities lead to a very long relaxation time (Maxwell time > 5 years). The mean plot indicates that the lowest misfit for all the data for Model A are viscosities in the range of 1-$3 \cdot 10^{18}$ Pa s and $3 \text{-} 7 \cdot 10^{19}$ Pa s for the upper mantle and lower crust, respectively. Such a stiff lower crust contributes very little to the surface displacement rates, but still seems to over predict the station velocities for 2001–2004 and 2004–2008 (Fig. 2).

Next we explore a model with SLS rheology rather than Maxwell in the lower crust (Model B). As we noted earlier, increasing the relaxation coefficient (α), decreases the viscoelastic contribution from the SLS lower crust (Fig 7). We calculate the model response for the same range of viscosities for the lower crust and upper mantle as in model A, varying the relaxation coefficient ($\alpha = 1/3, 1/2$ and $2/3$) in the lower crust. Increasing α gives a larger range of lower crust viscosities that become acceptable for the 2000–2001 GPS velocities. The models have a lower misfit than Model A for 2001–2004 and 2004–2008 velocities, although it still difficult to find a consistent viscosity to explain the deformation during the first year and the following time periods. The lowest misfit is found for Model B with upper mantle viscosities of $1 \text{-} 3 \cdot 10^{18}$ Pa s, whereas for the lower crust we find $5 \text{-} 9 \cdot 10^{19}$ Pa s, $1 \text{-} 5 \cdot 10^{19}$ Pa s and $0.8 \text{-} 5 \cdot 10^{19}$ Pa s giving mean WRSS of 143, 142 and 142 for $\alpha = 1/3, 1/2$ and $2/3$, respectively (~70% of the data variance).

The above modeling indicates that assuming a viscoelastic relaxation in the lower crust produces surface velocities that are too large. We therefore test Model C, which has a thick elastic plate and SLS rheology in the upper mantle for a range of relaxation coefficients (α from 0.01 to 0.66). Although, calculating the surface deformation with different values of α is computer intensive, the relaxation coefficient of the SLS allows us to adjust both the amplitude and time development of the transient signal. We find that the minimum for each time period overlaps more closely than for Models A and B, such that the low misfit region in the mean misfit curve is more consistent with the minimum of each dataset (Fig. 9). Our calculations indicate that viscosities in the range $1 \text{-} 3 \cdot 10^{18}$ Pa s in the upper mantle and relaxation coefficients from 0.1 to 0.25 give the lowest mean misfit (WRSS=140).

Finally, we modify Model C by adjusting the thickness of the elastic plate (Model D), using a constant viscosity of $1 \cdot 10^{18}$ Pa s, and a range of α (Fig. 9). We found a slightly better fit than for the optimal Model C (WRSS=136) if the thickness of the elastic plate is decreased to 15 km, and α close to 0.2. This representation of Model D explains 75% of the signal variance, and is therefore our preferred viscoelastic model.

In Fig. 2 we compare the GPS station velocities to the sum of the plate motion and predictions for several models of viscoelastic relaxation, using the set of model parameters as indicated in each figure legend. Fig. 5 shows the LOS changes in each profile area as a function of time, compared to the different rheological models discussed above. Fig. 10 shows time series from selected GPS stations, after correcting for a constant velocity due to plate motion and poroelastic rebound. For comparison we show the displacements predicted by our preferred viscoelastic model (Model D). In summary, we find no evidence that a sum of two exponential functions is required to reproduce the postseismic signals in our GPS and InSAR data. Optimal parameters found for Models A and B indicate high viscosity for the lower crust which in turn implies a transient time over decades that is either not compatible with our observations, or below the detection threshold of our observations.

6. Co- and post-seismic static Coulomb failure stress change

To examine possible influence of viscoelastic relaxation in stress triggering of the 2008 May earthquakes, we calculate static Coulomb stress changes in the SISZ during 2000–2008 from Model D. The change in the static Coulomb failure stress change (ΔCFS) is estimated from (e.g., Harris, 1998):

$$\Delta CFS = \Delta\tau_s + \mu_f(\Delta\sigma_n - \frac{B}{3}\Delta\sigma_{kk}), \tag{1}$$

with $\Delta\sigma_{kk}$ is the change in volumetric stress, $\Delta\sigma_n$ and $\Delta\tau_s$ are, respectively, the changes in normal and shear stress on to the receiver faults (here we assume they are N–S right lateral strike slip faults). We use a coefficient of friction of μ_f=0.75 and the Skempton's coefficient B=0.5.

We calculate ΔCFS at 5 km depth (Fig. 11) and in a cross-section over the fault planes of the two 2008 May events (Fig. 12) using fault plane locations from (Decriem et al., 2010). Estimates of the coseismic ΔCFS (Fig. 11A) show positive stress changes at 5 km depth in the area west of the 2000 June faults where the 2008 May events occurred, in agreement with previous studies (Árnadóttir et al., 2003). We also calculate the contribution to the ΔCFS from the viscoelastic relaxation during 2000–2008 (Fig. 11B) from the preferred rheological model estimated in the previous section (Model D). Our calculations show that the viscoelastic model predicts positive stress changes in the whole SISZ, with the highest values in between the two 2000 June faults. Thus, we find a slight stress increase on the 2008 May faults due to postseismic relaxation, albeit an order of magnitude smaller (0.02–0.04 MPa) than the coseismic stress changes (0.25–0.5 MPa).

7. Discussion

7.1. Viscoelastic rheology: Maxwell, SLS, or Burgers body

The choice of rheology to describe stress relaxation in the lower crust and upper mantle is non trivial. Basic representation of the viscoelastic behaviour of the Earth is often insufficient using the most commonly used linear rheologies, e.g., the Maxwell element (spring and viscous dashpot connected in series, Fig. 6) does not fully describe delayed elasticity, and the Kelvin element (spring and viscous dashpot in parallel) can not account for stress relaxation. The standard linear solid (SLS) is the simplest element that can predict both phenomena. A Burgers body is a more detailed model for creep and relaxation (Fig. 6). This last model is a superposition of three effects: the instantaneous elastic response, an exponentially decaying transient response (Kelvin element), and a linearly increasing steady-state response controlled by the Maxwell element (Pollitz, 2003). Furthermore, it is not evident which of these models best represent the lower crust and the upper mantle. Results from postseismic studies are not always consistent, even for same area. Many studies have applied Maxwell rheology to explain surface deformation (Freed and Lin, 2001; Pollitz et al., 2001; Johnson and Segall, 2004; Jónsson, 2008; Árnadóttir et al., 2009), while others prefer SLS (Cohen, 1982; Pollitz et al., 2000; Ryder et al., 2007; Wang et al., 2009), or Burgers body (Pollitz, 2003, 2005; Árnadóttir et al., 2005).

However, it is important to note that the more complex linear models can be equivalent to the simpler models, if the parameters are appropriately selected. For example, the Burgers body rheology can be reduced to SLS or Maxwell, and an SLS element can describe Maxwell material. Comparison of postseismic surface displacements following a strike slip earthquake using analytical expressions for the the different linear rheologies (Maxwell, SLS and Burgers body) has

been conducted by Hetland and Hager (2005). In their study, Hetland and Hager (2005) suggest that a Burgers body and SLS elements give similar results at the beginning of the transient if the viscosities for the Burgers body are selected such that $\eta_2 \leq \eta_1/10$ (Fig. 6). The initial relaxation of the Burger body approximates that of a Maxwell element if $\eta_2 \gg \eta_1$.

Previous studies of the year scale postseismic relaxation following the 2000 June earthquakes were done by Árnadóttir et al. (2005), and Jónsson (2008). Árnadóttir et al. (2005) compared afterslip and viscoleastic models to explain GPS velocities from 2000–2001 and 2001–2004. Although both models can explain the data, they suggested that viscoelastic relaxation is a more reasonable model to explain the deformation after the first year. Their Earth model has a 12 km thick elastic plate, Maxwell rheology in the lower crust (12–20 km depth) and a Burgers body rheology below 20 km (upper mantle). They assume a transient mantle viscosity scaling $\eta_{UM2} = 0.036 \times \eta_{UM1}$ for the upper mantle, and suggest that the data were best fit by a model with viscosities of $\eta_{LC}=1\cdot10^{19}$ Pa s and $\eta_{UM1}=3\cdot10^{18}$ Pa s for the lower crust (LC) and upper mantle (UM), respectively. We will refer to this model as Arnadottir 2005A. They also consider a second model with $\eta_{LC}=5\cdot10^{18}$ Pa s and $\eta_{UM1}=5\cdot10^{19}$ Pa s, which we will refer to later on as Arnadottir 2005B. The model Arnadottir 2005A is dominated by the fast creep of the Kelvin element during the first years. It correspond to an effective viscosity $\eta_{sls} = 0.036 \times \eta_{UM1} = \eta_{UM2}=1\cdot10^{17}$ Pa s (τ_2=0.05 years). There is, however, no evidence of such rapid transient in the InSAR time series (Fig. 5). For the second model (Arnadottir 2005B) the Burgers body is equivalent to an SLS element for the upper mantle with $\eta_{sls} = 0.036 \times \eta_{UM1}$ $=\eta_{UM2}=1.8\cdot10^{18}$ Pa s and $\alpha = \frac{\mu_1\mu_2}{\mu_1+\mu_2} = 0.5$ as $\mu_1=\mu_2$ (Árnadóttir et al., 2005). The corresponding relaxation would then occur within 3–5 years, in better agreement with our observations than the model Arnadottir 2005A.

Jónsson (2008) extended the study by Árnadóttir et al. (2005) by adding InSAR data for the 5 years after the 2000 June earthquakes. He also suggests viscoelastic relaxation as the more likely mechanism to explain the deformation. Rather than a Burgers body rheology, his preferred model has three layers, with Maxwell rheology and viscosities of $2\cdot10^{19}$ Pa s from 10 to 15 km, $1\cdot10^{18}$ Pa s from 15 to 20 km and $3\cdot10^{18}$ Pa s below 20 km depth. The intermediate thin layer, relaxing faster, suggests that small creep occurs at the beginning of the transient, and a more appropriate model would be a single element with SLS rheology using a low α, such as our preferred model (Model D).

We use the software VISCO1D (Pollitz, 2005) to recalculate the models proposed by Árnadóttir et al. (2005) and Jónsson (2008), and extend the model calculation to 2008 (Figs. 5 and 10). All these models appear to predict velocities that are faster than the observed GPS velocities during 2004–2008.

In our study neither the GPS nor the InSAR data seem to indicate that more than one exponential function decay is needed to fit the observations. In our models with a viscoelastic lower crust (A and B) we found that high viscosities (i.e., $\eta > 1\cdot10^{19}$ Pa s) are favoured to reproduce the observations. Such high viscosities predict low rates for the 2004–2008 time interval, but result in large total displacement and a long relaxation time (more than 30 years). If we assume SLS rheology for the lower crust (Model B), the relaxation coefficient required to improve the fit to the data is very high (>0.66). Such high α predicts small displacements in the first years following the earthquake. In both cases (high viscosities or low viscosities with high α) the slower rates provide a better match to the observed rates during the 2004–2008 time interval. We argue that this is a strong indication that the viscoelastic relaxation from the lower crust has probably been over-estimated due to the shorter time span of the data (2000–2005) in the previous studies. We

9

can rule out Model A, as the large displacements predicted by this model for the 2004–2008 time interval are not detected at stations close to the plate boundary (ONDV, KIDJ, HAAL, KALT, LYTI, HEND, FLAG), nor do we observe large LOS displacements in the InSAR time series.

We found better agreement between the viscoelastic model predictions and our data using a thick elastic layer (~15km) over a half-space with SLS rheology (Model D). Stiff lower crust was also suggested from models of glacial isostatic adjustment in Iceland (Árnadóttir et al., 2009). They argue for viscosities around $1·10^{20}$ Pa s from 10 to 40 km and $1·10^{19}$ Pa s below assuming Maxwell rheology, to fit vertical velocities from two country wide GPS campaigns (1993–2004).

Previous studies in Iceland indicate that the mantle viscosity is better resolved than the viscosity of the lower crust. The mantle viscosity estimates, however, range over at least one order of magnitude between postseismic (Árnadóttir et al., 2005; Jónsson, 2008) and glacial isostatic adjustment (Pagli et al., 2007; Árnadóttir et al., 2009) studies. This difference may be due to the nature of the driving mechanism. In the case of postseismic relaxation, high coseismic stress changes occur quickly, very localised at a well known time. On the other hand, load changes due to glacial rebound cause small stress changes over long time periods, that may extend deep into the mantle, depending on the load size. Our ability to resolve viscosity structure at depth also depends on the location and the time span of the observations. In the postseismic case, our GPS dataset includes three time periods following the 2000 June earthquakes, with rapid decay in the deformation rates during the first 5 years. In the case of glacial rebound, the ice history used by Árnadóttir et al. (2009) covers more than a century, and the GPS velocities are averaged over 11 years. Such smoothing may not be appropriate to resolve processes at shallow depth, but may be used to resolve higher viscosities at greater depth. The discrepancy in the mantle viscosity estimated in postseismic and glacial isostatic adjustment studies, is therefore most likely the result of the resolution capability due to the nature of each process. Postseismic viscoelastic relaxation is suitable to estimate rheology at shallow depth whereas glacial isostatic adjustment can give an average value for a larger volume of the mantle. Our best model (Model D) with a half-space viscosity of $1\text{-}3·10^{18}$ Pa s is, however, consistent with estimates of upper mantle viscosities in previous postseismic studies.

7.2. Coulomb Failure Stress

Coseismic Coulomb stress changes at 5 km depth (Fig. 11) are positive, indicating loading of the faults that ruptured in 2008 May around 63.95°N latitude. It is interesting to note that recorded aftershocks do not extend further north than 64.05°N over the Kross and Ingólfsfjall fault planes, where negative static Coulomb stress changes due to the June 2000 events are predicted. Further investigation of the 2008 May postseismic deformation and aftershock sequences is a subject of a separate study. Here, we estimate the loading on the 2008 May faults by postseismic viscoelastic relaxation. The stress changes (ΔCFS) we estimate on the 2008 May faults shown in Fig. 12. We find stress relaxation below 15 km depth in the viscoelastic part according to our Model D. This relaxation leads to positive loading of the elastic part from a depth of 15 km up to the surface, with the largest changes predicted between 10 and 15 km depth (0.05 MPa). The stress increase occurs mainly below the area with the maximum slip in models for the 2008 May events estimated by Decriem et al. (2010). The maximum postseismic stress changes are, however, about one order of magnitude smaller than the coseismic stress changes. The viscoelastic relaxation contribution to the triggering of the 2008 May earthquakes therefore appears to be small, and may not entirely explain the delay between the two earthquake sequences.

8. Conclusions

We present an extensive study of the postseismic deformation transient following the 2000 June earthquakes in the SISZ, extending the GPS dataset to 2008. From our analysis we conclude that no significant transient deformation was observed after 2005.

We explore a wide range of viscoelastic models including both Maxwell and standard linear solid (SLS) rheologies to reproduce the surface velocities. Our preferred model has a thick elastic plate ($\sim$15 km) and a mantle that we model using a SLS rheology, with a viscosity of $\eta =$1-3$\cdot10^{18}$ Pa s and a relaxation coefficient $\alpha = 0.1 - 0.25$. Our study indicates that the viscoelastic contribution of the lower crust is very small, due to either almost elastic behaviour or very long relaxation time, below the detection threshold of our observations. Therefore, the effect of relaxation in the lower crust may have been over-estimated in previous SISZ postseismic studies.

Finally, Coulomb stress change calculations indicate that the contribution of viscoelastic relaxation to the loading of faults that ruptured in the 2008 May earthquake doublet is very small (less than 0.05 MPa) compared to the coseismic stress changes (0.5–1 MPa).

9. Acknowledgments

References

Altamimi, Z., Collilieux, X., Legrand, J., Garayt, B., Boucher, C., 2007. ITRF2005: A new release of the International Terrestrial Reference Frame based on time series of station positions and Earth Orientation Parameters. J. Geophys. Res. 112, B09401, doi:10.1029/2007JB004949.

Árnadóttir, T., Hreinsdóttir, S., Gudmundsson, G., Einarsson, P., Heinert, M., Völksen, C., 2001. Crustal deformation measured by GPS in the South Iceland Seismic Zone due to two large earthquakes in June 2000. Geophys. Res. Lett. 28, 4031–4033.

Árnadóttir, T., Jiang, W., Feigl, K. L., Geirsson, H., Sturkell, E., 2006. Kinematic models of plate boundary deformation in southwest Iceland derived from GPS observations. J. Geophys. Res. 111, B07402, doi: 10.1029/2005JB003907.

Árnadóttir, T., Jónsson, S., Pedersen, R., Gudmundsson, G. B., 2003. Coulomb stress changes in the South Iceland Seismic Zone due to two large earthquakes in June 2000. Geophys. Res. Lett. 30(5), 1205, doi: 10.1029/2002GL016495.

Árnadóttir, T., Jónsson, S., Pollitz, F. F., Jiang, W., Feigl, K. L., 2005. Postseismic deformation following the June 2000 earthquake sequence in the south Iceland seismic zone. J. Geophys. Res. 110, B12308, doi: 10.1029/2005JB003701.

Árnadóttir, T., Lund, B., Jiang, W., Geirsson, H., Björnsson, H., , Einarsson, P., Sigurdsson, T., 2009. Glacial rebound and plate spreading: results from the first countrywide GPS observations in Iceland. Geophys. J. Int. 177(2), 691–716.

Clifton, A. E., Einarsson, P., 2005. Styles of surface rupture analysis accompanying the June 17 and 21, 2000 earthquakes in the South Iceland Seismic Zone. Tectonophysics 396, 141–159.

Cohen, S. C., Jul. 1982. A multilayer model of time dependent deformation following an earthquake on a strike slip fault. J. Geophys. Res. 87, 5409–5421.

Dach, R., Hugentobler, U., Fridez, P., Meindl, M., 2007. Bernese GPS software version 5.0. Tech. rep., Astronomical Institure, University of Bern, Bern, Switzerland.

Decriem, J., Árnadóttir, T., Hooper, A., Geirsson, H., Sigmundsson, F., Keiding, M., Ófeigsson, B. G., Hreinsdóttir, S., Einarsson, P., LaFemina, P. C., Bennett, R., 2010. The 2008 May 29 earthquake doublet in SW Iceland. Geophys. J. Int. 181, 1128–1146.

DeMets, C. G., Gordon, R., Argus, D. F., Stein, S., 1994. Effect of recent revisions to the geomagnetic reversal time scale on estimates of current plate motions. Geophys. Res. Lett. 21, 2191–2194.

Deng, J., Gurnis, M., Kanamori, H., Hauksson, E., 1998. Viscoelastic flow in the lower crust after the 1992 Landers, California, earthquake. Science 282, 1689–1692.

Einarsson, P., 2008. Plate boundaries, rifts and transforms in Iceland. Jökull 58, 35–38.

Freed, A., Bürgman, R., 2004. Evidence of powerlaw flow in the Mojave desert mantle. Nature 430, 548–551.

Freed, A., Bürgman, R., Calais, E., Freymueller, J., Hreinsdottir, S., 2006. Implications of deformation following the 2002 Denali, Alaska, earthquake for postseismic relaxation processes and lithospheric rheology. J. Geophys. Res. 111, doi:10.1029/2005JB003894.

Freed, A. M., Lin, J., 2001. Delayed triggering of the 1999 Hector Mine earthquake by viscoelastic stress transfer. Nature 411, 180–183.

Harris, R. A., 1998. Introduction to special section: Stress triggers, stress shadows, and implications for seismic hazard. J. Geophys. Res. 103, 24,347–24,358.

Heki, K., Miyazaki, S., Tsuji, H., 1997. Silent fault slip following an interplate thrust earthquake at the Japan trench. Nature 386, 595–598.

Herring, T. A., King, R. W., McClusky, S. C., 2006. GLOBK reference manual, Global Kalman filter VLBI and GPS analysis program, release 10.3. Tech. rep., Mass. Inst. Technol., Cambridge, MA, USA.

Hetland, E. A., Hager, B. H., oct 2005. Postseismic and interseismic displacements near a strike-slip fault: A two-dimensional theory for general linear viscoelastic rheologies. J. Geophys. Res. 110 (B9), 10401.

Hjaltadóttir, S., 2009. Use of relatively located microearthquakes to map fault patterns and estimate the thickness of the brittle crust in Soutwest Iceland. Master's thesis, Faculty of Earth Sciences, University of Iceland, Reykjavík, Iceland.

Hreinsdóttir, S., Árnadóttir, T., Decriem, J., Geirsson, H., Tryggvason, A., Bennett, R. A., LaFemina, P., 2009. A complex earthquake sequence captured by the continuous GPS network in SW Iceland. Geophys. Res. Lett. 36, L12309.

Johnson, K. M., Segall, P., Oct. 2004. Viscoelastic earthquake cycle models with deep stress-driven creep along the San Andreas fault system. J. Geophys. Res. 109 (B18), 10403.

Jónsson, S., 2008. Importance of post-seismic viscous relaxation in southern Iceland. Nature Geoscience 1, 136–139.

Jónsson, S., Segall, P., Pedersen, R., Björnsson, G., 2003. Post-earthquake ground movements correlated to pore-pressure transients. Nature 424, 179–183.

Keiding, M., Árnadóttir, T., Jónsson, S., Decriem, J., Hooper, A., 2010. Plate boundary deformation and man-made subsidence around geothermal fields on the Reykjanes Peninsula, Iceland. Journal of Volcanology and Geothermal Research 194, 139–149.

LaFemina, P. C., Dixon, T. H., Malservisi, R., Árnadóttir, T., Sturkell, E., Sigmundsson, F., Einarsson, P., 2005. Geodetic GPS measurements in south Iceland: Strain accumulation and partitioning in a propagating ridge system. J. Geophys. Res. 110, B11405, doi: 10.1029/2005JB003675.

Langbein, J., Murray, J., Snyder, H., 2006. Coseismic and initial postseismic deformation from the 2004 Parkfield, California, earthquake, observed by Global Positioning System, electronic distance meter, creepmeters, and borehole strainmeters. Bull. Seismol. Soc. Am. 96, 304–320.

Masterlark, T., Hughes, K., 2008. The next generation of deformation models for the 2004 M9 Sumatra-Andaman Earthquake. Geophys. Res. Lett. 35.

McClusky, S., et al., 2000. Global Positioning System constraints on plate kinematics and dynamics in the eastern Mediterranean and Caucasus. J. Geophys. Res. 105(B3), 5695–5720.

Melbourne, T., Webb, F., Stock, J., Reigber, C., 2002. Rapid postseismic transients in subduction zones from continuous GPS. J. Geophys. Res. 107, 2241.

Pagli, C., Sigmundsson, F., Pedersen, R., Einarsson, P., Árnadóttir, T., Feigl, K. L., 2007. Crustal deformation associated with the 1996 Gjálp subglacial eruption, Iceland: InSAR studies in affected areas adjacent to the Vatnajökull ice cap. Earth Planet. Sci. Lett. 259, 24–33.

Pedersen, R., Jónsson, S., Árnadóttir, T., Sigmundsson, F., Feigl, K. L., 2003. Fault slip distribution of two M_w=6.5 earthquakes in South Iceland estimated from joint inversion of InSAR and GPS measurements. Earth Planet. Sci. Lett. 213, 487–502.

Pedersen, R., Sigmundsson, F., Feigl, K. L., Árnadóttir, T., 2001. Coseismic interferograms of two M_s=6.6 earthquakes in the South Iceland Seismic Zone, June 2000. Geophys. Res. Lett. 28, 3341–3344.

Peltzer, G., Rosen, P., Rogez, F., Hudnut, K., 1998. Poro-elastic rebound along the Landers 1992 earthquake surface rupture. J. Geophys. Res. 103, 30131–30145.

Pollitz, F., Banerjee, P., Grijalva, K., Nagarajan, B., Brgmann, R., 2008. Effect of 3-d viscoelastic structure on postseismic relaxation from the 2004 m= 9.2 Sumatra earthquake. Geophys. J. Int. 173, 189–204.

Pollitz, F. F., 2003. Transient rheology of the uppermost mantle beneath the Mojave Desert, California. Earth Planet. Sci.

Lett. 215, 89–104.

Pollitz, F. F., 2005. Transient rheology of the upper mantle beneath central Alaska inferred from the crustal velocity field following the 2002 Denali earthquake. J. Geophys. Res., doi:10.1029/2005JB003676.

Pollitz, F. F., Wicks, C., Thatcher, W., 2000. Mobility of continental mantle: Evidence from postseismic geodetic observations following the 1992 Landers earthquake. J. Geophys. Res. 105, 8035–8054.

Pollitz, F. F., Wicks, C., Thatcher, W., 2001. Mantle flow beneath a continental strike-slip fault: Postseismic deformation after the 1999 Hector Mine earthquake. Science 293, 1814–1818.

Pritchard, M., Simons, M., 2006. An aseismic pulse in nothern Chile and along-strike variations in seismogenic behavior. J. Geophys. Res. 111, 30131–30145.

Ryder, I., Parsons, B., Wright, T., Funning, G., 2007. Post-seismic motion following the 1997 Manyi (Tibet) earthquake: InSAR observations and modelling. Geophys. J. Int. 169, 1009–1027.

Stefánsson, R., Bödvarsson, R., Slunga, R., Einarsson, P., Jakobsdóttir, S., Bungum, H., Gregersen, S., Havskov, J., Hjelme, J., Korhonen, H., 1993. Earthquake Prediction Research in the South Iceland Seismic Zone and the SIL Project. Bull. Seismol. Soc. Am. 83 (3), 696–716.

Wang, L., Wang, R., Roth, F., Enescu, B., Hainzl, S., Ergintav, S., 2009. Afterslip and viscoelastic relaxation following the 1999 M7.4 İzmit earthquake from GPS measurements. Geophys. J. Int. 178, 1220–1237.

Wessel, P., Smith, W., 1998. New, improved version of generic mapping tools released. EOS Trans. American Geophys. Union 79, 579.
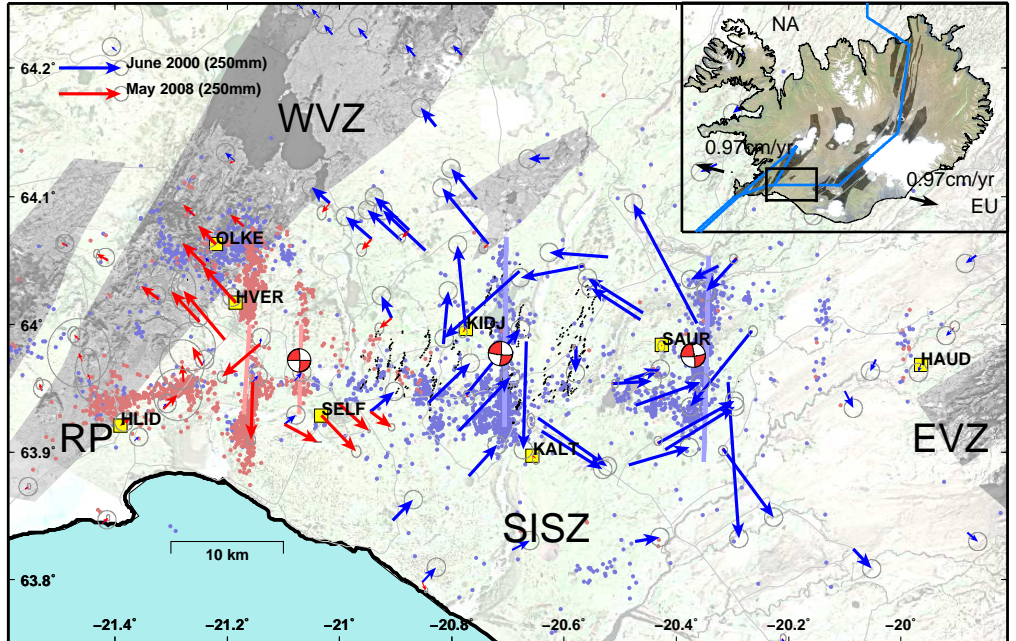
Figure 1: Tectonic setting of South Iceland Seismic Zone (SISZ) and coseismic offsets estimated from GPS measurement due to the June 2000 (blue arrows) and the May 2008 (red arrows) events (Árnadóttir et al., 2006; Decriem et al., 2010). The error ellipses denote 95% uncertainties off the coseismic offsets. The SISZ is an E–W transform zone that joins the Reykjanes Peninsula and the Western Volcanic Zone (WVZ), to the west, and the Eastern Volcanic Zone (EVZ) to the east. Volcanic fissure swarms are shown in dark grey. The dots are earthquakes recorded by the SIL seismic network during 2000 (blue) and 2008 (red). The fault planes estimated from inversion of geodetic data are indicated with thick N–S lines (Pedersen et al., 2003; Decriem et al., 2010). The focal mechanisms are from the USGS. Yellow squares show the locations of continuous GPS stations in the study area. The inset shows the plate boundary across Iceland, and the location of the study area with a rectangle. The black arrows show the plate spreading according to the NUVEL-1A plate motion model (DeMets et al., 1994).

14
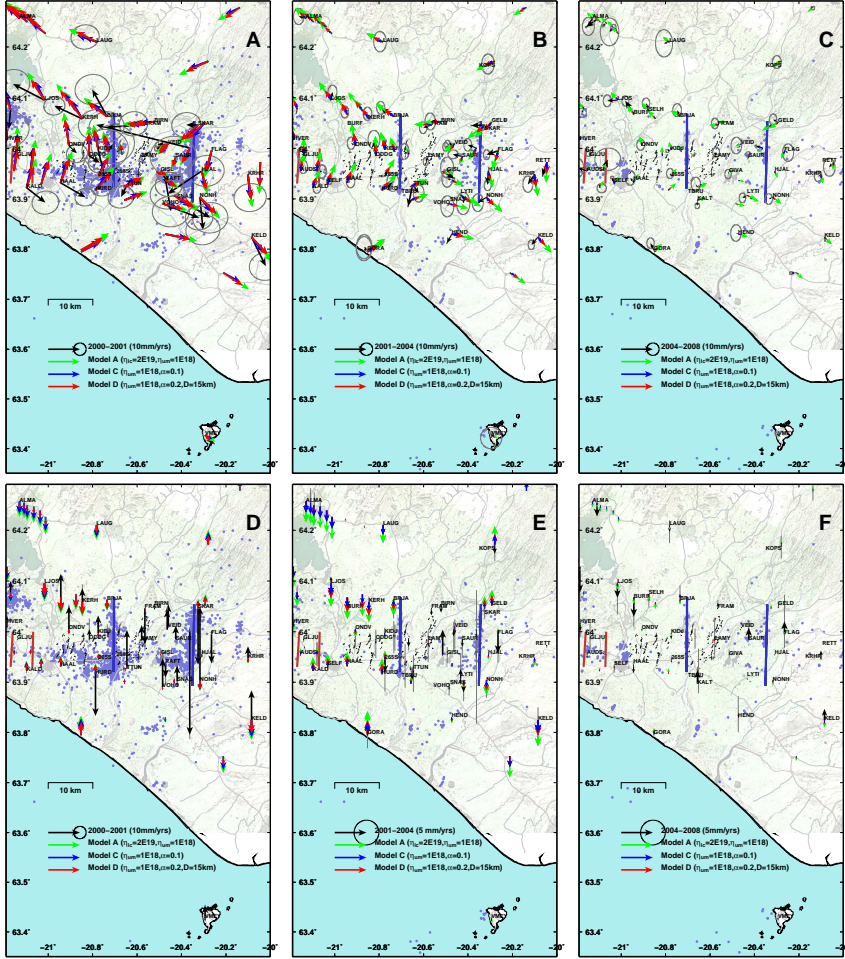
Figure 2: GPS velocities for 2000–2001, 2001–2004, and 2004–2008 (black arrows with 95% confidence ellipses). Panels A, B and C show horizontal velocities, and panels D, E and F vertical. The 2000–2001 velocities are corrected for poroelastic relaxation as explained in the text. The dots show earthquakes for the given time period. The two vertical blue lines show the location of the 2000 June 17 and 21 faults. The coloured arrows show the optimal fit viscoelstic models for rheology used in Models A, C, and D.
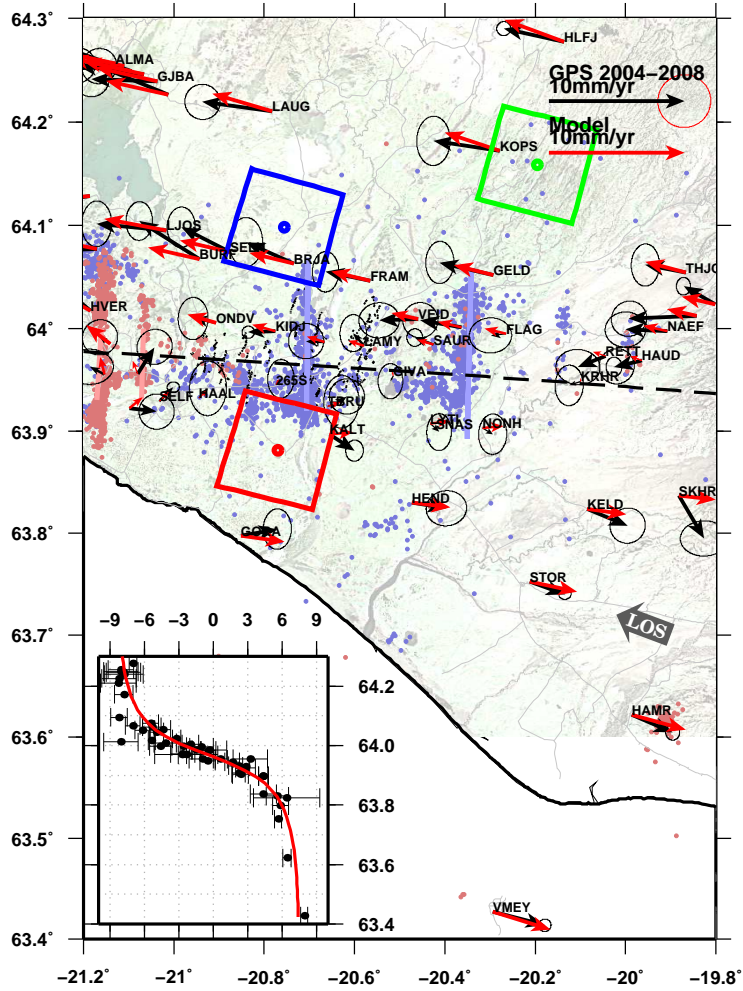
Figure 3: GPS velocities for 2004–2008 (black arrows with 95% error ellipses) and predicted velocities from a dislocation model of the plate boundary (red arrows). The blue dots show earthquakes occurring from 2000 June 21 to 2008 January 1. The two thick blue lines show the locations of the 2000 June 17 and 21 fault models (Pedersen et al., 2003), and the red lines indicate the faults that ruptured in May 2008 (Decriem et al., 2010). The thick dashed line is the estimated location of the SISZ transform. The inset shows the east component of the GPS velocities (i.e., the motion parallel to the plate boundary), as a function of latitude. The plate model prediction is shown with a red curve. The colored squares show the locations of the three InSAR profiles derived by Jónsson (2008) and the dark grey arrow with LOS label show the descending radar look direction.
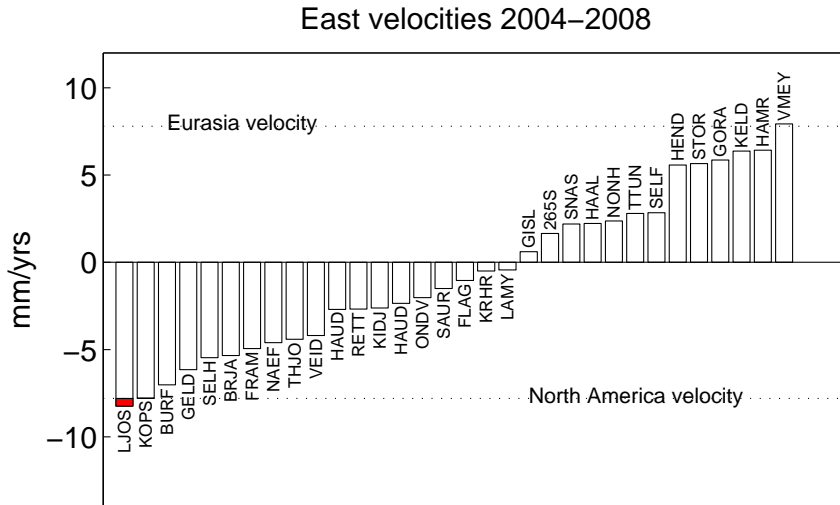
16
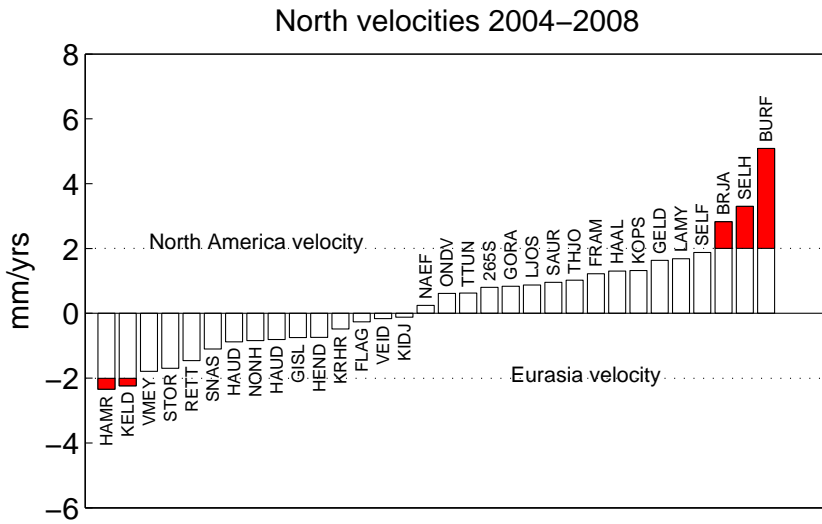
Figure 4: Histogram of the east and north component of the GPS station velocities for 2004–2008 sorted by amplitude. The dashed lines show the plate velocities according to the NUVEL-1A plate motion model (DeMets et al., 1994), and the red portion of the bar indicates the part of the velocity that exceeds the NUVEL-1A model.
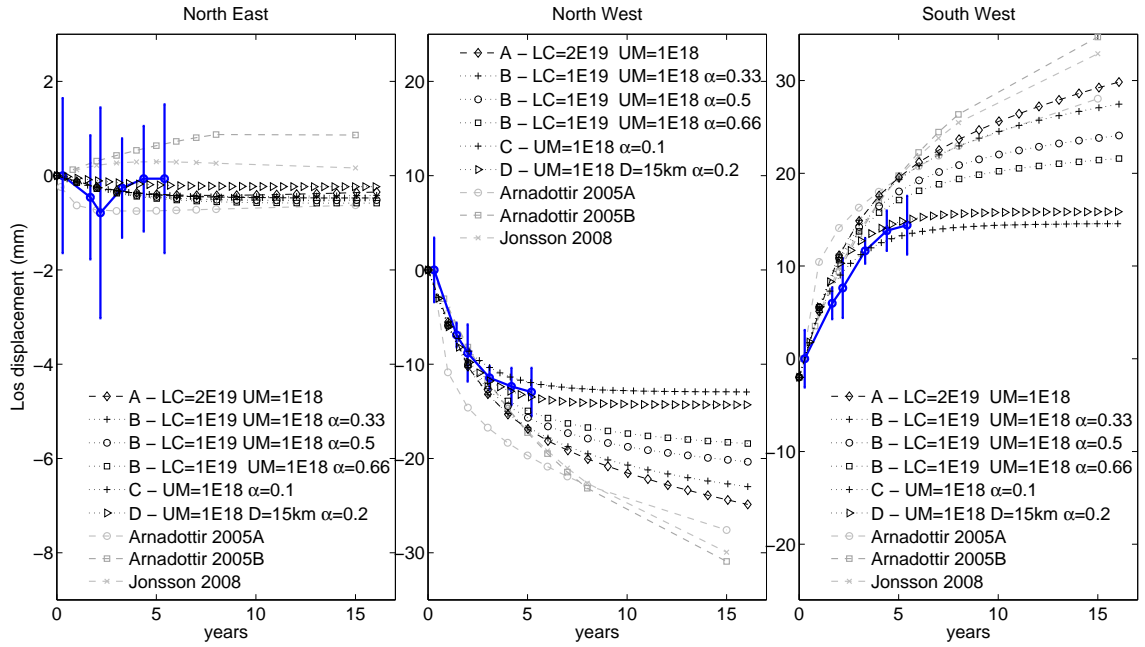
Figure 5: InSAR line-of-sight (LOS) displacements (thick black lines) for the 2000–2005 time period in the three areas outlined by the coloured boxes in Fig. 3. Predicted LOS displacements for the rheological parameters in Models A, B, C and D that best fit the combined data are shown with dashed lines and symbols. Model predictions based on prior studies (Árnadóttir et al., 2005; Jónsson, 2008) are also plotted. Here, negative LOS displacements correspond to subsidence.
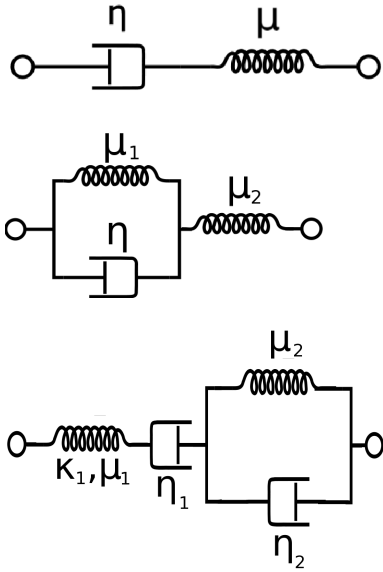
18

Figure 6: Mechanical analog models (springs and viscous dashpots) used to describe Maxwell (top) SLS (center) and Burgers body rheology (bottom). We use the software code PSGRN/PSCMP (Wang et al., 2009) to calculate the SLS rheology, where μ_2 is unrelaxed shear modulus. The relaxed shear modulus is $\frac{\mu_1\mu_2}{\mu_1+\mu_2}$, also written as $\alpha\mu_2$, where $0 \leq \alpha \leq 1$ is the relaxation strength of the SLS body. When $\alpha = 1$ this corresponds to perfect elasticity and if $\alpha = 0$ the SLS rheology reduces to a Maxwell rheology. The Burgers body description has a steady state shear and bulk moduli μ_1 and κ_1, respectively, steady state viscosity η_1, transient viscosity η_2 and a transient shear modulus μ_2 (Pollitz, 2003). If $\eta_2 = \infty$ or $\mu_2 = \infty$ the Burgers body is equivalent to a Maxwell rheology. If $\eta_1 = \infty$ the material behavior reduces to SLS rheology.
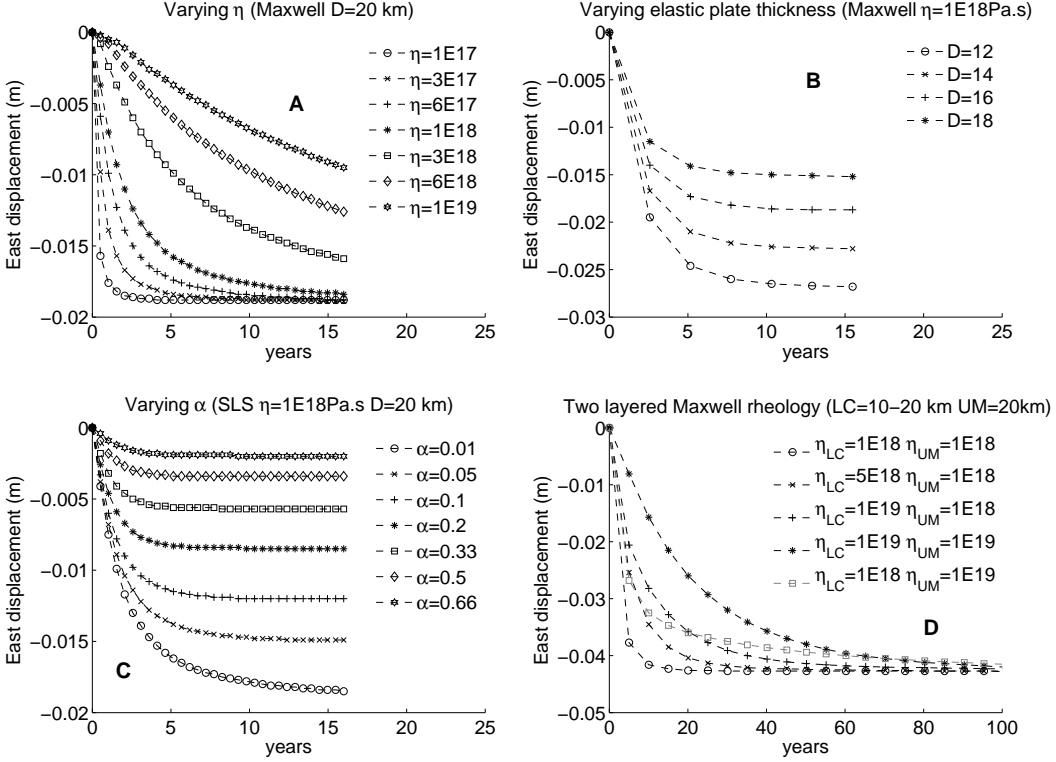
Figure 7: Surface deformation predicted by viscoelastic models, when varying the rheological model parameters. The source function is a vertical N–S right-lateral strike slip fault, with 1 m of coseismic slip from the surface down to 10 km. (A) Model with Maxwell rheology below 20 km depth, and varying viscosity (η). (B) Model with Maxwell rheology with $\eta = 1\cdot10^{18}$ Pa s below depth D. (C) Model with SLS rheology below 20 km depth, with $\eta = 1\cdot10^{18}$ Pa s, and varying α. (D) Model with Maxwell rheology in the lower crust (η_{LC}, depth 10-20 km), and Maxwell rheology in the upper mantle (η_{UM}, below 20 km depth).
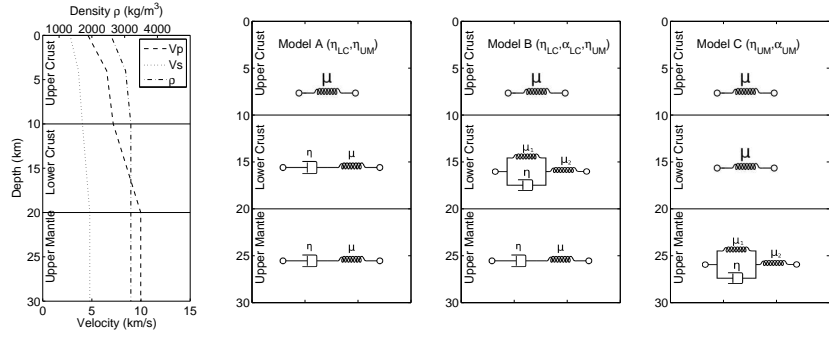
Figure 8: Seismic velocities and density of the crust with depth (left) and rheology of the viscoelastic models. Model A has a Maxwell rheology in the lower crust and upper mantle. Model B has SLS rheology in the lower crust and a Maxwell mantle. Model C has a thick elastic crust and SLS mantle.
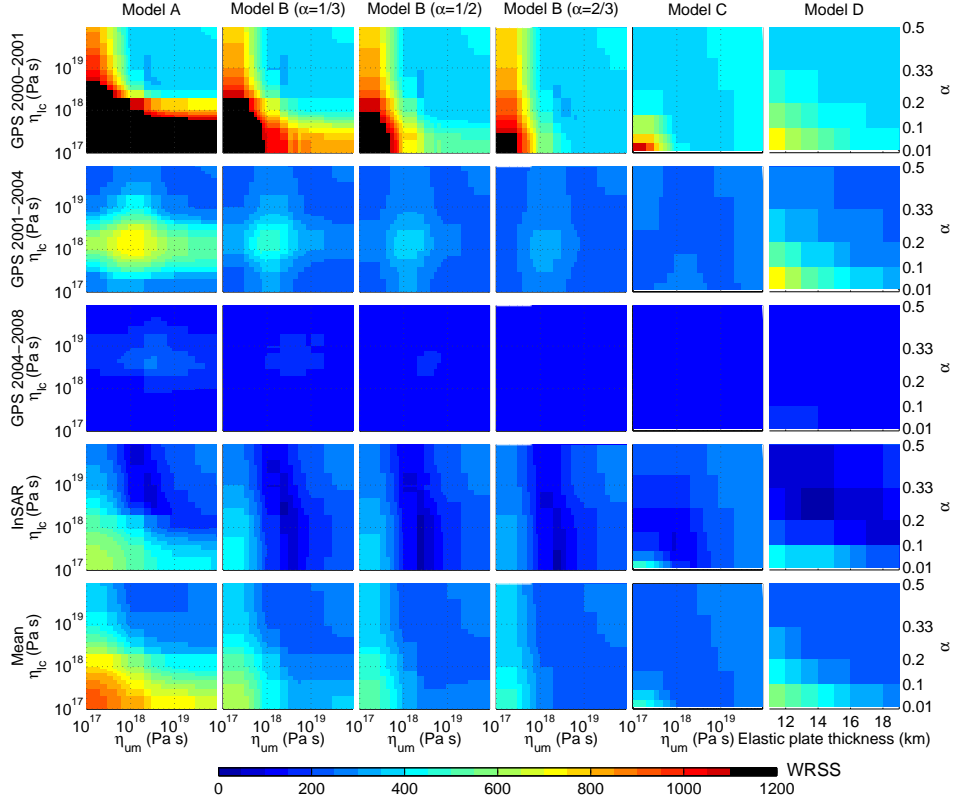
Figure 9: Misfit (WRSS) for each dataset (rows) for the different rheological models we tested (columns). The bottom row shows the mean of the WRSS for the individuals datasets. The rheological models are explained in Fig. 8. Model B is calculated assuming three different values of α, as indicated for each column. The horizontal and vertical axis in each subplot represent the upper mantle and lower crust viscosities, respectively, except for Models C and D where the vertical axis shows the SLS relaxation coefficient α of the upper mantle. We tested models with viscosities ranging from $1 \cdot 10^{17}$ Pa s to $1 \cdot 10^{20}$ Pa s. The dashed lines indicate $1 \cdot 10^{18}$ Pa s and $1 \cdot 10^{19}$ Pa s.
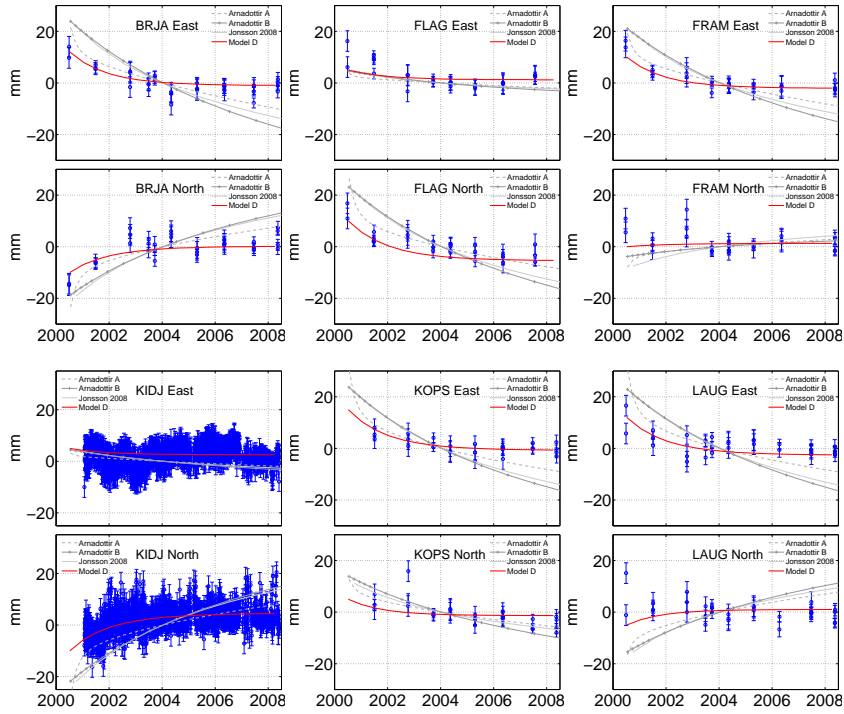
Figure 10: Time series showing displacements as a function of time at selected GPS stations (blue dots with 1σ error bars), and motion predicted by the preferred viscoelastic Model D (red line) as well as models from previous studies (grey lines), same as in Fig. 5. The station displacements have been corrected for constant plate motion and poro-elastic relaxation.
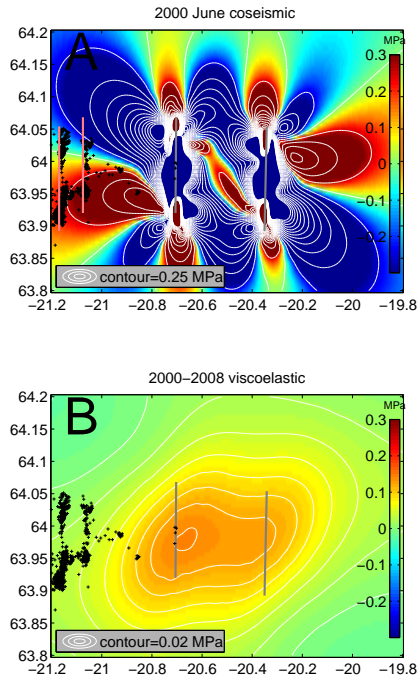
23

Figure 11: Static Coulomb failure stress change (ΔCFS) on N–S right-lateral strike slip faults at 5 km depth following the 2000 June main shocks using our preferred viscoelastic model. This model (Model D) has a 15 km thick elastic plate and a half-space with SLS rheology (α=0.2, η=1·10^{18} Pa s). (A) Coseismic CFS change (contours are 0.25 MPa). Warm colours indicate a stress increase. (B) Viscoelastic CFS change (contours are 0.02 MPa). The thick grey and light red lines indicate the locations of the 2000 June and the 2008 May ruptures, respectively. The dots show earthquake locations from 2008 May 29 to 2010 January 01.
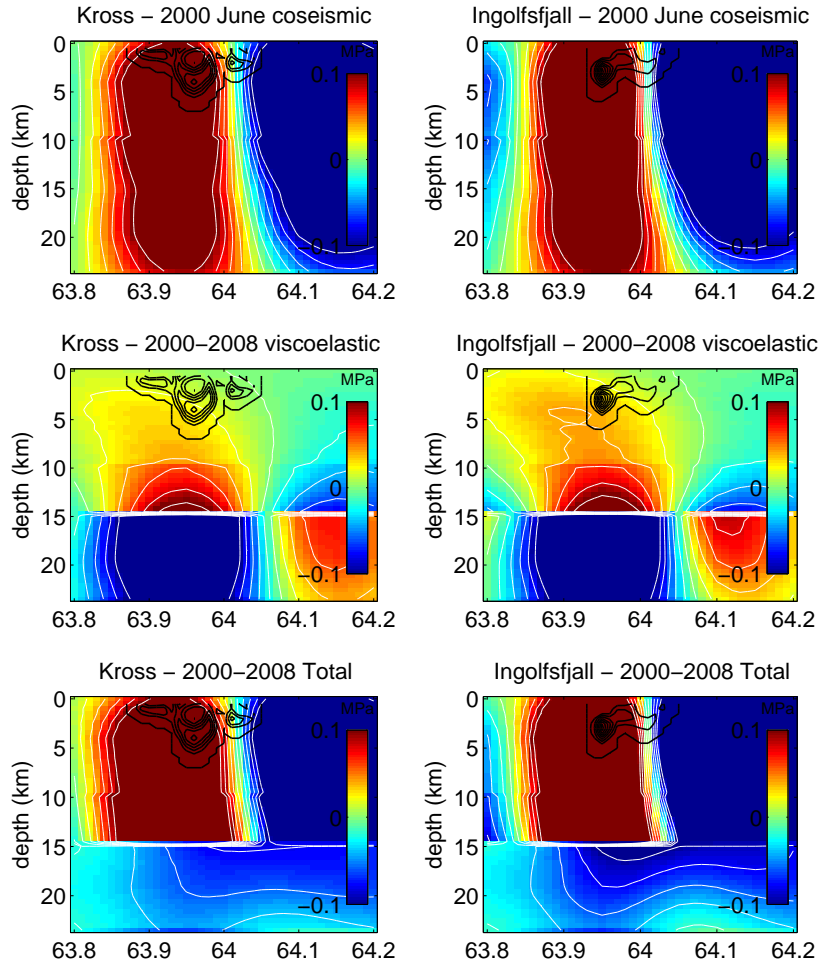
Figure 12: Coulomb failure stress changes on the 2008 May faults (the Kross fault and the Ingólfsfjall) fault). (Top) Coseismic static Coulomb failure stress changes due to the 2000 June mainshocks, (center) the stress changes caused by viscoelastic relaxation during 2000–2008, (bottom) stress changes due to the 2000 June main shocks and viscoelastic postseismic relaxation. The white contours are 0.05 MPa and the black contours indicate the slip distribution estimated from inversion of geodetic data (Decriem et al., 2010)

Decriem J., Árnadóttir Th., Hreinsdóttir S., Hooper A., Geirsson H., LaFemina P.C., and Bennett R.A., Postseismic relaxation following the May 2008 earthquakes South Iceland, *submitted to Geophysical Journal International, 2011.*

.

Postseismic relaxation following the May 2008 earthquakes South Iceland.

Draft: 20 March 2011

J. Decriem,[1] T. Árnadóttir,[1] S. Hreinsdóttir,[1] A. Hooper,[2] H. Geirsson, [3,4] P. LaFemina,[4] R. A. Bennett,[5]

[1] *Nordic Volcanological Center,Institute of Earth Sciences,University of Iceland,IS-101 Reykjavík, Iceland (judicael@hi.is)*

[2] *Dept. of Earth Observation and Space Systems, Delft University of Technology, Delft, Netherlands*

[3] *Division of Processing and Research, Icelandic Meteorological Office,Reykjavík, Iceland*

[4] *Dept. of Geosciences, Pennsylvania State University, University Park, Pennsylvania, USA*

[5] *Dept. of Geosciences, University of Arizona, Tucson, Arizona, USA*

SUMMARY

An earthquake sequence started in June 2000 (after 88 years of relative quiescence) in the South Iceland Seismic Zone (SISZ) with two Mw6.5 events occuring within 81 hours of each other. In May 2008, the western part of the SISZ was shaken by two M6 events located only ∼5 km apart and rupturing within a few seconds of each other (Hreinsdóttir et al., 2009). Transient surface deformation following the June 2000 events, visible from InSAR and GPS data were explained by poroelastic effects for the first months (Jónsson et al., 2003) and viscoelastic relaxation lasting for ∼5 years (Árnadóttir et al., 2005; Jónsson, 2008; Decriem & Árnadóttir, 2011). Here, we analyze GPS and InSAR data from the first year following the May 2008 earthquakes. We observe fast transients at continuous GPS stations close to the faults with about 30 mm of motion (∼15-20% of the coseismic

offsets) during the first two months. We test poroelastic, viscoelastic, and afterslip models to reproduce the surface deformation during the first year following the May 2008 events. Our preferred models involve viscoelastic relaxation and shallow afterslip to explain both the far field and near field displacements. We also identify a phase discontinuity in InSAR data covering the first week after the May 2008 events that coincides with an ENE-trending lineament of high aftershock activity. We suggest a pore pressure model with an impermeable structure may explain the correlation between the changes in water pressure, offset in InSAR data, and high seismicity along this ENE-trending lineament.

Key words: Viscoelastic relaxation; Poroelastic deformation; postseismic transient; South Iceland Seismic Zone; Satellite geodesy; Earthquake source observations; Seismicity and tectonics; Space geodetic surveys

1   INTRODUCTION

In May 2008 two M6 earthquakes struck the western part of the South Iceland Seismic Zone (Hreinsdóttir et al., 2009). The South Iceland Seismic Zone (SISZ) accommodates left-lateral shear due to plate spreading between the North American and Eurasian plates across South Iceland (Figure 1). Earthquakes in the SISZ release strain that builds up along this segment of the plate boundary (due to the spreading at a rate of ∼19 mm/yr), that connects the Reykjanes Peninsula to the west and Eastern Volcanic Zone to the east (DeMets et al., 1994). Instead of a single left lateral fault, the strain is released in moderate size earthquakes (M6-7) rupturing N-S right lateral strike slip faults (Einarsson, 2008; Clifton & Einarsson, 2005).

The latest sequence of large events in the SISZ started in 2000 when two M6.5 earthquakes occurred on June 17 and 21. Surface deformation observed by GPS and Interferometric Synthetic Aperture Radar (InSAR) was explained by up to 2.5 m of slip on two parallel, 10 km long N–S trending faults (Árnadóttir et al., 2001; Pedersen et al., 2001, 2003). A rapid post-seismic transient was captured by InSAR and has been explained with a poro-elastic model (Jónsson et al., 2003). A longer deformation transient (∼5 years) was recorded by annual GPS measurements and was more consistent with viscoelastic relaxation (Árnadóttir et al., 2005; Jónsson, 2008; Decriem & Árnadóttir, 2011).

From modeling of geodetic data Hreinsdóttir et al. (2009) and Decriem et al. (2010) described the 2008 May event as a doublet, where two N–S oriented faults (the Kross fault to the west and the Ingólfsfjall fault to the east), located only ∼5 km apart ruptured within a few seconds of each

other. A composite magnitude of $M_w 6.1$ for the doublet was estimated from geodetic data by Decriem et al. (2010). Earthquake activity in South Iceland has been recorded by the Icelandic seismic network (SIL) operated by the Icelandic Meteorological Office, since 1989 (Stefánsson et al., 1993). After-shocks were recorded by both the SIL network and a temporary seismic network (Jakobsdóttir et al., 2008; Brandsdóttir et al., 2011). The aftershocks delineate two N–S oriented faults, and a third E–W lineament located to the west of the main faults (Brandsdóttir et al., 2011).

Here we present GPS and Interferometric Synthetic Aperture Radar (InSAR) observations follow-ing the May 2008 earthquakes. We evaluate the surface deformation during the first year and examine whether pore pressure changes, viscoelastic relaxation and/or afterslip can explain the signals we ob-serve.

2 OBSERVATIONS

2.1 GPS observations

Annual campaign style GPS measurements have been conducted in the SISZ and on the Reykjanes Peninsula since June 2000 (Árnadóttir et al., 2006; Keiding et al., 2008). Campaign measurements were made at selected stations in the area in April and early May 2008, before the main shocks on May 29, and a denser network was resurveyed starting on the evening of May 29. We also maintained semi-continuous observations at 17 GPS campaign stations from early June until August 2008. The May 2008 coseismic GPS campaign data have been analyzed and modelled by Decriem et al. (2010). Here we use campaign and semi-continuous data collected in summer 2008 and May 2009 to study the postseismic deformation following the May 2008 earthquakes (Figure 2).

The GPS data analysis is performed in two steps. First we use the Bernese v5.0 software (Dach et al., 2007) to calculate daily solutions with orbit information and Earth rotation parameters from the International GPS Service (IGS) in the International Terrestrial Reference Frame (ITRF) 2005 (Altamimi et al., 2007). In the second step we follow a regional stabilization approach (McClusky et al., 2000), and combine the daily solution from Bernese v5.0 and global network solution using the GLOBK software (Herring et al., 2006).

The timeseries 3) show a rapid decaying trend at the beginning and a slower trend during the year following. We decided to split the measurment into two time period : a) from May to August 2008 and b) from August 2008 to May 2009 (Figure 2). We correct the August 2008 to May 2009 dataset from background motion using a secular plate motion model from Decriem & Árnadóttir (2011), and two contracting point sources in the Hengill area. The deformation we observe by GPS correlates with LOS changes observed by InSAR (Keiding et al., 2010) and is most likely due to extraction of geothermal

fluids at the Nesjavellir and Hellisheidi power plants (Figure 1). In the subsequent sections we will refer to this corrected data set as the postseismic deformation during August 2008 to May 2009.

We observe a fast transient shortly after the events (Figure 2 and 3). From May to August 2008 stations in the northwest quadrant move rapidly towards northwest. The continuous GPS (CGPS) stations HVER moves to the west and north at 23 mm and 16 mm, respectively, and OLKE about 12 mm and 4 mm, respectively. This represents 15-20 % of the coseismic offsets at these stations (Decriem et al., 2010). In the southeast quadrant, the motion of CGPS station SELF (4 mm to East and 6 mm to the South) also equals 15-20 % of the coseismic offsets. A large northward displacement (about 10 mm) was measured at campaign station GEIT where shallow earthquakes (depth < 2 km) up to M5 were recorded (Brandsdóttir et al., 2011). In the area between the main faults that ruptured on May 29, stations GLJU and AUDS show significant displacement toward southwest. Although the displacement fields for the May to August 2008 and the August 2008 to May 2009 periods are not identical, there are many similar features, with smaller magnitudes of displacements for the later (Figure 2).

2.2 InSAR

We process ENVISAT data from tracks T95, T138, T367 and T402 spanning 2006 to 2009 using the DORIS software (Kampes & Usai, 1999). Several interferograms span the time of the earthquakes. To the west of the events from -21.2 to -21.5 longitude and 63.9 latitude a sharp phase discontinuity seems to align with seismicity (Figure 4). This feature maps into all interferograms covering the first week following the events, independently from the track, observation geometry and master image. If atmospheric effect was the source of the signal it would be seen in other interferogram (such as T95 2008-06-02/2008-07-07 Fig 4). The location of the discontinuity does not correlate with topography and the signal is not seen in InSAR data after June 2008 (Figure 4). No surface fractures have been observed in this area, although a significant number of aftershocks were located there. The intereferograms do not indicate significant postseismic deformation other than the ENE oriented fringe.

3 MODELLING

3.1 Poroelastic relaxation

Elastic stress changes induced by an earthquake affects the pressure of the fluids in the crust. Following the event, fluids are driven from an area of high pressure toward an area of low pressure, according to Darcy's law. This pore pressure equilibration (poroelastic relaxation) has been suggested to explain

short term deformation following earthquakes, including the June 2000 earthquakes (e.g. Jónsson et al., 2003; Freed et al., 2006).

We compare the May - August 2008 deformation with models of poroelastic relaxation. To estimate the elastic deformation resulting from pore pressure equilibration we calculate the coseismic deformation using fault models from Decriem et al. (2010) under drained and undrained conditions following Jónsson et al. (2003). The undrained condition corresponds to the phase where the rate of elastic loading is greater than the rate at which pore water pressure may dissipate. The drained state corresponds to the deformation phase once the pore water is again in equilibrium. The elastic deformation resulting from the pore pressure dissipation is then given by the difference between the undrained and drained solutions. We assume a Poisson's ratio of 0.31 for the undrained conditions and 0.25 for the drained solution similar to Jónsson et al. (2003) for the June 2000 earthquakes. We estimate the goodness of fit with the weighted residual sum of squares (WRSS). For this model the WRSS = 450. The resulting displacements are shown in Figure 2A. The station displacements predicted by the poroelastic model are much smaller and in most cases in the opposite sense to what we observe in the epicentral region.

3.2 Viscoelastic relaxation

Earthquakes change stresses in the brittle crust instantaneously, and with time these stress changes are transferred trough the ductile part of the lower curst and upper mantle by viscoelastic relaxation. Viscoelastic flow in the lower crust and upper mantle has been used to explain the broad (10-100 km) long term deformation signal after moderate to large earthquakes (e.g. Wang et al., 2009; Masterlark & Hughes, 2008).

We use the PGRN/PSCMP software to calculate the surface displacements (Wang et al., 2009). We apply a rheological model that best fits 8 years of postseismic deformation observed by GPS, following the June 2000 main shocks in the SISZ (Decriem & Árnadóttir, 2011). The model consists of a 15 km thick elastic plate and an standard linear solid (SLS) rheology for the mantle with a viscosity of $\eta = 1 \cdot 10^{18}$ Pa s and a relaxation coefficient $\alpha = 0.1$. We use the fault models from Decriem et al. (2010) and calculate the corresponding viscoelastic relaxation for both of our GPS datasets (Figure 2). We found a WRSS=150 and WRSS=250 for the May-August 2008 and the August 2008 - May 2009 datasets, respectively.

3.3 Afterslip

Elastic slip following an earthquake has been identified as a possible postseismic mechanism in many studies (e.g. Heki et al., 1997; Langbein et al., 2006). We estimate afterslip over the Kross and In-

gólfsfjall fault planes, by extending the fault surfaces estimated by Decriem et al. (2010) following
Árnadóttir et al. (2005). We calculate the distribution of afterslip for the two time spans of our GPS
datasets. We also calculate the afterslip after correcting the GPS displacements for the viscoelastic
relaxation using the model from section 3.2. The model results are shown in Figure 5.

For the May - August 2008 dataset the best fit model has a maximum slip of 0.07 m on the In-
gólfsfjall fault and 0.1 m on the Kross fault (WRSS=118). When we correct the data for viscoelastic
relaxation, we find that the slip is concentrated above 2 km, with the same maximum slip as before.
This model has a slightly better fit (WRSS=110). For the second time interval, August 2008 - May
2009, the afterslip is much smaller, with up to 0.02 m and 0.01 m on the Ingólfsfjall and Kross faults,
respectively (WRSS=220). Correcting for the viscoelastic signal again removes the slip on the deeper
parts of the faults, and the best fit model has a WRSS=180. The models where we include both vis-
coelastic relaxation and afterslip do not indicate significant deep afterslip. These models also provide
the best fit to our data and are therefore our preferred models. Figure 3 shows the timeseries for
selected continuous and semi-continuous GPS stations in the epicentral area and the displacements
predicted by the composite model with both viscoelastic relaxation and afterslip.

3.4   Pore Pressure model

Here we investigate whether the ENE-trending phase jump observed with InSAR could be caused by
brittle faulting. A forward calculation using the fault models for the May 2008 main shocks (Decriem
et al., 2010). indicates that the predicted coseismic deformation in the area is smooth and no such
sharp deformation is expected (Figure 7). We also test dislocation models, both assuming left lateral
strike slip and normal faulting (Figure 7). To reproduce the InSAR signal the fault models have to
extend from the surface to a maximum depth of 500 m. This is very shallow considering that most
of the aftershocks are located below 6 km (Brandsdóttir et al., 2011). Furthermore, The dislocation
models that may explain the InSAR signal do not fit the GPS station displacement. For example we do
not observe large eastward displacement at HLID as suggested by the left-lateral model or northward
displacement suggested by the normal fault model (Figure 3). We therefore conclude that faulting is
not a likely mechanism to explain the observed deformation in this area.

We then explore whether the InSAR discontinuity could be related to a pore-pressure difference
between the northern and southern part of the epicentral area. We calculate the pore pressure relaxation
according to Darcy's law. Darcy's law states that the flow discharge velocity is proportional to the
gradient of the fluid pressure : $v = -\frac{K}{\mu}(\Delta p)$ with K the permeability, μ the viscosity of the fluid and
p the pore pressure ($p = -B\sigma_{kk}/3$ with B the Skempton coefficient).

We use an implicit finite difference solver to calculate the pore-pressure change with time. Implicit

schemes (solving $U_{n+1}/dt = U_n$) are numerically more stable than explicit integration schemes ($U_n *$ $dt = U_{n+1}$) in our case the system of equations to solve is (Biot, 1941; Gaspar et al., 2007):

$$\begin{bmatrix} AK^{-1} & G \\ G^{-1} & -\tau L \end{bmatrix} \begin{bmatrix} v \\ p \end{bmatrix} = \begin{bmatrix} 0 \\ f \end{bmatrix} \tag{1}$$

with A the connectivity matrix (linking the neighboring elements to each others), K the permeabilities, G the Gradient operator, τ the time step, L the Laplacian operator, v the Darcy velocity, p the fluid pressure and f the injection of fluid within the system (here f=0). We test two cases with initial pore pressure calculated from the coseismic model of Decriem et al. (2010). We estimate changes with time for v and p, first using a homogeneous halfspace, and second with an additional impermeable structure ($K << \epsilon$) at the location of the InSAR phase discontinuity. Resulting pore pressure calculations are shown in Figure 6.

4 DISCUSSION

Our viscoelastic model shows good agreement to the east with the far-field GPS stations (BRJA, KIDJ, 265S) for the May - August 2008 time period. However the predicted displacements are much smaller than observed at the near field stations (HVER, SELF). Our afterslip model shows a large patch of slip at depth. This particular patch of afterslip is located below 15 km depth where we expect viscoelastic relaxation may occur. The deep afterslip may reflect deformation observed at the far-field stations due to viscoelastic relaxation, rather than deep afterslip. After we correct the dataset for viscoelastic relaxation, no deep patch of slip is required and the models only suggest shallow afterslip (Figure 5). We then select the composite model as our preferred, with both viscoelastic relaxation (explaining the far-field motion) and shallow afterslip (up to 10 cm of slip) to reproduce the near field station displacements. Our afterslip models show a small amount of slip, located on the planes that ruptured during the coseismic phase. After the June 2000 events, afterslip during the first months could not be ruled out by Jónsson et al. (2003) from InSAR data. The GPS measurements following the June 2000 main shocks span over a year, and lack the temporal resolution of the May 2008 data (Árnadóttir et al., 2005). The station displacements during 2000 - 2001 are also affected by a strong poroelastic signal observed by InSAR. Thus, deformation caused by shallow afterslip after the June 2000 events may be difficult to identify, as apparent in the afterslip models derived by Árnadóttir et al. (2005). Subsequent studies suggest that viscoelastic rebound was the prominent mechanism (Jónsson, 2008; Decriem & Árnadóttir, 2011), although afterslip at shallow depth can not be ruled out.

For the May - August 2008 time period the poroelastic model results in smaller than measured GPS displacements. We can not rule out that poroelastic relaxation occurred during the first months (May

174 - August 2008), at the same time as the dominant mechanisms we have identified (afterslip and vis-
175 coelstic relaxation). However, the sharp linear feature in InSAR could be attributed to elevated/lower
176 ground-water level along an impermeable barrier (Bawden et al., 2001). If a vertical impermeable
177 structure extended through the crust as shown in Figure 6 then high pressure may build up north of
178 the structure and low pressure to the south, after the May mainshocks. The shear strength of the mate-
179 rial along the impermeable boundary could decrease due to higher pore pressure on the northern side,
180 promoting aftershocks in this particular area. The ENE-trending lineament is located at the western
181 end of the SISZ, where the tectonic regime changes from a transform zone (NS rupturing faults SISZ)
182 to oblique spreading in the Reykjanes Peninsula (Keiding et al., 2008), this lineament has been a lo-
183 cus for earthquake activity throughout the years with a small seismic episode in 1998 . More advanced
184 modelling is, however, required to account for the fully coupled solution relating fluid flow and elastic
185 deformation, and a detailed comparison of the Coulomb stress change with aftershock rate (Lindman,
186 2009; Lindman et al., 2010) to test the validity of this hypothetical impermeable structure. We there-
187 fore propose this pore-pressure model as an alternative mechanism to faulting that may explain both
188 the InSAR observations and the numerous aftershocks recorded in the area.

189   In order to extract the postseismic signal during August 2008 to May 2009, the GPS station dis-
190 placements need to be corrected for plate spreading and deformation due to geothermal exploration in
191 the Hengill area. The plate bounary is, however, complex in the epicentral area of the May 2008 earth-
192 quakes, and our models are rather simple. As a result, our estimates of the postseismic deformation
193 may be biased, and the apparent discrepancy between the preferred model (viscoelastic relaxation and
194 afterslip) may in fact be partly due to inadequacies in the models we use to correct for background
195 signals.

5   CONCLUSION

197 We present here a study of the postseismic deformation transient observed by GPS, following the May
198 2008 mainshocks. We find rapid station displacements during the first two months (June-August) and
199 a smaller signal during the following months (August 2008-May 2009). Our optimal model includes
200 both viscoelastic relaxation to reproduce the far-field deformation and shallow afterslip (up to 10 cm
201 slip in the top 2 km) to reproduce the large transient we observe at stations close to the faults.

202   The models we tested do not support a significant deformation signal due to poroelastic relaxation
203 in the weeks following the mainshocks. This difference in the transient between the June 2000 and
204 May 2008 events can be due to the smaller magnitude of the May 2008 mainshocks or the poroelastic
205 rebound may occur within hours and can not be distinguish from the coseismic offsets. However, we
206 identify an ENE-trending lineament with large number of aftershocks correlating with a very sharp

phase discontinuity in the InSAR data during the first days following the events. This feature can not be explained by our composite model or any type of faulting. We propose a pore pressure model including an E-W impermeable structure to explain the signal and seismicity in this area.

6   ACKNOWLEDGMENTS

References

Altamimi, Z., Collilieux, X., Legrand, J., Garayt, B., & Boucher, C., 2007. ITRF2005: A new release of the International Terrestrial Reference Frame based on time series of station positions and Earth Orientation Parameters, *J. Geophys. Res.*, **112**, B09401, doi:10.1029/2007JB004949.

Árnadóttir, T., Hreinsdóttir, S., Gudmundsson, G., Einarsson, P., Heinert, M., & Völksen, C., 2001. Crustal deformation measured by GPS in the South Iceland Seismic Zone due to two large earth-quakes in June 2000, *Geophys. Res. Lett.*, **28**, 4031–4033.

Árnadóttir, T., Jónsson, S., Pollitz, F. F., Jiang, W., & Feigl, K. L., 2005. Postseismic deformation following the June 2000 earthquake sequence in the south Iceland seismic zone, *J. Geophys. Res.*, **110**, B12308, doi: 10.1029/2005JB003701.

Árnadóttir, T., Jiang, W., Feigl, K. L., Geirsson, H., & Sturkell, E., 2006. Kinematic models of plate boundary deformation in southwest Iceland derived from GPS observations, *J. Geophys. Res.*, **111**, B07402, doi: 10.1029/2005JB003907.

Bawden, G. W., Thatcher, W., Stein, R. S., Hudnut, K. W., & Peltzer, G., 2001. Tectonic contraction across Los Angeles after removal of groundwater pumping effects, *Nature*, **412**, 812–815.

Biot, M., 1941. General theory of three dimensional consolidation, *J. Appl. Phys.*, **12**, 155–169.

Brandsdóttir, B., Parsons, M., White, R. S., Gudmundsson, O., Drew, J., & Thorbjarnadóttir, B., 2011. The may 29 2008 earthquake aftershock sequence within the South Iceland Seismic Zone: Fault locations and source parameters of aftershocks, *Jokull: journal of the glaciological and geological societies of Iceland*, p. In Press.

238 Clifton, A. E. & Einarsson, P., 2005. Styles of surface rupture analysis accompanying the June 17
239   and 21, 2000 earthquakes in the South Iceland Seismic Zone, *Tectonophysics*, **396**, 141–159.

240 Dach, R., Hugentobler, U., Fridez, P., & Meindl, M., 2007. Bernese GPS software version 5.0, Tech.
241   rep., Astronomical Institure, University of Bern, Bern, Switzerland.

242 Decriem, J. & Árnadóttir, T., 2011. Transient crustal deformation in the South Iceland Seismic Zone
243   observed by GPS and InSAR during 2000-2008, *Tectonophysics*, p. submitted.

244 Decriem, J., Árnadóttir, T., Hooper, A., Geirsson, H., Sigmundsson, F., Keiding, M., Ófeigsson, B. G.,
245   Hreinsdóttir, S., Einarsson, P., LaFemina, P. C., & Bennett, R., 2010. The 2008 May 29 earthquake
246   doublet in SW Iceland, *Geophys. J. Int.*, **181**, 1128–1146.

247 DeMets, C. G., Gordon, R., Argus, D. F., & Stein, S., 1994. Effect of recent revisions to the geomag-
248   netic reversal time scale on estimates of current plate motions, *Geophys. Res. Lett.*, **21**, 2191–2194.

249 Einarsson, P., 2008. Plate boundaries, rifts and transforms in Iceland, *Jökull*, **58**, 35–38.

250 Freed, A., Bürgman, R., Calais, E., Freymueller, J., & Hreinsdottir, S., 2006. Implications of de-
251   formation following the 2002 Denali, Alaska, earthquake for postseismic relaxation processes and
252   lithospheric rheology., *J. Geophys. Res.*, **111**, doi:10.1029/2005JB003894.

253 Gaspar, F., Lisbona, F., Oosterlee, C., & Vabishchevich, P., 2007. An efficient multigrid solver for a
254   reformulated version of the poroelasticity system, *Computer Methods in Applied Mechanics and*
255   *Engineering*, **196**(8), 1447 – 1457, Domain Decomposition Methods: recent advances and new
256   challenges in engineering.

257 Heki, K., Miyazaki, S., & Tsuji, H., 1997. Silent fault slip following an interplate thrust earthquake
258   at the Japan trench, *Nature*, **386**, 595–598.

259 Herring, T. A., King, R. W., & McClusky, S. C., 2006. GLOBK reference manual, Global Kalman
260   filter VLBI and GPS analysis program, release 10.3, Tech. rep., Mass. Inst. Technol., Cambridge,
261   MA, USA.

262 Hreinsdóttir, S., Árnadóttir, T., Decriem, J., Geirsson, H., Tryggvason, A., Bennett, R. A., & LaFem-
263   ina, P., 2009. A complex earthquake sequence captured by the continuous GPS network in SW
264   Iceland, *Geophys. Res. Lett.*, **36**, L12309.

265 Jakobsdóttir, S. S., Gudmundsson, G. B., Hjaltadóttir, S., Kjartansson, E., Roberts, M. J., Vogfjörd,
266   K. S., & Stefansson, R., 2008. Magnitude 6.3 earthquake in SW-Iceland., *31st ESC General As-*
267   *sembly, Hersonissos, 7.-12. september.*.

268 Jónsson, S., 2008. Importance of post-seismic viscous relaxation in southern Iceland, *Nature Geo-*
269   *science*, **1**, 136–139.

270 Jónsson, S., Segall, P., Pedersen, R., & Björnsson, G., 2003. Post-earthquake ground movements
271   correlated to pore-pressure transients, *Nature*, **424**, 179–183.

272 Kampes, B. & Usai, S., 1999. Doris: The delft object-oriented radar interferometric software., in in
273 Proc. 2nd Int. Symp. Operationalization of Remote Sensing.

274 Keiding, M., Árnadóttir, T., Sturkell, E., Geirsson, H., & Lund, B., 2008. Strain accumulation along
275 an oblique plate boundary: The Reykjanes Peninsula, southwest Iceland, *Geophys. J. Int.*, **172(1)**,
276 861–872, doi:10.1111/j.1365–246X.2007.03655.x.

277 Keiding, M., Árnadóttir, T., Jónsson, S., Decriem, J., & Hooper, A., 2010. Plate boundary defor-
278 mation and man-made subsidence around geothermal fields on the Reykjanes Peninsula, Iceland,
279 *Journal of Volcanology and Geothermal Research*, **194**, 139–149.

280 Langbein, J., Murray, J., & Snyder, H., 2006. Coseismic and initial postseismic deformation from the
281 2004 Parkfield, California, earthquake, observed by Global Positioning System, electronic distance
282 meter, creepmeters, and borehole strainmeters, *Bull. Seismol. Soc. Am.*, **96**, 304–320.

283 Lindman, M., 2009. *Physics of aftershocks in the South Iceland Seismic Zone*, Ph.D. thesis, Faculty
284 of Science and Technology, Uppsala University, Uppsala, Sweden.

285 Lindman, M., Lund, B., & Roberts, R., 2010. Spatiotemporal characteristics of aftershock sequences
286 in the South Iceland Seismic Zone: interpretation in terms of pore pressure diffusion and poroelas-
287 ticity, *Geophys. J. Int.*, **183**, 1104–1118.

288 Masterlark, T. & Hughes, K., 2008. The next generation of deformation models for the 2004 M9
289 Sumatra-Andaman Earthquake, *Geophys. Res. Lett.*, **35**.

290 McClusky, S. et al., 2000. Global Positioning System constraints on plate kinematics and dynamics
291 in the eastern Mediterranean and Caucasus, *J. Geophys. Res.*, **105(B3)**, 5695–5720.

292 Pedersen, R., Sigmundsson, F., Feigl, K. L., & Árnadóttir, T., 2001. Coseismic interferograms of
293 two M_s=6.6 earthquakes in the South Iceland Seismic Zone, June 2000, *Geophys. Res. Lett.*, **28**,
294 3341–3344.

295 Pedersen, R., Jónsson, S., Árnadóttir, T., Sigmundsson, F., & Feigl, K. L., 2003. Fault slip distribution
296 of two M_w=6.5 earthquakes in South Iceland estimated from joint inversion of InSAR and GPS
297 measurements, *Earth Planet. Sci. Lett.*, **213**, 487–502.

298 Stefánsson, R., Bödvarsson, R., Slunga, R., Einarsson, P., Jakobsdóttir, S., Bungum, H., Gregersen,
299 S., Havskov, J., Hjelme, J., & Korhonen, H., 1993. Earthquake Prediction Research in the South
300 Iceland Seismic Zone and the SIL Project, *Bull. Seismol. Soc. Am.*, **83**(3), 696–716.

301 Wang, L., Wang, R., Roth, F., Enescu, B., Hainzl, S., & Ergintav, S., 2009. Afterslip and viscoelastic
302 relaxation following the 1999 M7.4 İzmit earthquake from GPS measurements, *Geophys. J. Int.*,
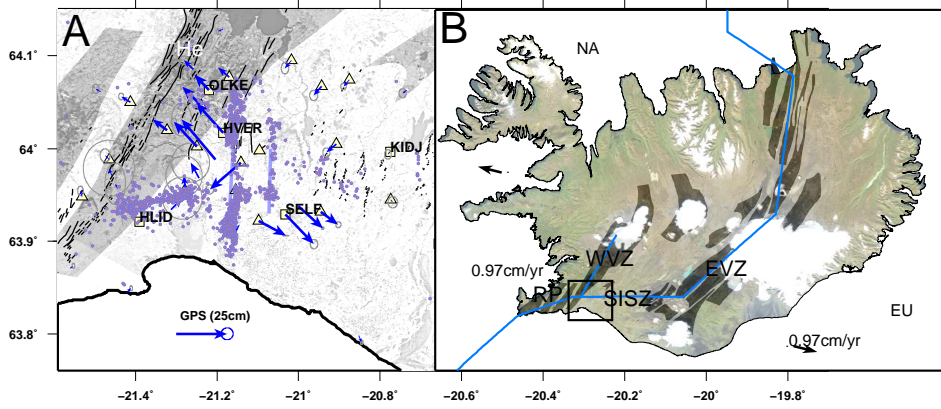303 **178**, 1220–1237.

Figure 1. The tectonic setting of the South Iceland Seismic Zone (SISZ). (A) Coseismic offsets (blue arrows) estimated from GPS measurements due to the May 2008 earthquakes. The two thick vertical lines show the locations of the fault planes estimated for the May 2008 events. Yellow squares indicate the locations of the CGPS stations and triangles the location of semi-continuous GPS stations maintained after the mainshocks. The Hengill volcanic system is indicated with "He". (B) The plate boundary across Iceland, and the location of the study area with a rectangle. The main tectonic features are the Reykjanes Peninsula (RP), the Western Volcanic Zone (WVZ), The South Iceland Seismic Zone (SISZ), and the Eastern Volcanic Zone (EVZ). The black arrows show the plate spreading according to the NUVEL-1A plate motion model (DeMets et al., 1994).
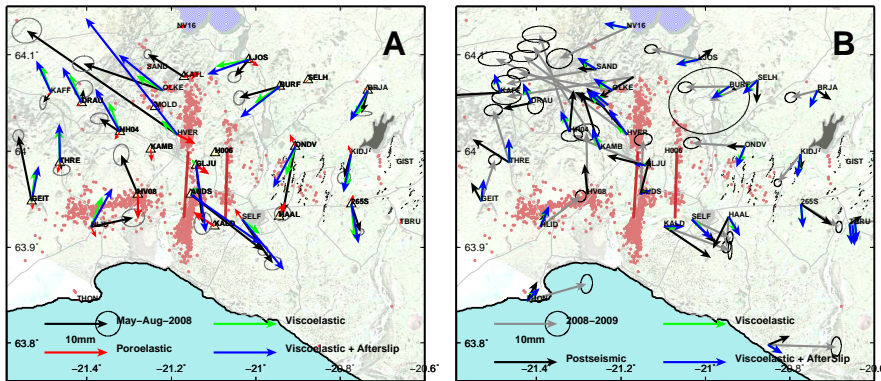

Figure 2. Postseismic GPS displacements and model predictions : (A) May - August 2008 period and (B) August 2008 - May 2009 time period. The black arrows show the postseismic signal i.e., the data (gray arrows) corrected from background signal. The error ellipses denote 95% uncertainties. The red lines show the locations of the fault ruptures estimated for the May 2008 events (Decriem et al., 2010).
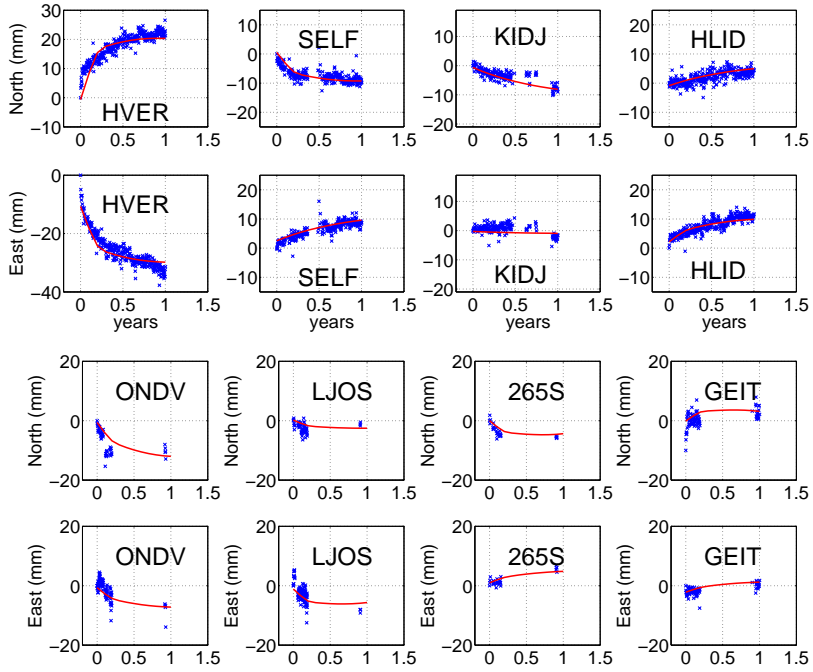
Figure 3. GPS timeseries corrected for background motion (blue crosses) and composite viscoelastic+afterslip postseismic model (red lines) for continuous GPS stations (top row) and semi-continuous stations (bottom row) in the study area.
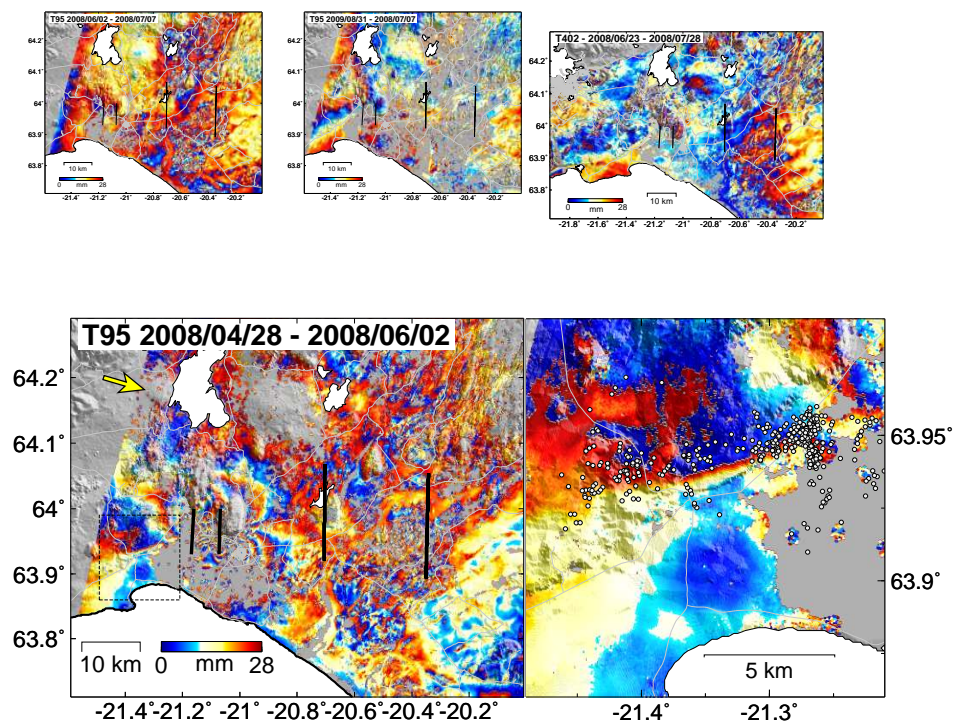
Figure 4. InSAR data from Envisat T95 (top left, middle and bottom) and T402 (top right) the colorscale shows the wrapped displacement in the line of sight direction. The black thick lines show the locations of the fault that ruptured in the June 2000 earthquakes (two eastern fault) and the May 2008 (two western faults). Bottom left: The black square shows the location of the right inset, the yellow arrow the direction of the line of sight of the satellite. Bottom right : The dots show afterhocks recorded by the SIL network for 2008/04/29 - 2008/06/02.
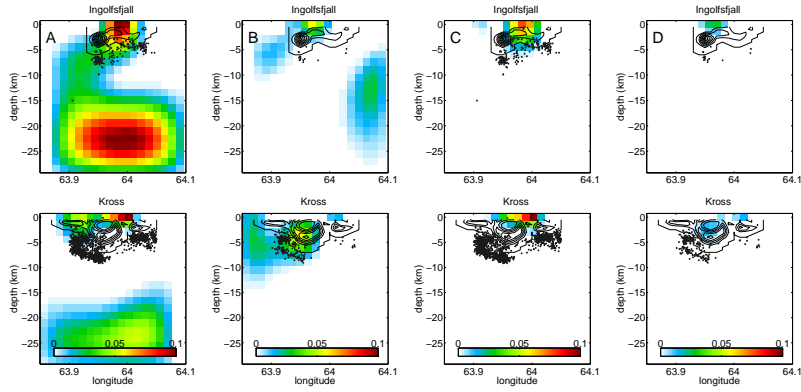
Figure 5. Afterslip distribution (A,C) May - August 2008 and (B,D) 2008 to 2009 . The two plots on the left (A,B) show the slip we estimate from GPS data and the plots on the right (C,D) inversion from GPS data corrected for viscoelastic relaxation. The black dots show the locations of aftershock recorded by the SIL network during the respective time periods. The colorscale shows the amount of right lateral slip in m.
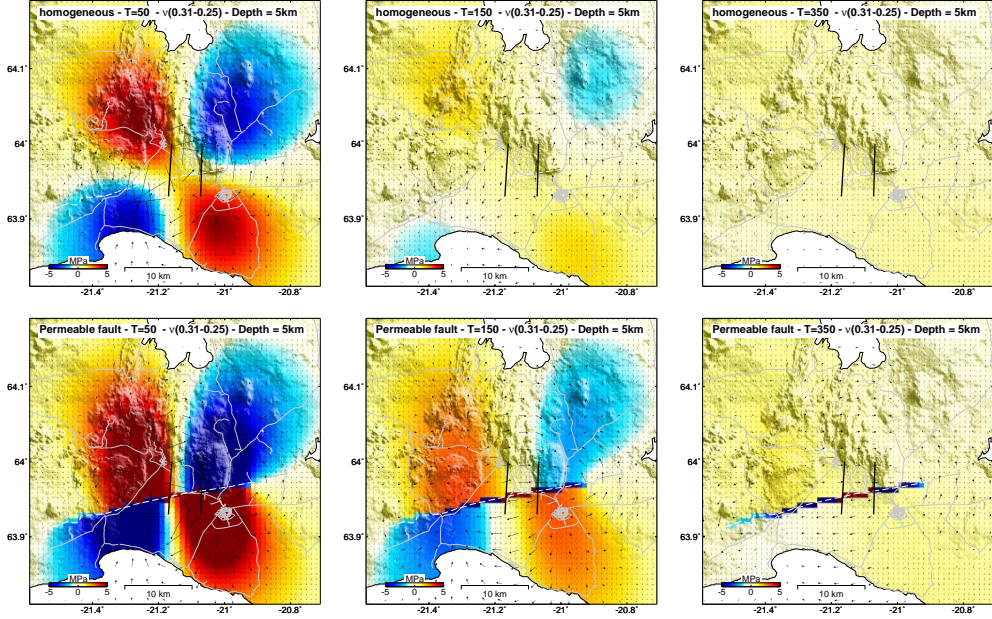
Figure 6. Comparison of pore pressure relaxation after the May 2008 earthquakes in case of homogeneous crust (top row) and in case of a ENE impermeable structure (bottom row) at integration steps =50,100,150. Our numerical solver is non-dimensional so the corresponding time steps scale with the viscosity and permeability in the model. The colorscale shows the pore pressure and the black vectors the fluid velocity field. The dashed white line shows the location of the hypothetic impermeable structure coinciding with the E-W fringe observed by InSAR, the apparent steps in the lineament comes from the aliasing of the line on the solver grid.
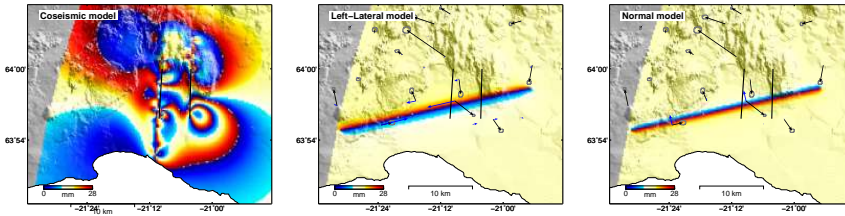

Figure 7. Dislocation models we tested to reproduce the InSAR discontinuity 4(a) May 2008 coseismic displacements, (b) left-lateral strike slip (c) normal fault. The black arrows show the May-August 2008 GPS displacements and blue arrows the predicted displacements for the dislocation models.